Präzisionsmessungen der spinabhängigen Strukturfunktionen g_1^p und g_1^d des Protons und des Deuterons sowie Extraktion der spinabhängigen Strukturfunktion g_1^n des Neutrons mit dem HERMES-Experiment

Precision Measurements of the spin-dependent structure functions g_1^p and g_1^d of the proton and the deuteron and extraction of the neutron spin structure function g_1^n at HERMES

Den Naturwissenschaftlichen Fakultäten
der Friedrich-Alexander-Universität Erlangen-Nürnberg
zur
Erlangung des Doktorgrades

vorgelegt von
Markus Ehrenfried

aus Rheinfelden

Als Dissertation genehmigt von den
Naturwissenschaftlichen Fakultäten
der Universität Erlangen-Nürnberg

Tag der mündlichen Prüfung:	21. Juli 2005
Vorsitzender der Promotionskommission:	Prof. Dr. D.-P. Häder
Erstberichterstatter:	Prof. Dr. K. Rith
Zweitberichterstatter:	Prof. Dr. M. Düren

Contents

Chapter 1

Introduction

Spin is one of the most fundamental properties of a particle. It determines how particles in an ensemble are allowed to behave, whether they are allowed to settle all in the same quantum state like particles with integral spin[1] (0, 1, 2, ...) obeying BOSE-EINSTEIN statistics or whether they are pressed to build up higher and higher structures as the PAULI principle forces them to follow FERMI-DIRAC statistics because they have half-integral spin (1/2, 3/2, 5/2, ...).

Spin is also what differs matter particles from particles which mediate forces: all matter in the universe is built from a small number of fundamental spin 1/2 particles (quarks and leptons) while all forces are mediated by particles which have integral spin.

The spin-1/2 nature of the building blocks of the atom – protons and neutrons in the nucleus (therefore called *nucleons*) and electrons in the atom's shell – is the very reason why matter arranges into complex structures instead of condensating into something which would be so extremely boring that nobody would ever be around to wonder *how* boring it actually is.

While the electron is an elementary particle which just has an intrinsic spin of 1/2, the nucleon is a complicated object composed of quarks which are glued together by the strong interaction, mediated by gluons. Quarks, being matter particles, have also an intrinsic spin of 1/2 while gluons as force carrying particles have an integral spin of 1. Besides their intrinsic spin the quarks and gluons can in addition also carry an orbital angular momentum (very much like the electrons in the atom's shell). All these contributions add up to the resulting nucleon spin of *precisely* 1/2:

$$\frac{1}{2} = \frac{1}{2}\Delta\Sigma + L_z^q + \Delta G + L_z^G \tag{1.1}$$

where $\Delta\Sigma$ is the net quark helicity, ΔG is the net gluon helicity and L_z^q and L_z^G are the contributions of the orbital angular momenta of quarks and gluons.

[1]The usual convention $\hbar = c = 1$ is used.

In contradiction to early calculations based on relativistic quark models [JM90] [SW98] the European Muon Collaboration (EMC) at CERN discovered in 1987 that only a surprisingly small fraction ($\Delta\Sigma \approx 0.1 - 0.2$) of the nucleon's spin could be attributed to the spins of the quarks [Muon88] [Muon89]. This became known as the 'spin crisis'.

The HERMES experiment at DESY is one of several experiments which were designed to disentangle the individual contributions adding up to the nucleon's resulting spin. The spin structure can be parametrized by phenomenological structure functions of which one – the spin-dependent structure function g_1 – is the focus of this thesis. The contribution of the quark spins $\Delta\Sigma$ is related to the first moment of this structure function, $\int_0^1 g_1(x)\mathrm{d}x$, which is of particular interest as it allows a precise test of Quantum Chromodynamics (QCD) via the fundamental Bjorken sum rule.

HERMES has measured the spin-dependent structure function g_1 of the proton and the deuteron with high precision in the kinematic range $0.0021 < x < 0.9$ and $0.1\,\mathrm{GeV}^2 < Q^2 < 20\,\mathrm{GeV}^2$. Based on these measurements the structure function g_1 of the neutron was extracted. The measured spin asymmetries were corrected for QED radiative effects and detector smearing using a Monte Carlo based unfolding method. The first moments for proton and deuteron were calculated within the measured x range.

Chapter 2

Spin-dependent structure functions

Deep inelastic scattering (DIS) experiments, where the nucleon is probed with leptons, have been used successfully for more than four decades to gain knowledge about the nucleon's internal structure. In DIS the four-momentum transfer q^2 determines the resolution at which the nucleon is observed[1]. If both the leptonic probe and the nucleon are polarized, the spin structure of the nucleon is accessible as the lepton – due to conservation of angular momentum – can only interact with those quarks inside the nucleon which have opposite spin orientation with respect to the incoming lepton's spin. Therefore the spin structure of the nucleon can be related to cross section asymmetries which can be parametrized by structure functions. The spin-dependent structure functions can be expressed in terms of quark helicity distributions.

In this chapter the kinematics of the DIS process is briefly introduced and cross-section asymmetries, structure functions and their interpretation in the Quark Parton Model and in Quantum Chromo Dynamics (QCD) are discussed.

2.1 Kinematics of deep inelastic scattering

In the process of deep inelastic lepton-nucleon scattering (see Fig. 2.1 and Table 2.1) a lepton e is scattered off a nucleon N (proton or neutron), $e + N \longrightarrow e' + X$, exciting it to a hadronic final state X with an invariant mass W substantially larger than the nucleon mass M. At HERMES the leptons are electrons or positrons with an energy of $E = 27.6$ GeV (which might vary marginally depending on the tune of the HERA electron ring). As HERMES is a fixed target experiment, the target nucleon is at rest in the

[1] A virtual photon of four-momentum $\mathbf{q}$ is able to resolve structures of the order $\hbar/\sqrt{q^2}$.

lab frame. In an inclusive measurement like the one described in this thesis only the scattered lepton e' is detected but no knowledge about the hadronic final state (excited nucleon and products of the fragmentation process) is taken into account.

The cross-sections for deep inelastic scattering are — contrary to the elastic cross-sections — large and depend only weakly on the squared four-momentum transfer q^2. This indicates that the electromagnetic probe is scattering off *pointlike* constituents inside the nucleon. These so-called *partons* were identified with quarks by FEYNMAN [Fey72] in 1969.

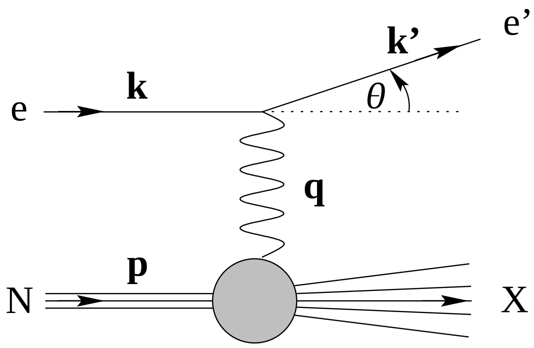

Figure 2.1: Deep inelastic scattering in the approximation of one-photon exchange. See Table 2.1 for the definition of kinematic quantities.

The interaction is mediated by the exchange of a neutral virtual boson (γ or Z^0). At center-of-mass energies considerably smaller than the Z^0 mass, weak interactions can safely be neglected ($m_{Z^0} \approx 91.2$ GeV/c^2, $\sqrt{s}$ at HERMES ≈ 7.3 GeV). In the HERMES energy regime only electromagnetic interactions are relevant and the BORN approximation of one-photon exchange is used. This process is depicted in Fig. 2.1, the kinematic variables used to describe it are defined in Table 2.1.

The kinematics of a scattering event can be described in terms of the negative squared four-momentum transfer Q^2 and the two dimensionless scaling variables x and y which are defined as

$$Q^2 \equiv -q^2 = -(\mathbf{q}\cdot\mathbf{q}) = -(\mathbf{k}-\mathbf{k}')^2, \tag{2.1}$$

$$x \equiv \frac{Q^2}{2\,\mathbf{p}\cdot\mathbf{q}} = \frac{Q^2}{2\,M\nu}, \tag{2.2}$$

$$y \equiv \frac{\mathbf{p}\cdot\mathbf{q}}{\mathbf{p}\cdot\mathbf{k}} = \frac{\nu}{E}. \tag{2.3}$$

Here $\mathbf{k}$, $\mathbf{k}'$, $\mathbf{p}$ and $\mathbf{q}$ are the four-momenta of the incident electron, the scattered electron, the target nucleon of mass M and the exchanged virtual photon respectively. E is the the energy of the incident electron (equal to

$\mathbf{k} = (E, \vec{k}),\ \mathbf{k'} = (E', \vec{k'})$	four-momenta of incident and scattered electron
$\mathbf{p} = (E_p, \vec{p}) \stackrel{lab}{=} (M, 0)$	four momentum of initial target nucleon of mass M
$\mathbf{q} = (\nu, \vec{q}) = \mathbf{k} - \mathbf{k'}$	four-momentum of the exchanged virtual photon
$\mathbf{S} = S^\mu \stackrel{lab}{=} (0, \vec{P^T})$	spin four-vector of the target nucleon
$\nu = \frac{\mathbf{p}\cdot\mathbf{q}}{M} \stackrel{lab}{=} E - E'$	energy of the exchanged virtual photon
$\theta,\ \phi$	polar and azimuthal scattering angle of the electron
$Q^2 = -q^2 \stackrel{lab}{\cong} 4EE' \sin^2 \frac{\theta}{2}$	negative squared four-momentum transfer
$s = (\mathbf{p} + \mathbf{k})^2 \stackrel{lab}{\cong} M^2 + 2ME$	squared center-of-mass energy (HERMES: $\sqrt{s} \approx 7.3$ GeV)
$W^2 = (\mathbf{p} + \mathbf{q})^2 \stackrel{lab}{=} M^2 + 2M\nu - Q^2$	squared invariant mass of photon-nucleon system
$x = \frac{Q^2}{2\mathbf{p}\cdot\mathbf{q}} = \frac{Q^2}{2M\nu} \quad (0 \leq x \leq 1)$	BJORKEN scaling variable
$y = \frac{\mathbf{p}\cdot\mathbf{q}}{\mathbf{p}\cdot\mathbf{k}} = \frac{\nu}{E} \quad (0 \leq y \leq 1)$	fractional energy transfer from electron to nucleon

Table 2.1: Kinematic quantities used to describe the DIS process. The nucleon is at rest in the lab frame. As the energies E, E' are much larger than the electron mass m_e it is a valid approximation to neglect m_e.

the HERA electron beam energy of 27.6 GeV) and $\nu \stackrel{lab}{=} E - E'$ is the virtual photon's energy.

The BJORKEN scaling variable x $(0 \leq x \leq 1)$ can be interpreted as a measure for the inelasticity of the scattering process. In case of elastic scattering the hadronic final state equals just the nucleon's mass in the initial state ($W^2 = M^2$) and therefore $x = 1$. For inelastic scattering ($W^2 > M^2$) x has values < 1. Within the Quark Parton Model which will be discussed below x can also be interpreted as the fraction of the nucleon's momentum which is carried by the struck quark. The variable y is the fractional energy transfer from the incident electron to the nucleon $(0 \leq y \leq 1)$.

The kinematics of an inelastic event can be completely described by any combination of two out of the three variables x, y and Q^2. Obviously there is no clear border where inelastic scattering becomes *deep* inelastic. Traditionally, the DIS regime is characterized by $W^2 \gg M^2$ and $Q^2 \gg$

$M^2 \approx 1$ GeV^2. For $Q^2 \to 0$, where the transition from lepto-production to photo-production occurs, the application of perturbative QCD (pQCD) becomes questionable.

2.2 Cross section asymmetries in spin-dependent DIS

The cross section for deep inelastic scattering can be expressed in terms of the leptonic tensor $L_{\mu\nu}$, describing the emission of a virtual photon at the lepton vertex, and the hadronic tensor $W^{\mu\nu}$, describing the absorption of the virtual photon by the target. The differential cross section for detecting a scattered lepton in the final state under a solid angle $\mathrm{d}\Omega$ and in the final energy range $[E', E' + \mathrm{d}E']$ may be written as [AEL95]

$$\frac{\mathrm{d}^2\sigma}{\mathrm{d}\Omega\,\mathrm{d}E'} = \frac{\alpha^2}{2MQ^4}\,\frac{E'}{E}\,L_{\mu\nu}W^{\mu\nu} \tag{2.4}$$

where α denotes the fine structure constant. The leptonic tensor $L_{\mu\nu}$ can be exactly calculated in quantum electrodynamics (QED) whereas the lack of knowledge about the nucleon's internal structure doesn't permit to do the same with $W^{\mu\nu}$ in QCD so far, although the coupling between quarks and gluons is understood.

The hadronic tensor can be split into two parts of which one behaves symmetric (S) under parity transformations and the other one behaves antisymmetric (A) [AEL95][2]:

$$W_{\mu\nu} = W_{\mu\nu}^{(S)} + iW_{\mu\nu}^{(A)}. \tag{2.5}$$

The symmetric part $W_{\mu\nu}^{(S)}$ is spin-independent and can be parametrized by the two dimensionless scalar structure functions $F_1(x, Q^2)$ and $F_2(x, Q^2)$ which describe the deviation of the DIS cross section from the MOTT cross section[3]. The unpolarized DIS cross section is proportional to $L_{\mu\nu}^{(S)}W^{\mu\nu\,(S)}$ (where $L_{\mu\nu}^{(S)}$ denotes the symmetric part of the leptonic tensor).

The antisymmetric part $W_{\mu\nu}^{(A)}$ of the hadronic tensor describes the spin structure of the nucleon. It can be accessed by means of cross section differences between opposite relative spin orientations in experiments where both the incident leptons and the target nucleons are polarized. $W_{\mu\nu}^{(A)}$ can

[2] The leptonic tensor can be split into symmetric and antisymmetric parts in a similar way [AEL95].

[3] The MOTT cross section describes the scattering of relativistic spin-1/2 particles in a pointlike potential. The structure functions $F_1(x, Q^2)$ and $F_2(x, Q^2)$ parametrize the fact that the nucleon isn't pointlike but has a substructure, representing an electric and magnetic charge distribution.

be expressed in termes of two invariant structure functions [FJ01],

$$W^{\mu\nu\,(A)} = -i\epsilon^{\mu\nu\alpha\beta} q_\alpha \left[G_1(\nu, Q^2) \frac{S_\beta}{M^2} + G_2(\nu, Q^2) \frac{(S_\beta \nu M - p_\beta \, \mathbf{S} \cdot \mathbf{q})}{M^4} \right], \tag{2.6}$$

where $\epsilon^{\mu\nu\alpha\beta}$ is the totally antisymmetric tensor, and $\mathbf{S}$ is the nucleon's spin four-vector. In the DIS regime (Bjorken limit)

$$Q^2 \longrightarrow \infty, \quad \nu \longrightarrow \infty \quad \text{while } x = \frac{Q^2}{2\,\mathbf{p} \cdot \mathbf{q}} = \frac{Q^2}{2M\nu} \text{ is kept fixed} \tag{2.7}$$

the Q^2 dependence of $G_1(\nu, Q^2)$ and $G_2(\nu, Q^2)$ vanishes as the virtual photon is able to resolve the *pointlike* constituents of the nucleon and we obtain the two *scaling* functions $g_1(x)$ and $g_2(x)$:

$$g_1(x, Q^2) = \left(\frac{\nu}{M}\right) G_1(\nu, Q^2) \overset{\nu, Q^2 \to \infty}{\longrightarrow} g_1(x) \tag{2.8}$$

$$g_2(x, Q^2) = \left(\frac{\nu}{M}\right) G_2(\nu, Q^2) \overset{\nu, Q^2 \to \infty}{\longrightarrow} g_2(x). \tag{2.9}$$

The Q^2-independence – the so-called *scaling behaviour* – of the structure functions in the DIS regime is an important predicition of the 'naïve' Quark-Parton Model based on the assumption of pointlike constituents within the nucleon. Scaling is experimentally well established but precision measurements show small deviations, the so-called *scaling violations*. This Q^2 dependence of the structure functions is caused by elementary QCD processes like gluon emission and absorption by quarks, production and annihilation of quark-antiquark pairs from gluons, coupling of gluons, etc. [Rit02]. Taking this into account, F_1, F_2, g_1 and g_1 are functions of both x and Q^2.

In a polarized scattering experiment the spin structure function $g_1(x, Q^2)$ can be measured via the DIS cross section difference for two opposite orientations of the target spin, given by [Jaf90] [Rit02]:

$$\begin{aligned} \frac{\mathrm{d}^3(\sigma(\alpha) - \sigma(\pi + \alpha))}{\mathrm{d}x\,\mathrm{d}y\,\mathrm{d}\phi_s} = \frac{e^4}{2\pi^2 Q^2} \Bigg(& \cos\alpha \Big[(1 - \frac{y}{2} - \frac{y^2\gamma^2}{4})\, g_1(x, Q^2) - \\ & - \frac{y\gamma^2}{2}\, g_2(x, Q^2) \Big] - \sin\alpha \cos\phi_s\, \gamma \times \\ & \times \sqrt{1 - y - \frac{y^2\gamma^2}{4}} \Big[\frac{y}{2}\, g_1(x, Q^2) + g_2(x, Q^2) \Big] \Bigg). \end{aligned} \tag{2.10}$$

The angles α and ϕ_s are defined as depicted in Fig. 2.2 and the kinematical factor γ is defined as $\gamma \equiv \sqrt{Q^2}/\nu = 2Mx/\sqrt{Q^2}$.

The spin structure functions $g_1(x, Q^2)$ and $g_2(x, Q^2)$ can be determined experimentally from cross section asymmetries obtained with longitudinally

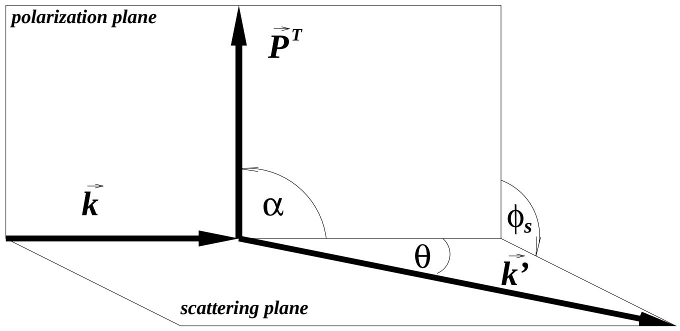

Figure 2.2: Definition of angles: α is the angle between the incident electron's momentum $\vec{k}$ and the polarization vector $\vec{P^T}$ of the target nucleon. The angle between the scattering plane (defined by the momenta of the incident and scattered electron, $\vec{k}$ and $\vec{k'}$) and the polarization plane (formed by $\vec{k}$ and $\vec{P^T}$) is denoted ϕ_s.

polarized beams[4] and longitudinally ($A_{||}$) and transversely ($A_\perp$) polarized targets,

$$A_{||} = \frac{\sigma^{\uparrow\downarrow} - \sigma^{\uparrow\uparrow}}{\sigma^{\uparrow\downarrow} + \sigma^{\uparrow\uparrow}} \quad \text{and} \tag{2.11}$$

$$A_\perp = \frac{\sigma^{\uparrow\rightarrow} - \sigma^{\uparrow\leftarrow}}{\sigma^{\uparrow\rightarrow} + \sigma^{\uparrow\leftarrow}} \quad , \tag{2.12}$$

where $\sigma^{\uparrow\downarrow}$ ($\sigma^{\uparrow\uparrow}$) is the cross section for longitudinally anti-aligned (aligned) lepton and nucleon spins and $\sigma^{\uparrow\rightarrow}$ and $\sigma^{\uparrow\leftarrow}$ denote the cross sections for longitudinally polarized leptons and transversely polarized nucleons in two opposite spin orientations. These cross sections can be expressed as composed of a spin-independent part σ_U and a spin-dependent part σ_P like

$$\sigma^{\uparrow\uparrow} = \sigma_U + \sigma_P \qquad \text{and} \qquad \sigma^{\uparrow\downarrow} = \sigma_U - \sigma_P \tag{2.13}$$

(and similar for the transverse cross sections $\sigma^{\uparrow\rightarrow}$ and $\sigma^{\uparrow\leftarrow}$).

The measured cross section asymmetries (2.11) and (2.12) are related to the virtual photon asymmetries A_1 and A_2 through

$$A_{||} = D \cdot (A_1 + \eta A_2) \quad \text{and} \tag{2.14}$$

$$A_\perp = d \cdot (A_2 - \zeta A_1). \tag{2.15}$$

D and d are the depolarization factors of the virtual photon, quantifying the fraction of the longitudinal electron beam polarization transfered to

[4]For polarized scattering experiments always *longitudinally* polarized beams are used as for a transversely polarized beam all effects would be suppressed by the inverse LORENTZ factor m_e/E ($\approx 1/54000$ at HERMES energies). The transverse polarization vector is not changed when going from the rest frame to the lab-frame, but the longitudinal is [LR00].

the virtual photon 'beam' when the virtual photon carries a fraction $y = (E - E')/E$ of the electron's initial state energy. The depolarization factors are given by [Muon99] [Muon00]:

$$D = \frac{y[(1+\gamma^2 y/2)(2-y) - 2y^2 m_e^2/Q^2]}{y^2(1-2m_e^2/Q^2)(1+\gamma^2) + 2(1+R)(1-y-\gamma^2 y^2/4)} \tag{2.16}$$

$$d = D \cdot \frac{\sqrt{1-y-\gamma^2 y^2/4}\,(1+\gamma^2 y/2)}{(1-y/2)(1+\gamma^2 y/2) - y^2 m_e^2/Q^2}. \tag{2.17}$$

The kinematical factors η and ζ appearing in (2.14) and (2.15) are defined as [Rit02] [FJ01]

$$\eta = \epsilon\gamma y\,[1-(1-y)\,\epsilon] \quad \text{and} \tag{2.18}$$

$$\zeta = \frac{\eta\,(1+\epsilon)}{2\epsilon}, \tag{2.19}$$

where ϵ is the magnitude of the virtual photon's transverse polarization,

$$\epsilon = \left(1 + \frac{1}{2}\,\frac{y^2 + y^2\gamma^2}{1 - y - \frac{1}{4}y^2\gamma^2}\right)^{-1}. \tag{2.20}$$

R is the ratio of the longitudinal and transverse virtual photon absorption cross section, $R = \sigma_L/\sigma_T$, which can be extracted from the two spin-independent structure functions $F_1(x,Q^2)$ and $F_2(x,Q^2)$ measured in unpolarized DIS [WRB+90]:

$$R(x,Q^2) = \frac{\sigma_L}{\sigma_T} = \frac{F_2(x,Q^2)(1+\gamma^2) - 2xF_1(x,Q^2)}{2xF_1(x,Q^2)}. \tag{2.21}$$

Virtual photon asymmetries A_1 and A_2 which are independent from the lepton kinematics can be defined as helicity decomposition of the scattering cross sections of the virtual photon–nucleon system as

$$A_1 \equiv \frac{\sigma_{\frac{1}{2}} - \sigma_{\frac{3}{2}}}{\sigma_{\frac{1}{2}} + \sigma_{\frac{3}{2}}} \quad \text{and} \tag{2.22}$$

$$A_2 \equiv \frac{2\,\sigma_{LT}}{\sigma_{\frac{1}{2}} + \sigma_{\frac{3}{2}}}, \tag{2.23}$$

where $\sigma_{\frac{1}{2}}$ and $\sigma_{\frac{3}{2}}$ denote the cross sections for the virtual photon–nucleon system with a resulting total angular momentum of 1/2 or 3/2 respectively. σ_{LT} is a term which arises from interference between longitudinal and transverse amplitudes. Positivity limits constrain $|A_1| \leq 1$ and $|A_2| \leq \sqrt{R}$; experimentally A_2 is found to be *significantly smaller* than the positivity limit $\sqrt{R}$ for both proton and deuteron targets [E14398] (see also Fig. 6.1). A_1

and A_2 are related to the spin-dependent structure functions $g_1(x, Q^2)$ and $g_2(x, Q^2)$ via

$$A_1(x, Q^2) = \frac{g_1(x, Q^2) - \gamma^2 g_2(x, Q^2)}{F_1(x, Q^2)} \quad \text{and} \tag{2.24}$$

$$A_2(x, Q^2) = \frac{\gamma\,(g_1(x, Q^2) + g_2(x, Q^2))}{F_1(x, Q^2)}. \tag{2.25}$$

In (2.24) the structure function g_2 is kinematically suppressed by the factor γ^2 and $A_1 \approx g_1/F_1$ is a good approximation. Using the relations (2.24) and (2.25) the spin structure function $g_1(x, Q^2)$ which is the focus of this thesis can be related to an experimentally measured longitudinal lepton asymmetry $A_{||}$ (2.11):

$$g_1(x, Q^2) = \frac{F_1(x, Q^2)}{1+\gamma^2}\left[\frac{A_{||}(x, Q^2)}{D(y)} + (\eta - \zeta)\, A_2(x, Q^2)\right] \tag{2.26}$$

$$\simeq \frac{F_1(x, Q^2)}{1+\gamma^2}\,\frac{A_{||}(x, Q^2)}{D(y)}. \tag{2.27}$$

2.3 Interpretation in the Quark Parton Model

In the "intuitive but powerful[5]" Quark-Parton Model (QPM) [Fey72] [BP69] where the nucleon is envisioned in the infinite-momentum frame of reference as an object built up from non-interacting, nearly massless, collinear and asymptotically free quarks[6], the structure functions can be interpreted in a straightforward probabilistic way: The quarks inside the nucleon have *momentum distributions* $q(x)$ and $\overline{q}(x)$ where $q(x)\mathrm{d}x$ ($\overline{q}(x)\mathrm{d}x$) is the number of quarks (anti-quarks) of flavour $q = u, d, s, ...$ ($\overline{q} = \overline{u}, \overline{d}, \overline{s}, ...$) in the nucleon that carry a fractional momentum in the range $[x,\, x + \mathrm{d}x]$. In DIS a virtual photon with energy ν and four-momentum transfer $Q^2 = -q^2$ strikes one of the quarks with momentum fraction x. From the total cross section of this process the structure function $F_1(x)$ can be related to the quark distributions as follows:

$$F_1(x) = \frac{1}{2}\sum_q e_q^2\, (q(x) + \overline{q}(x))\,. \tag{2.28}$$

The sum in (2.28) runs over the quark flavours ($q = u, d, s, ...$) and e_q is the electric charge of the respective quark flavour in units of the elementary charge $|e|$.

[5] [BP69]

[6] In the naïve QPM the quarks have no orbital angular momentum and there are also no polarized gluons present.

Due to the conservation of angular momentum a quark can only absorb a virtual photon if their spin orientation relatively to each other is anti-parallel. Hence, the *quark spin distributions*

$$\Delta q(x) = q^{+}(x) - q^{-}(x) \tag{2.29}$$

can be probed when both beam and target are polarized. $q^{+(-)}(x)\mathrm{d}x$ is defined as the number of quarks of flavour q in the nucleon within the fractional momentum range $[x,\, x+\mathrm{d}x]$ and parallel (+) (anti-parallel (−)) spin orientation with respect to the nucleon's spin. The spin distributions $\overline{q}^{+(-)}(x)\mathrm{d}x$ for anti-quarks are defined analogously. In the QPM the spin-dependent structure function $g_1(x)$ is related to the quark spin distributions to leading order (LO) in QCD as [FJ01]

$$g_1(x) = \frac{1}{2}\sum_q e_q^2 \left(\Delta q(x) + \Delta\overline{q}(x)\right), \tag{2.30}$$

where again the sum runs over all quark flavours. This relation can be decomposed into a flavour singlet (S) and a non-singlet (NS) contribution:

$$g_1(x) = g_1^{\mathrm{S}}(x) + g_1^{\mathrm{NS}}(x) \tag{2.31}$$

with

$$g_1^{\mathrm{S}}(x) = \frac{1}{2}\left\langle e_q^2\right\rangle \sum_q \left(\Delta q(x) + \Delta\overline{q}(x)\right) \equiv \frac{1}{2}\left\langle e_i^2\right\rangle \Delta\Sigma(x) \tag{2.32}$$

$$g_1^{\mathrm{NS}}(x) = \frac{1}{2}\sum_q e_q^2 \left(\Delta q(x) + \Delta\overline{q}(x) - \frac{1}{N_f}\Delta\Sigma(x)\right) \tag{2.33}$$

where N_f denotes the number of quark flavours taken into account and $\left\langle e_q^2\right\rangle = \frac{1}{N_f}\sum_q e_q^2$ is the average value of the squared quark charges.

The singlet distribution $\Delta\Sigma(x) = \sum_q \left(\Delta q(x) + \Delta\overline{q}(x)\right)$ appearing in Eq. (2.32) is of special importance as its first moment reflects the fraction of the nucleon spin contributed by the spins of the quarks.

2.4 First moment of $g_1(x)$ and sum rules

The first moment of the spin-dependent quark distribution of flavour q is given by

$$\Delta q = \int_0^1 \Delta q(x)\mathrm{d}x \tag{2.34}$$

and can be interpreted as the fraction of the nucleon's spin which can be attributed to the spins of the quarks of flavour q. As the structure function g_1 measured in inclusive DIS is not flavour sensitive, the first moment of g_1

in the leading-order QPM, $\Gamma_1 = \int_0^1 g_1(x)\mathrm{d}x$, represents the charge-square-weighted sum over all spin-dependent quark and anti-quark distributions,

$$\Gamma_1 = \int_0^1 g_1(x)\mathrm{d}x = \frac{1}{2}\sum_q e_q^2 \left(\Delta q + \Delta\overline{q}\right). \tag{2.35}$$

The sum in (2.35) runs over the three active quark flavours u, d, s and the Q^2 dependence is absent in the simple QPM. For the proton and the neutron integrals one obtains

$$\Gamma_1^p = \int_0^1 g_1^p(x)\,\mathrm{d}x = +\frac{3}{36}a_3 + \frac{1}{36}a_8 + \frac{4}{36}a_0 \tag{2.36}$$

$$\Gamma_1^n = \int_0^1 g_1^n(x)\,\mathrm{d}x = -\frac{3}{36}a_3 + \frac{1}{36}a_8 + \frac{4}{36}a_0 \tag{2.37}$$

with the $SU(3)_f$ nucleon axial charges

$$a_0 = (\Delta u + \Delta\overline{u}) + (\Delta d + \Delta\overline{d}) + (\Delta s + \Delta\overline{s}) \tag{2.38}$$

$$a_3 = (\Delta u + \Delta\overline{u}) - (\Delta d + \Delta\overline{d}) \tag{2.39}$$

$$a_8 = (\Delta u + \Delta\overline{u}) + (\Delta d + \Delta\overline{d}) - 2(\Delta s + \Delta\overline{s}). \tag{2.40}$$

The expressions for Γ_1^p and Γ_1^n in (2.36) and (2.37) are simply related by isospin symmetry:

$$\Delta u^p = \Delta d^n \qquad \text{and} \qquad \Delta d^p = \Delta u^n. \tag{2.41}$$

The non-singlet axial charges a_3 and a_8 can be obtained from hyperon beta decays. Under the additional assumption of SU(3) flavour symmetry beta decays of hyperons from the spin-1/2 octet can be parametrized in termes of two decay constants, F and D, which are related to the axial charges a_3 and a_8 like [AEL95] [Rit02]

$$a_3 = F + D = \frac{g_A}{g_V} = 1.2573 \pm 0.0028 \qquad \text{and} \tag{2.42}$$

$$a_8 = 3F - D = 0.579 \pm 0.025. \tag{2.43}$$

g_A/g_V is the ratio of axial-vector and vector coupling measured in the Gamov-Teller neutron beta-decay.

The singlet axial charge a_0 cannot be obtained in the same way from hyperon beta decays. Measurements of $g_1(x)$ like the one presented in this thesis therefore provide an important input to constrain a_0.

A fundamental sum rule formulated by Bjorken [Bjo70] relates the difference between the first moments of proton and neutron to the ratio g_A/g_V:

$$\Gamma_1^p - \Gamma_1^n = \frac{1}{6}\frac{g_A}{g_V} = 0.209. \tag{2.44}$$

The BJORKEN sum rule can be derived using only current algebra and isospin symmetry (Eq. (2.41)).

The less fundamental ELLIS-JAFFE sum rule [EJ74] assumes that the strange quark polarization is zero, $\Delta s + \Delta \overline{s} = 0$, and therefore $a_0 = a_8$:

$$\Gamma_1^{p,n} = \pm \frac{1}{12}(F + D) + \frac{5}{36}(3F - D). \tag{2.45}$$

For the proton and neutron integrals the ELLIS-JAFFE sum rule predicts

$$\Gamma_1^p = \int_0^1 g_1^p(x)\mathrm{d}x = 0.185 \pm 0.004 \tag{2.46}$$

$$\Gamma_1^n = \int_0^1 g_1^n(x)\mathrm{d}x = -0.024 \pm 0.004 \tag{2.47}$$

and a value of $\Delta\Sigma$ in the order of 0.58.

Both the BJORKEN and the ELLIS-JAFFE sum rule require QCD radiative corrections which amount — according to a calculation up to order α_s^2 [LV91] — to $\approx 15\%$ correction for the BJORKEN sum rule and $\approx 10\%$ correction for the ELLIS-JAFFE sum rule at $Q^2 = 5$ GeV^2 [FJ01].

A comparison of the mentioned sum rules with experimental data requires the evaluation of the integral $\int_0^1 g_1(x)\mathrm{d}x$ over the full x range from 0 to 1 at a fixed value of Q^2. Spectrometer acceptance and limited beam energy make it impossible to measure the full range in x at a constant Q^2 value. Using the experimentally well established Q^2 independence of the structure function ratio $g_1(x, Q^2)/F_1(x, Q^2)$ and the precisely measured Q^2 dependence of the spin-independent structure function $F_1(x, Q^2)$, the extracted $g_1(x, Q^2)$ values can be evolved to a common value of Q^2 as done in the analysis presented here.

As never the full x range from 0 to 1 is covered, extrapolations towards $x = 0$ and $x = 1$ are required in order to include the unmeasured regions into the integral. For $x \to 1$ the structure function $g_1(x)$ has to converge towards zero,

$$\lim_{x \to 1} g_1(x) = 0, \tag{2.48}$$

as $g_1(x)$ is proportional to a difference of quark distributions which fall off to zero for $x \to 1$ as observed in the spin-independent case. The extrapolation of $g_1(x)$ towards $x \to 0$ however is problematic as no clear x dependence can be predicted. For details see [FJ01] and references therein. Both the extrapolation $x \to 1$ and $x \to 0$ have not been the focus of the analysis presented here. The integrals are merely given in the x range covered by HERMES.

Extrapolations of the available world data on $g_1^p(x)$ and $g_1^n(x)$ towards low and high x with NLO QCD fits like published by the E155 collaboration [E15500] verify the BJORKEN sum rule but show a strong violation of the ELLIS-JAFFE sum rule. This may be interpreted as a hint that the assumptions the Ellis-Jaffe sum rule is based on (like e.g. zero strange sea polarization or $SU(3)_f$ symmetry) are not justified.

2.5 NLO QCD corrections to g_1

The naïve Quark Parton Model (QPM) introduced in Section 2.3 is not able to explain several facts which are observed experimentally. The assumption of collinear and free quarks e.g. leads to the prediction that $g_2(x) = 0$ which is in contradiction to experimental observations [E14398] [E155] [E15497a]. The QPM is also not able to explain the scaling violations seen in the structure functions. Furthermore, relativistic predictions for the total quark helicity in the nucleon (including the orbital angular momenta of the quarks) suggest $\Delta\Sigma \approx 0.58$ which is significantly larger than the experimentally determined values.

The reason for these inconsistencies between the QPM predictions and the experimental results is that the naïve QPM neglects fundamental processes which are described by next-to-leading order (NLO) QCD: quarks can radiate off and absorb gluons, gluons can fluctuate into quark-antiquark pairs, three or four gluons can couple at the same vertex and so on. This causes a Q^2 dependence of the structure functions in NLO QCD and leads to the following expression for $g_1(x, Q^2)$ [Rit02]:

$$\begin{aligned} g_1(x, Q^2) \quad = \quad & \frac{1}{2} \sum_q e_q^2 \int_x^1 \frac{\mathrm{d}y}{y} \Big[\Delta q^{NS}(\frac{x}{y}, Q^2)\ \Delta C_q^{NS}(y, Q^2) + \\ & + \frac{1}{N_f} \Delta\Sigma(\frac{x}{y}, Q^2)\ \Delta C_q^S(y, Q^2) + \\ & + \Delta G(\frac{x}{y}, Q^2)\ \Delta C_G(y, Q^2) \Big] \end{aligned} \tag{2.49}$$

where $\Delta\Sigma$ denotes the singlet quark distribution, $\Delta q^{NS}(x, Q^2)$ is the non-singlet quark distribution and the gluon distribution $\Delta G(x, Q^2)$ is defined analogue to (2.29) as

$$\Delta G(x, Q^2) = G^+(x, Q^2) - G^-(x, Q^2). \tag{2.50}$$

The coefficient functions $\Delta C_q^{NS}(x, Q^2)$, $\Delta C_q^S(x, Q^2)$ and $\Delta C_G(x, Q^2)$ can be expanded in powers of the strong coupling constant $\alpha_s(Q^2)$:

$$\Delta C_i(x, Q^2) = \Delta C_i^{(0)}(x) + \frac{\alpha_s(Q^2)}{2\pi}\ \Delta C_i^{(1)}(x) + \left(\frac{\alpha_s(Q^2)}{2\pi} \right)^2\ \Delta C_i^{(2)}(x) + ... \tag{2.51}$$

In leading order (LO) the spin-dependent gluon distribution does not contribute to $g_1(x, Q^2)$ because of $\Delta C_G^{(0)} = 0$.

In NLO the factorisation between the helicity distributions and the coefficient functions becomes scheme dependent but the different schemes are related by well-defined transformations. The so-called gluon axial anomaly or Adler-Bell-Jackiw anomaly [Adl69] makes it impossible that a factorisation scheme fulfils at the same time both gauge invariance and the conservation of chiral symmetry [Che96]. Obviously the choice of a factorisation scheme cannot change the measured quantity $g_1(x, Q^2)$ but rather affects the interpretation of the various helicity contributions in (2.49) relatively to each other:

Adler-Bardeen (AB) scheme. In the chirality conserving Adler-Bardeen scheme [AB69] the spin-dependent gluon distribution $\Delta G(x, Q^2)$ contributes to the first moment $\Gamma_1(Q^2) = \int_0^1 g_1(x, Q^2)\mathrm{d}x$ as the first moment of $\Delta C_G^{(1)}(x)$ is non-zero due to the Adler-Bell-Jackiw axial anomaly [AR88] [BFR96] [CCM88]. In the AB scheme the emission of a gluon with a certain helicity by a quark is linked to an increase of the orbital angular momentum of the quark-gluon system such that the *total* angular momentum is conserved: through the gluon emission ΔG increases, but at the same time the orbital angular momentum L_z also grows with opposite sign, while the total angular momentum remains unchanged [E14398].

Modified Minimal Subtraction ($\overline{MS}$) scheme. In the $\overline{MS}$ scheme $\Gamma_1(Q^2)$ doesn't depend directly on $\Delta G(x, Q^2)$ as $\Delta C_G^{(1)}(x) = 0$. The $\overline{MS}$ scheme is gauge invariant but chiral symmetry is violated, i.e. $q\overline{q}$ pairs created from gluons have the *same* helicity. Therefore a positive gluon polarization causes a negative sea-quark polarization.

The helicity distributions determined in the above mentioned schemes can be transformed into each other via the relations:

$$\Delta G(Q^2)_{\overline{MS}} = \Delta G(Q^2)_{AB} \tag{2.52}$$

$$\Delta\Sigma(Q^2)_{\overline{MS}} = \Delta\Sigma_{AB} - N_f \frac{\alpha_s(Q^2)}{2\pi}\Delta G(Q^2)_{AB}, \tag{2.53}$$

where N_f is the number of quark flavours which can contribute at a given Q^2.

The Q^2 evolution of the parton distributions $\Delta q^{NS}(x, Q^2)$, $\Delta\Sigma(x, Q^2)$ and $\Delta G(x, Q^2)$ can be calculated with the polarized Dokshitzer-Gribov-Lipatov-Altarelli-Parisi (DGLAP) equations [AP77] [GL72] [Lip75]:

$$\frac{\mathrm{d}}{\mathrm{d}\ln Q^2}\Delta q^{NS}(x, Q^2) = \frac{\alpha_s(Q^2)}{2\pi} P_{qq} \otimes \Delta q^{NS} \tag{2.54}$$

$$\frac{\mathrm{d}}{\mathrm{d}\ln Q^2}\begin{pmatrix} \Delta\Sigma(x, Q^2) \\ \Delta G(x, Q^2) \end{pmatrix} = \frac{\alpha_s(Q^2)}{2\pi}\begin{pmatrix} P_{qq} & 2N_f P_{qG} \\ P_{Gq} & P_{GG} \end{pmatrix} \otimes \begin{pmatrix} \Delta\Sigma \\ \Delta G \end{pmatrix} \tag{2.55}$$

with the convolution being defined as

$$(a \otimes b) = \int_x^1 \frac{\mathrm{d}y}{y}\, a\left(\frac{x}{y}\right) b(y). \tag{2.56}$$

The QCD splitting functions $\Delta P_{ij}(x/y)$ are a measure for the probability that a parton i with a momentum fraction x originates from a parton j with a momentum fraction $y > x$. P_{qq} describes the radiation of gluons from quarks, P_{qG} and P_{Gq} describe the production and annihilation of $q\overline{q}$ pairs by gluons and P_{GG} describes the interaction between gluons.

Chapter 3

The HERMES experiment

HERMES[1] is one of the four experiments installed at DESY's lepton-proton collider HERA (Fig. 3.1). The experiment was finally approved in summer 1993 after having demonstrated that high transverse electron beam polarizations could be reached routinely at HERA and that a smooth operation of internal storage cell targets was doable at other storage rings. Following a construction period of only 1 1/2 years, HERMES started data taking in early summer 1995.

The advantages of the HERMES experimental setup include high target polarizations without dilutions due to unpolarized substrates as known from solid state targets, a much higher target density than gas jet targets are able to deliver because of the storage cell technology and a spectrometer with large acceptance and excellent particle identification.

Measurements of the nucleon's spin structure require three main ingredients which will be briefly discussed in the following sections of this chapter: polarized leptons as electromagnetic probes, polarized nucleons as target and a spectrometer for the detection of the scattered particles.

3.1 The polarized HERA beam

HERA provides a proton beam with an energy of 920 GeV and an electron (positron) beam with an energy of 27.6 GeV, circulating in opposite directions in the two beam pipes of the storage rings with 6.3 km circumference. HERMES as a fixed target experiment uses only the electron beam, the proton beam is just passed through the experimental area. The electron beam consists of up to 220 bunches with a length of 27 ps separated by 96 ns. Typical currents at injection of the beam were around 35 mA in the 1996/97 data taking period and up to almost 50 mA in the 2000 data taking period. Over the beam lifetime of about 10 hours the current decreases

[1] The acronym *HERMES* stands for *HERA measurement of spin.*

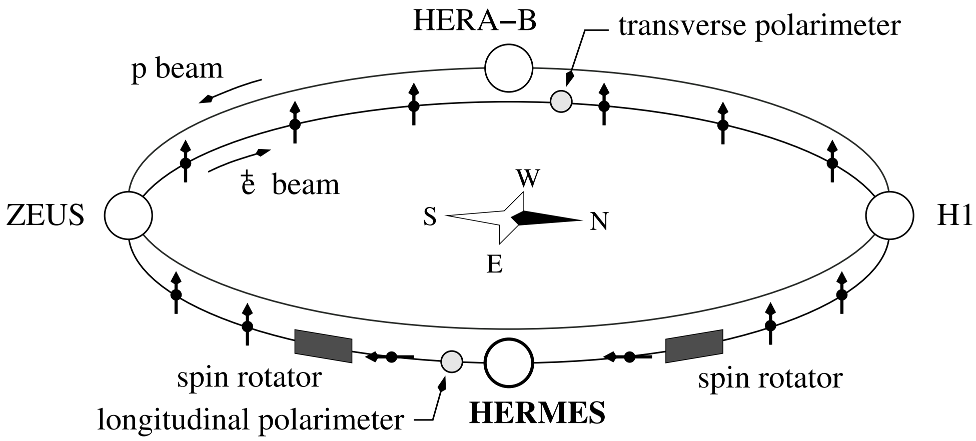

Figure 3.1: Sketch of the HERA facility at DESY. HERMES uses only the e^+ beam of the storage ring. The transverse spin polarization which builds up through the SOKOLOV-TERNOV mechanism is transformed into a longitudinal polarization in front of the HERMES experimental area by a set of magnets acting as a spin rotator. Behind HERMES the transverse polarization is restored by a second spin rotator. Two polarimeters monitor the degree of longitudinal respectively transverse beam polarization (compare Fig. 3.2).

exponentially and the beam is finally dumped when the current has reached $\sim$13 mA.

The beam becomes transversely spin-polarized due to the SOKOLOV-TERNOV effect [ST64], a tiny asymmetric spin flip amplitude involved in the synchrotron radiation process which favours an anti-parallel (parallel) spin-orientation in the final state relative to the field of the storage ring's bending magnets for electrons (positrons). Spin-flip synchrotron radiation is an extremely rare process – it is suppressed by ten orders of magnitude compared to 'normal' (non spin-flip) synchrotron radiation – but it has a large asymmetry as can be seen from the probabilities for an electron (positron) stored in HERA to flip its spin in one or the other direction with respect to the external magnetic field [Due]:

$$w^{\uparrow\downarrow} = \frac{1}{38.5\,\mathrm{min}} \qquad \text{and} \qquad w^{\downarrow\uparrow} = \frac{1}{16.2\,\mathrm{hrs}}. \tag{3.1}$$

As soon as the (initially unpolarized) beam has been ramped up to its final energy of 27.6 GeV the polarization begins to build up. Within a risetime of about 22 minutes typical polarizations between 50% and 60% are reached (see Fig. 3.2). The achieved polarization depends critically on how well one gets depolarizing factors like misalignement of magnets and depolarizing resonances under control.

In front of the HERMES target the transverse beam polarization is transformed into longitudinal polarization with a set of magnets acting as spin

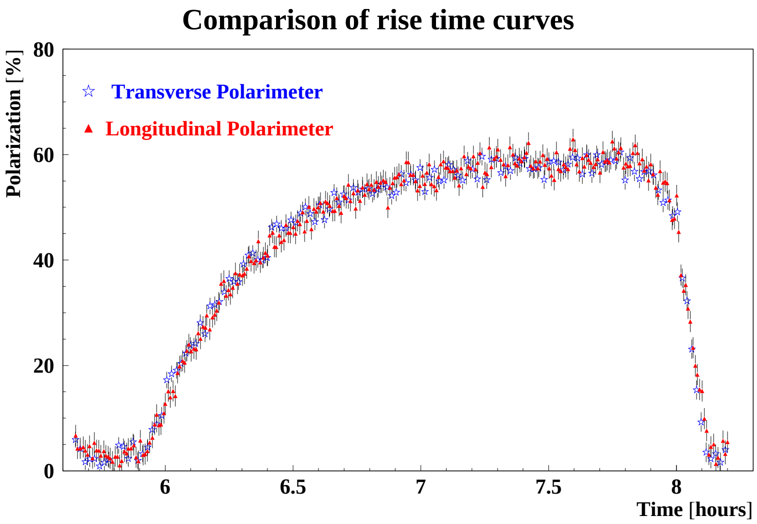

Figure 3.2: Polarization build-up through the SOKOLOV-TERNOV mechanism. Within a risetime of about 22 minutes typically polarizations between 50% and 60% are reached. The beam polarization is constantly monitored by two polarimeters.

rotator. Behind the HERMES experimental region a second spin rotator restores the transverse polarization before the beam enters the next arc.

Precise knowledge of the degree of beam polarization is absolutely essential for the analysis discussed here. The polarization is constantly monitored by two polarimeters, one measuring the longitudinal polarization [B$^+$02] downstream of the HERMES spectrometer and a second one on the opposite side of the ring in the region where the spin orientation is transverse [B$^+$93]. Both polarimeters exploit asymmetries in the COMPTON back scattering of polarized laser light hitting the lepton beam. The back-scattered photons are registered with calorimeters. The good agreement between the two polarization measurements is illustrated in Fig. 3.2.

3.2 The polarized gas target

HERMES uses a target of spin-polarized hydrogen or deuterium gas which is injected into an open ended storage cell installed in the vacuum of HERA so that the electron beam circulates through its center (see Fig. 3.3). Compared to the free atomic beam of a jet target this technology allows an increase of target density by about two orders of magnitude, delivering areal densities of $1 - 2 \times 10^{14}$ nucleons/cm^2. The disadvantage of a storage cell is that polarized atoms bouncing off its walls may loose their polarization and that the H (D) atoms can recombine to H_2 (D_2) molecules. To reduce

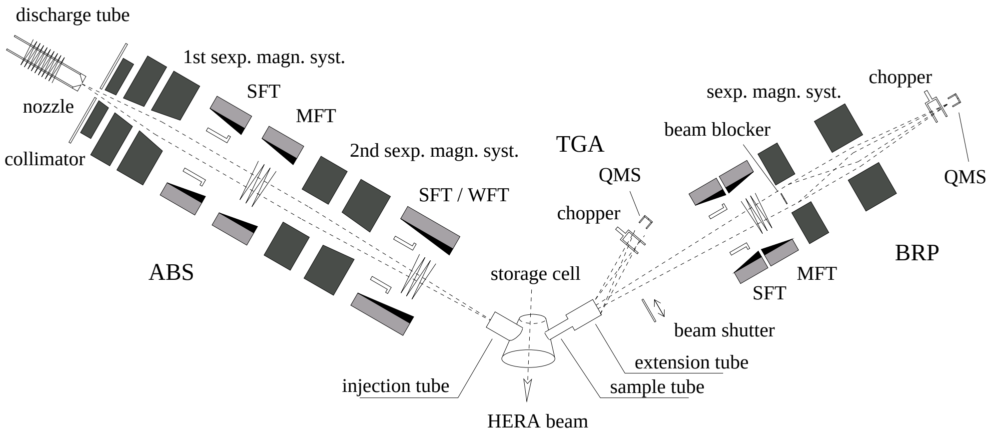

Figure 3.3: The HERMES target setup consists of an Atomic Beam Source (ABS) which injects polarized gas into a storage cell through which the HERA beam circulates. Polarized gas atoms are produced by a discharge tube dissociating the hydrogen or deuterium molecules and a system of sextupol magnetes and radio-frequency fields (labeled as SFT for strong field transition, MFT for medium field transition and WFT for weak field transition). Polarization and degree of dissociation are measured by a diagnostic system (BRP and TGA) on a sample of the target gas extracted out of the cell.

these effects, the interior of the target cell is coated with Drifilm (but also a simple layer of water ice works remarkably well for this purpose) and the cell is cooled to a temperature of 100 K.

The storage cell is as thin-walled as possible (75 μm aluminium) to reduce the probability for multiple scattering and bremsstrahlung for particles passing through its walls which would affect both angular and energy resolution. The cell has a length of 40 cm and an elliptical cross-section of 29.8 mm by 9.8 mm in the years 1996–1999 and of 21.0 mm by 8.9 mm in 2000. The center of the target cell is the origin of the HERMES coordinate system. Besides the injection tube through which polarized gas from an Atomic Beam Source (ABS) is fed in, the storage cell is equipped with a sample tube leading to a diagnostic system which consists of a Breit-Rabi Polarimeter (BRP) and a Target Gas Analyzer (TGA), measuring both polarization and degree of dissociation of the target gas sample extracted from the cell.

3.2.1 Atomic Beam Source

Polarized gas is produced by an Atomic Beam Source (ABS). H_2 (D_2) is dissociated into atomic hydrogen (deuterium) using a discharge tube and is then formed into an intense beam with small divergence by adiabatic expansion through a cooled nozzle and a set of collimators. From this initially unpolarized atomic beam one spin state of the electrons in the atom's shells is selected using the STERN-GERLACH effect: a system of sextupole magnets focuses atoms with the electron spin orientation $+1/2$ and deflects atoms which have the opposite spin orientation. A set of radio-frequency fields allows then to attain nuclear polarization by exchanging occupation numbers of hyperfine states via adiabatic high frequency transitions. Nuclear polarizations of up to 97% for hydrogen and up to 92% for deuterium were reached; the average values of the target polarization for the dataset analyzed here are listed in Table 4.4.

3.2.2 Target Gas Analyzer

The Target Gas Analyzer (TGA) measures the fraction of molecules (and therefore the degree of dissociation) in the gas sample extracted from the storage cell. It is essentially a quadrupole mass spectrometer (QMS) which separates mass 1 and mass 2 for hydrogen and mass 2 and mass 4 for deuterium. The HERMES target was able to reach degrees of dissociation of up to 92% for hydrogen and 95% for deuterium.

3.2.3 Breit-Rabi polarimeter

The polarization of the target gas is measured by a BREIT-RABI polarimeter (BRP). The BRP basically applies the same principles as the ABS in reverse order: the population of two or more hyperfine states is exchanged by radio-frequency fields and a system of sextupole magnets acts as electron spin filters, separating opposite electron spin states. A quadrupole mass spectrometer is used to count the rate of atoms in each hyperfine state. The hyperfine states are not measured all at the same time but one after another in a loop by varying the radio frequencies.

3.3 The HERMES Spectrometer

The HERMES detector (Fig. 3.4) is described in detail in [A$^+$98]. It is a forward spectrometer with a geometrical acceptance of ± 170 mrad horizontally and 40 to 140 mrad vertically, covering a range of scattering angles from 40 to 220 mrad. It consists of two identical detector halves (refered to as *top* and *bottom*) above and beneath the beam pipes. A horizontal septum plate shields the lepton and proton beams against the field of the spectrometer magnet.

3.3.1 The tracking system

The HERMES tracking system consists of a 1.3 Tm dipole magnet used for momentum measurement and in total 51 planes of wire chambers and six planes of microstrip gas detectors. These chambers contain wire planes in three different orientations: X planes with vertical wire orientation as well as U and V planes which are tilted by $\pm 30°$ with respect to the X planes. The wire chamber modules consist of six layers in $XX'UU'VV'$ configuration where the X', U', V' planes are offset by half a cell width with respect to the X, U, V planes to resolve right-left ambiguities.

Vertex Chambers VC 1/2. The Vertex Chambers are directly behind the exit window of the target chamber. In each detector half six planes of microstrip gas chambers with a cell width of 0.193 mm are grouped in two modules in the configuration VUX for VC 1 and XUV for VC 2. The Vertex Chambers were not operational during the 1999-2000 data taking period (deuterium target). To use the same tracking scheme for the whole dataset the information from the Vertex Chambers was also not taken into account for the tracking of the proton data taken in 1996 and 1997. The Vertex Chambers are mentioned here merely for completeness; they are irrelevant for the analysis discussed in this thesis.

Drift Vertex Chambers DVC. The DVCs, installed in 1996 and in operation since 1997, consist of six planes per detector half with in total 1088 wires in $XX'UU'VV'$ configuration, forming drift cells with a width of 6 mm. All drift chambers in the HERMES detector use a gas mixture consisting of $Ar/CO_2/CF_4$ (90:5:5). The spacial resolution per plane is $220\,\mu$m.

Front Chambers FC 1/2. The FCs are drift chambers which are installed in front of the spectrometer magnet. They consist of six planes per module in $UU'XX'VV'$ configuration with a cell width of 7 mm and provide a spacial resolution of $225\,\mu$m.

Magnet Chambers MC 1-3. Located inside the magnet gap, these multi-wire proportional chambers allow a momentum measurement for so-called *short tracks*, i.e. low momentum tracks which are bent out of the acceptance of the rear part of the spectrometer by the magnet's field. Each module consists of three planes in UXV configuration with a cell width of 2 mm, providing a resolution of 700 μm. As short tracks are not included in the analysis discussed here, these chambers are not relevant in this context and only mentioned for completeness.

Back Chambers BC 1/3 and 3/4. The purpose of the Back Chambers is the reconstruction of tracks after the charged particles have been deflected by the spectrometer magnet's field. These drift chambers consist of 7608 channels in $UU'XX'VV'$ geometry with a cell width of 15 mm and

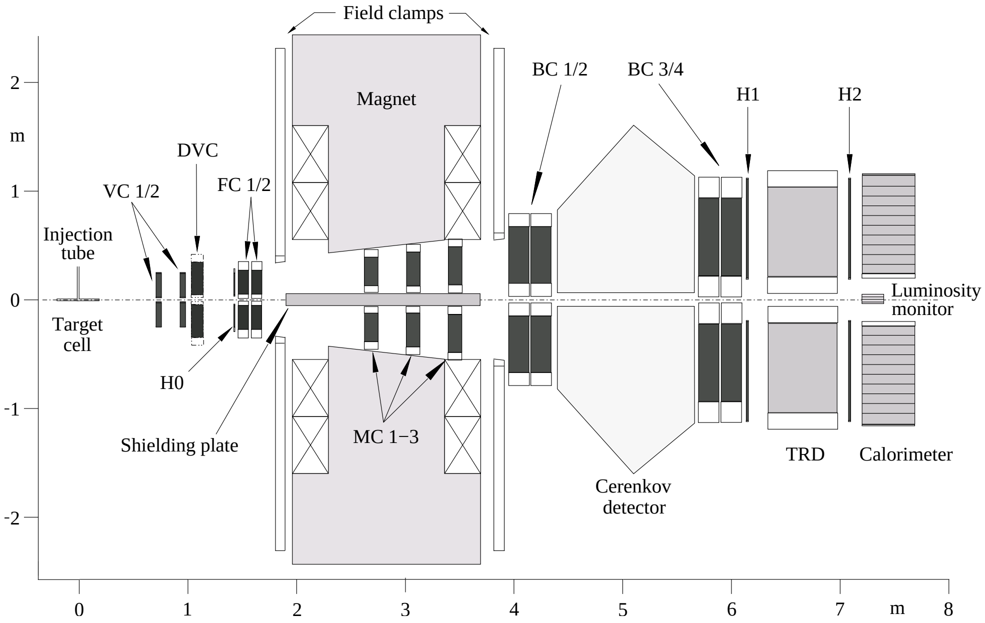

Figure 3.4: Side view of the HERMES Spectrometer. The beam enters from the left side and traverses the target cell centered at position (0, 0). A shielding plate protects the beam from being deflected by the spectrometer magnet's 1.3 Tm field.

an average resolution per plane of 275 μm (BC 1/2) respectively 300 μm (BC 3/4).

The tracking software `HRC (HERMES Reconstruction Code)` constructs with a fast tree-search pattern matching algorithm partial tracks as straight lines in front of and behind the spectrometer magnet based on the hits in the tracking chambers. In the next step these partial tracks are combined to full tracks and the momentum is determined using a look-up table [Wan]. For electrons in the momentum range of 3.5 to 27 GeV an average angular resolution of 0.3 - 0.6 mrad and an average momentum resolution $\Delta p/p$ of 0.7 - 1.3% (aside from bremsstrahlung tails) can be achieved[2] [Rit02].

3.3.2 The PID system

Cerenkov Detector

From 1995 till 1997 the HERMES Spectrometer was equipped with a threshold CERENKOV Detector which was used to separate pions from heavier hadrons in the momentum range up to 13.5 GeV. In 1998 this detector was replaced by a dual-radiator ring imaging CERENKOV detector (RICH) with

[2]the resolutions are slightly lower for data taken from 1998 on as the RICH detector introduced some additional material in the particle's path.

two radiators (silicia aerogel with an refractiv index of $n = 1.03$ and C_4F_{10} with $n = 1.0005$) which is described in detail elsewhere [A+02]. The RICH detector allows for the separation of pions, kaons and protons over almost the entire HERMES momentum range.

With respect to the data set analyzed here, this means that during the time the proton data were taken the threshold CERENKOV detector was installed and during the deuterium data taking period the RICH was operated.

Transition Radiation Detector

The radiator material of the Transition Radiation Detector, an array of polyethylene fibres with a diameter of ≈ 20 μm, was chosen in a way that only electrons produce transition radiation in the HERMES energy range. The transition radiation photons are detected with proportional chambers filled with a mixture of Xe/CH_4 (90:10). Per detector half six modules consisting each of a radiator and a proportional chamber are installed. The TRD rejects hadrons by a factor > 300 at an electron detection efficiency of 90%.

Pre-shower Hodoscope H2

The pre-shower hodoscope H2 consists of 42 vertical scintillator modules per detector half, preceded by two radiation lengths of lead. It provides pion rejection by about one order of magnitude with a detection efficiency for electrons of more than 90% as the probability for showers caused by leptons is much higher than for showers caused by hadrons.

Calorimeter

The Calorimeter consists of 420 blocks of radiation resistent F101 lead glass per detector half, arranged in a 42×10 array. The blocks have a front surface of 9×9 cm and a length of 50 cm which corresponds to approx. 18 radiation lengths. The energy of the showers developing in the blocks is measured by photomultiplier tubes which are connected to the back surface of each lead glass block.

The Calorimeter rejects pions by more than one order of magnitude at the first level trigger and by more than two orders of magnitude during offline analysis. For a reliable determination of the energy of electrons a high resolution and linearity of the signal is mandatory. The response of the calorimeter blocks to electrons of different energy was studied in a test beam and found to be linear within 1% over the whole relevant energy range from 1 to 10 GeV. The energy resolution can be parametrised as $\sigma(E)/E = (5.1 \pm 1.1) \times 10^{-2}/\sqrt{E[\mathrm{GeV}]} + (1.5 \pm 0.5) \times 10^{-2}$.

3.3.3 Trigger

The first level trigger for scattered electrons (`Trigger 21`) is formed by the coincidence of signals from the three hodoscope planes **H0, H1 and H2** and the **Calorimeter** where an energy deposition of more than 1.4 GeV in two adjacent columns of lead glass blocks is required. This trigger must appear in coincidence with the bunch signal from the accelerator (*'HERA clock'*) which is fired whenever a bunch of electrons passes the target cell.

The scintillator hodoscope **H0**, installed directly in front of the Front Chambers FC 1/2, has the purpose of suppressing triggers which are caused by showers originating from the proton beam pipe. A comparison between the time at which a signal in the front and the rear hodoscopes is registered allows to discriminate between forward and backward going particles.

The scintillator hodoscope **H1** is of identical design as the pre-shower hodoscope H2 already described above, but without the lead radiator in front of it.

3.3.4 Luminosity measurement

A precise measurement of the luminosity in each spin state is essential for the asymmetry measurement performed in this analysis. The **Luminosity Monitor** consists of a pair of small calorimeters installed left and right of the electron beam pipe, each consisting of 12 very radiation hard $NaBi(WO_4)_2$ CERENKOV crystals (22 mm $\times$ 22 mm $\times$ 200 mm), stacked in a 3$\times$4 array and covering a horizontal acceptance of 4.6 mrad to 8.9 mrad. The luminosity measurement uses the process of elastic scattering of beam particles off electrons of the target gas atoms: MØLLER scattering in the case of an electron beam and BHABHA scattering and e^+e^- annihilation in the case of a positron beam. The scattered particles exit the beam pipe at $x = 7.2$ m downstream of the center of the target cell and are detected by a coincidence measurement.

3.3.5 Data structures

The events observed by the HERMES detector are grouped into *bursts*, *runs* and *fills*. Events are continuously recorded whenever a trigger is accepted.

Every ten seconds the so-called *slow control information* like polarization, beam current, luminosity, detector status, etc. is read out. Events which fall into the interval between two successive scaler readings are collected in a burst and data quality has to be checked on this level[3]. The HERMES Data Quality Group provides official burst lists which contain for each individual burst information about its usability for analysis based on the slow control

[3] As HERA delivers continuously electron bunches, there in fact are no bursts like at other facilities. The notation burst has historical reasons as the design of the HERMES data aquisition system was taken over from another experiment.

data. These burst lists have been used for all data quality checks in the analysis discussed here.

When events are written to disk they are stored in files which are successively numbered. These files are called runs. Their maximum size is simply determined by technical reasons. A run usually contains several thousand events which belong to hundreds of different bursts.

A fill incloses the amount of runs taken during one fill of the HERA electron ring from the beginning of data taking after injection, ramping and tuning of the beam until the end of data taking shortly before the beam is dumped.

Chapter 4

Data analysis

4.1 Dataset

The measurement of the inclusive asymmetries $A_{||}^p$ and $A_{||}^d$ described in this chapter is based on data taken in 1996/97 on a proton target and in 2000 on a deuterium target. For the analysis the latest available well-calibrated data productions 96d0, 97d0 and 00c1 were used.

For all three productions the same tracking method (`NOVC`) was applied which eliminates artefacts due to varying efficiencies and resolutions of different tracking schemes[1]. This allows a consistent extraction of the neutron structure function based on the deuterium and proton measurements.

The available statistics after all cuts is listed in Table 4.1.

4.2 Data quality

To ensure good quality of the data included into this analysis the official burst list provided by the HERMES Data Quality Group was used. Data taken during periods when one or more of the PID or tracking detectors were not fully operational (e.g. due to high voltage trips) were discarded. Also periods during which problems with the Data Acquisition System occured or when the trigger dead time exceeded 50% were rejected. To suppress data with very low polarization which don't contribute significantly to the asymmetry measurement a minimum target polarization of 50% and a minimum beam polarization of 30% were required. In addition a cut on a minimum beam current of 5 mA was used. Obviously wrong values which never occured during data taking (like unreasonable long bursts, beam polarizations and currents which have never been reached, etc.) were discarded, too.

[1] In previous productions of the 1997 data for example the Vertex Chambers were included into the tracking algorithm (`STD` tracking). These Vertex Chambers were not available in the 1996 and 2000 data taking periods. The efficiency and resolution of tracking performed with/without Vertex Chambers is different.

year	production	target	# DIS $\uparrow\downarrow$	# DIS $\uparrow\uparrow$	# DIS (total)
1996	96d0	p	520 K	494 K	$1,014$ K
1997	97d0	p	$1,399$ K	$1,320$ K	$2,719$ K
2000	00c1	d	$5,242$ K	$5,119$ K	$10,361$ K

Table 4.1: Statistics of the available data set after applying all data quality criteria. The analysis presented here is based on 3.7 million DIS events for polarized hydrogen and 10.7 million DIS events for polarized deuterium.

If only one detector half (top or bottom) of the HERMES Spectrometer was affected by data quality problems, events registered with the other detector half were analyzed since for an inclusive measurement only one detector half is needed to register an event.

4.3 Particle identification

The HERMES Particle Identification (PID) system provides already at the trigger level a hadron suppression by about one order of magnitude; in offline analysis hadrons can be suppressed by four orders of magnitude with respect to the total number of hadrons [HERMES05b]. The efficiency for identifying electrons (and positrons) is above 96% with a hadron contamination of less than 0.2% [HERMES05a].

The HERMES PID algorithm uses BAYESian statistics with conditional probabilities [Wen01]. The conditional probability $P(A|B)$ is defined as the probability that hypothesis A is true when B was observed. In case of PID there are two hypothesis: H_l (=observed particle was a lepton) and H_h (=observed particle was a hadron). The PID determination is based on three observables: the response r of the considered PID detector as well as the momentum p and the polar scattering angle θ of the particle. The conditional probability $P(H_{l(h)}|r,p,\theta)$ that one of the hypotheses $H_{l(h)}$ is true based on those three observables is

$$P(H_{l(h)}|r,p,\theta) = \frac{P(H_{l(h)}|p,\theta)\;P(r|H_{l(h)},p)}{P(H_l|p,\theta)\;P(r|H_l,p) + P(H_h|p,\theta)\;P(r|H_h,p)}. \tag{4.1}$$

The terms $P(r|H_{l(h)},p)$, the so-called *parent distributions*, describe typical detector responses caused by leptons (hadrons) with a given momentum p. These parent distributions have been extracted for each of the PID detectors from clean samples of leptons (hadrons) isolated with very restrictive cuts on the other PID detectors.

The fluxes of leptons and hadrons (depending on momentum and scattering angle) are determined in an iterative procedure. In the beginning uniform fluxes are assumed,

$$P(H_l|p,\theta) = P(H_h|p,\theta), \tag{4.2}$$

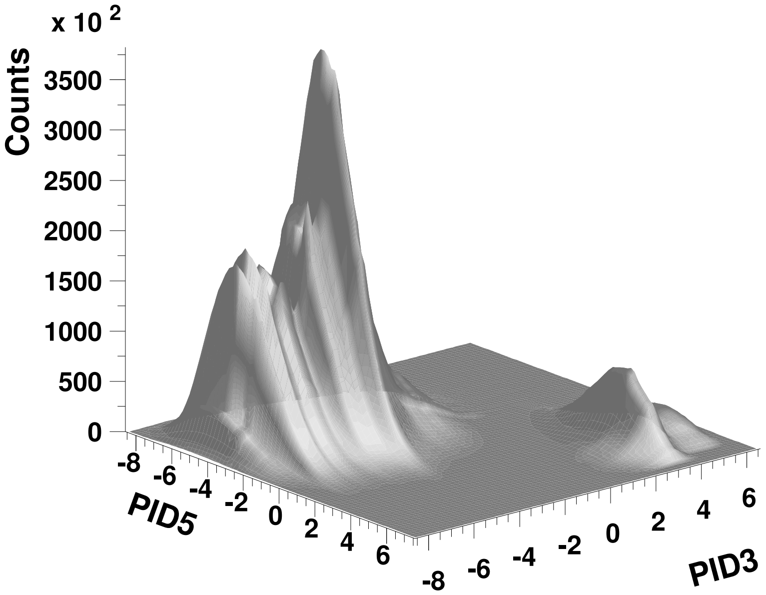

Figure 4.1: PID3 vs. PID5 [HERMES05b]

such that the ratio of conditional probabilities for finding leptons $P(H_l|r,p,\theta)$ and hadrons $P(H_h|r,p,\theta)$ simplifies to the ratio of the parent distributions (– for convenience the decadic logarithm is taken),

$$\log_{10}\frac{P(H_l|r,p,\theta)}{P(H_h|r,p,\theta)} = \log_{10}\frac{P(r|H_l,p)}{P(r|H_h,p)} \equiv \mathrm{PID}_{\mathrm{det}}, \tag{4.3}$$

which is defined as the PID value for the respective detector whose parent distributions were used in the calculation. Such $\mathrm{PID}_{\mathrm{det}}$ values are defined for the four relevant PID detectors: TRD, calorimeter, pre-shower and Cerenkov/RICH. To optimize the values for the particle fluxes $P(H_{l(h)}|p,\theta)$ the calculated ratio Eq. (4.3) is compared to data and the fluxes are varied until a good approximation is reached.

The PID value of the TRD is defined as PID5, the sum of the other three detector PID values is defined as PID3,

$$\begin{aligned}\mathrm{PID3} &\equiv \mathrm{PID}_{\mathrm{calorimeter}} + \mathrm{PID}_{\mathrm{pre-shower}} + \mathrm{PID}_{\mathrm{Cerenkov/RICH}} \\ \mathrm{PID5} &\equiv \mathrm{PID}_{\mathrm{TRD}}. \end{aligned} \tag{4.4}$$

Figure 4.1 shows the distribution of these values in a two-dimensional surface plot [HERMES05b]. The smaller bump in the corner where both PID3 and PID5 are positive corresponds to the lepton sample which is clearly separated from the other maxima which correspond to the hadron sample.

The final PID value used for the identification of leptons in this analysis is defined as follows:

$$\mathrm{PID} = \mathrm{PID3} + \mathrm{PID5} - \log_{10}\,\Phi \tag{4.5}$$

where Φ is the ratio of hadron and lepton fluxes,

$$\Phi = \frac{P(H_h|p,\theta)}{P(H_l|p,\theta)}. \tag{4.6}$$

Choosing a PID cut means optimizing the tradeoff between efficiency and purity of the selected sample: a very restrictive cut will produce a clean sample at the cost of statistics. In this analysis a cut of PID > 1 for the identification of leptons was found to be optimal, corresponding to the electron identification efficiency $> 96\%$ with a negligible hadron contamination ($< 0.2\%$) already mentioned at the beginning of this section.

4.4 Event selection

The cuts used to select DIS events are listed in Table 4.2. If an event contains more than one lepton only the lepton with highest energy (the so-called *leading lepton*) is taken into account. A cut on the charge of the detected lepton makes sure that the observed particle can originate from the incident beam (compare also Section 4.6). To extend the kinematic range to very low values of x the usual cut of $Q^2 > 1\,\mathrm{GeV}^2$ for hard scattering events has been reduced to $Q^2 > 0.1\,\mathrm{GeV}^2$ (but the binning was chosen in a way that the kinematic region $0.1\,\mathrm{GeV}^2 < Q^2 < 1\,\mathrm{GeV}^2$ can be easily separated from the region with $Q^2 > 1\,\mathrm{GeV}^2$ as will be seen in Section 4.5).

A cut on $W^2 > 3.24\,\mathrm{GeV}^2$ rejects events from the nucleon resonance region.

The upper and lower cuts on y are motivated by considerations concerning detector performance. A cut of $y < 0.91$ corresponds to an energy E' of the scattered lepton of more than 2.4 GeV which assures that the calorimeter efficiency has reached its plateau of almost 100%. The lower cut on $y > 0.1$ guarantees sufficient detector resolution as will be explained in detail in Section 4.5.

To assure that the detected lepton originates from a scattering event inside the target cell (and not from background due to electromagnetic showers, collimator scattering, etc.) a cut on the vertex position is imposed: the vertex has to be located in the range of ± 18 cm along the beam axis[2] and within a radial distance from the beam of 0.75 cm which envelops the target cell volume in good approximation.

[2]The origin of the HERMES coordinate system is the center of the target cell, $x = y = z = 0$.

$0.002 <$	x	< 0.900	$\mathrm{PID} = \mathrm{PID3} + \mathrm{PID5} - \log_{10}\Phi \geq 1$
$0.10 <$	y	< 0.91	electric charge = beam charge
$0.1\ \mathrm{GeV}^2 <$	Q^2		$\lvert z_{\mathrm{Vertex}}\rvert < 18\,\mathrm{cm}$
$3.24\ \mathrm{GeV}^2 <$	W^2		$\lvert d_{\mathrm{Vertex}}\rvert < 0.75\,\mathrm{cm}$
			Fiducial Volume Cuts

Table 4.2: Cuts imposed on event level

The geometrical acceptance of the HERMES spectrometer restricts the accessible kinematic region as illustrated in Fig. 4.4 by the curves indicating polar scattering angles of $\Theta = 0.22$ rad and $\Theta = 0.04$ rad. To reject tracks which might be affected by edge effects of the spectrometer a set of geometrical cuts is used collectively refered to as *Fiducial Volume Cuts (=FVCs)*. These cuts discard e.g. tracks which point to edge / corner blocks of the calorimeter as there the energy measurement might be compromised by part of the electromagnetic shower developing outside the active detector volume. The FVCs also reject events where tracks run very close to detector mountings, shielding material, etc. where the particles might cause electromagnetic showers.

As a whole the combination of cuts discussed above allows an analysis in the x range $0.002 < x < 0.9$.

4.5 Binning

In previous inclusive analyses of the HERMES data [Gae01] [DN] [Wei] a two-dimensional binning in x and y had been used (Fig. 4.2) consisting of 27 bins evenly spaced in $\ln x$ and up to three bins in y, resulting in 49 bins in total. In these analyses corrections for detector smearing effects were omitted and radiative corrections were accounted for in a different way than in the analysis presented in this thesis.

As soon as these effects were fully taken into account by applying the unfolding method (which will be described in Chapter 5) it became clear that binning the measured asymmetry in this way leads to an unacceptable large inflation of the uncertainty, especially in the high x region ($x > 0.2$).

Extensive studies yielded the somewhat surprising result that this problem was not caused by a binning which was too fine but by a binning which was too coarse. In the high x region the acceptance of HERMES covers a large range in y as can be seen in Fig. 4.2. Low values in y are correlated with low ν and therefore high energies E' of the scattered electron ($y = \nu/E = (E - E')/E$). With higher and higher energies the resolution of the spectrometer degrades more and more; the cut of $y < 0.1$ (corresponding to $E' = 24.8\,\mathrm{GeV}$) is in fact a cut to discard a kinematic region where the

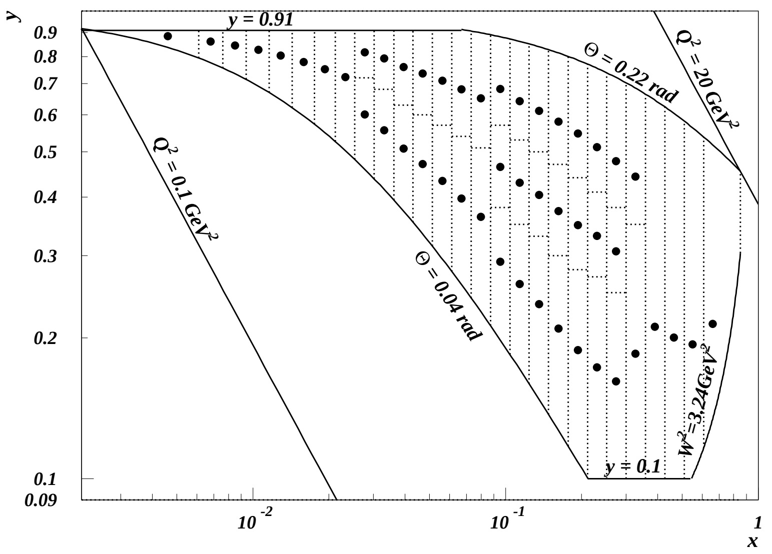

Figure 4.2: Kinematic $x-y$ binning used in previous analyses [Gae01] [DN] [Wei].

degradation of detector resolution is no longer acceptable (see Fig. 4.5). In the old binning the highest x bins used to be undivided in y, therefore contaminating data with very good resolution (at high values of y) with data of barely acceptable resolution (at low values of y). Furthermore the bin width in x turned out to be too narrow to be compatible with the achievable resolution in the high x and low y region. This caused the mentioned blow-up of error bars (the unfolding procedure had to apply huge corrections due to detector smearing) and required a complete rearrangement of the binning.

The true advantage of subdividing the high x bins along y becomes obvious considering the influence of the depolarisation factor D (Eq. 2.16). As already seen in Section 2.2 D depends strongly on y, i.e. virtual photons which carry a large fraction y of the energy of the incident lepton also have a high probability to retain its spin whereas for low energetic photons the opposite holds true[3].

Asymmetry values measured in kinematic regions affected by low polarization of the virtual photons (low y) have much less impact on the significance of the A_1 measurement than asymmetry values from regions with high virtual photon polarization (high y). Thus the low y region where detector smearing becomes critical is naturally suppressed, contributing only

[3] $D \approx y$ is already a good first approximation. The name ***de**polarization factor* is somewhat misleading: D denotes the fraction of the longitudinal lepton beam polarization transferred to the virtual photons. For $D = 1$ the virtual photons have in 100% of cases the same polarization as the leptons, i.e. they are totally polarized. For low values of y the depolarization factor has also small values, meaning that the polarization transferred from the beam to the virtual photons is small (i.e. the depolarization is high).

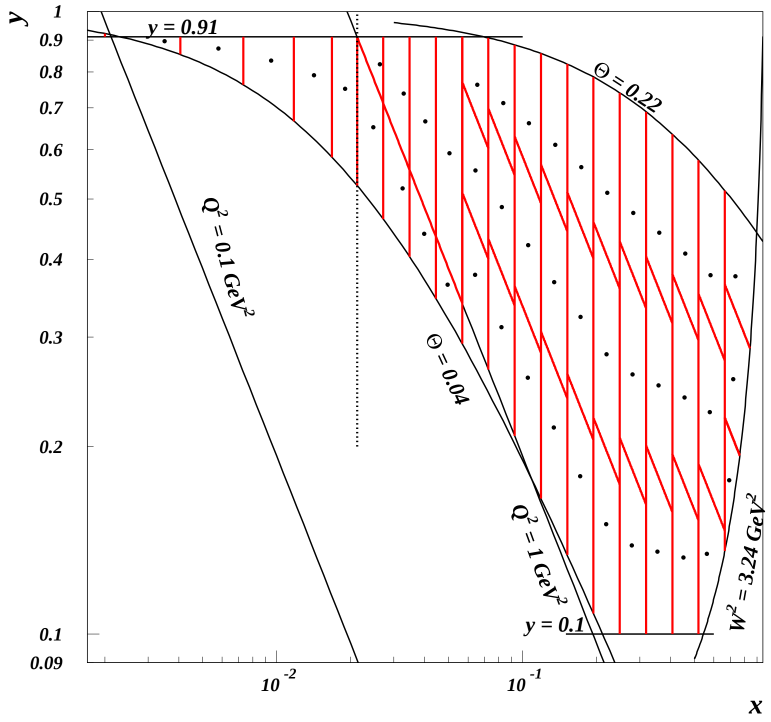

Figure 4.3: New $x-Q^2$ binning used in this analysis, shown in the $x-y$ kinematic plane (please compare also Fig. 4.4) [CDNE+04a].

marginally to the final result. Splitting the high x bins along y is therefore extremely beneficial[4].

After extensive efforts to optimize the binning finally a two-dimensional binning in x and Q^2 (Fig. 4.4) was chosen for this analysis. This is the same binning as shown in Fig. 4.3 in the variables x and y. It can be seen that the bin boundaries along constant values of Q^2 serve well to subdivide the x bins along y although they are not as ideal as bin boundaries along constant y values would be. This (minor) drawback is compensated for by advantages regarding the presentation of the data. For example a common bin boundary at $Q^2 = 1\,\mathrm{GeV}^2$ allows an effortless separation of the traditional DIS region

[4] This raises the question why not to apply the depolarization factor already on an event by event basis, e.g. by using it as a weight. It turns out that this is not practicable as the unfolding algorithm requires $A_{||}$ as input as we will see in Chapter 5. Unfolding changes the average kinematic values in each bin, including the value of y. Applying the depolarization factor calculated from the measured quantities would be incorrect, as these quantities are already affected by smearing. After unfolding the Born level kinematics is retrieved, but now there are no longer individual events as the unfolding cannot correct single events but only event samples. Therefore the depolarization factor has to be applied bin-wise *after* unfolding, calculated with the regained average kinematic values on Born level.

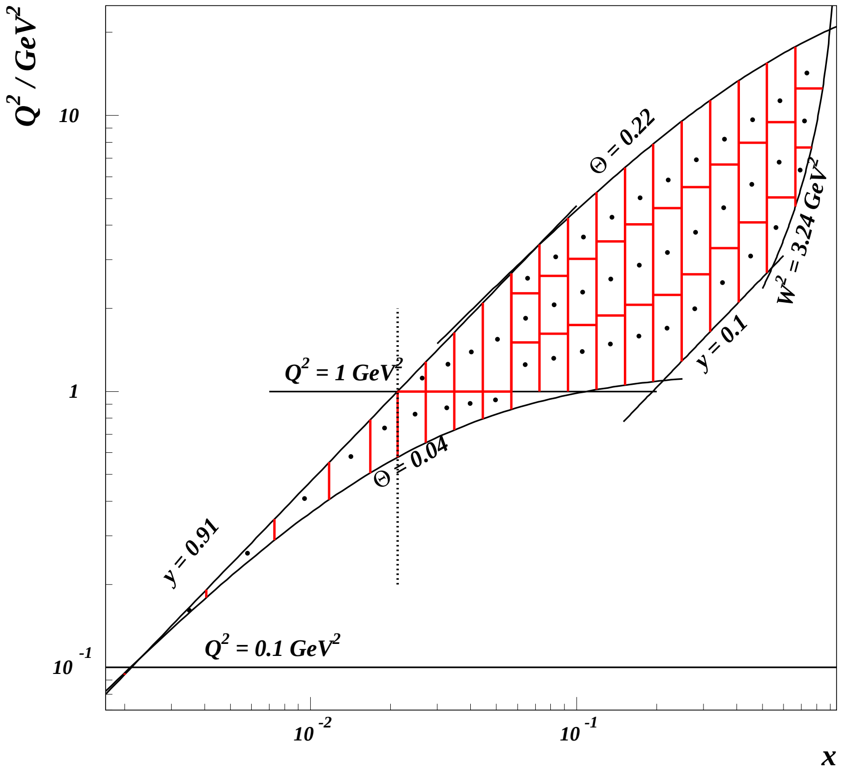

Figure 4.4: Kinematic $x - Q^2$ binning used in this analysis [CDNE+04a]. The values of the bin boundaries are given in Appendix C.

($Q^2 > 1$ GeV^2) from the region with lower Q^2 values whereas the use of a $x - y$ binning would require a complete re-analysis for $Q^2 > 1$ GeV^2 to achieve this.

To gain equally populated bins logarithmically equidistant spaced bin boundaries in x (according to the shape of the DIS cross section) have been chosen. Only at very low x values and for the highest x bin the bin width has been increased to compensate for a lack of statistics due to phase space restrictions.

In total 20 x bins have been subdivided in up to three Q^2 bins, resulting in 46 $x - Q^2$ cells (see Appendix C). The kinematic region $x > 0.2$ which couldn't be reasonably unfolded with the old binning is now divided into 18 $x - Q^2$ bins (instead of previously 12 $x - y$ bins) and despite the higher number of bins the errors are completely under control.

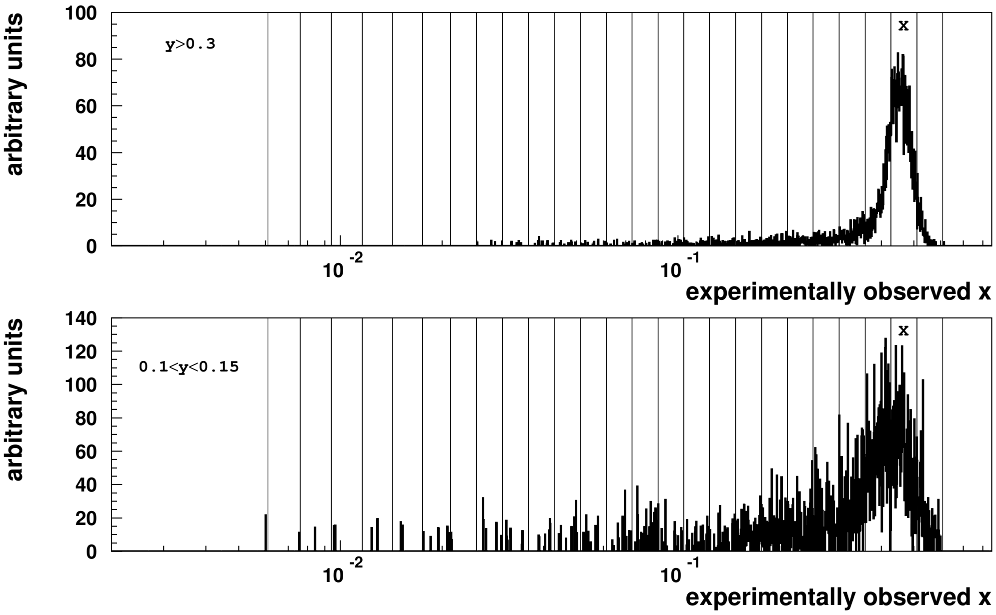

Figure 4.5: The resolution is for higher values of y (upper panel, $y > 0.3$) significantly better than in the region of very low y values (lower panel, $0.1 < y < 0.15$) as visible in these x distributions. All electrons originate from the bin marked with 'X' and were reconstructed after a detailed Monte Carlo simulation of the HERMES detector had been applied.

4.6 Correction for charge symmetric background

The analyzed dataset contains a certain amount of leptons which pass all DIS and geometrical cuts listed in Table 4.2 apart from the cut concerning their electrical charge. These events appear with respect to their kinematics and PID exactly like the process we want to measure — except for the fact that they *cannot* stem from beam particles as they have the wrong charge (e.g. e^- in case of an e^+ beam).

The origin of these particles are charge symmetric (cs) processes like $\gamma \longrightarrow e^+e^-$. Hence there is a second sample of leptons (built up from their counterparts in these cs reactions) which have the *same* charge as the incident beam, therefore passing *all* the cuts given in Table 4.2 and diluting the DIS sample. Charge symmetric background is negligible at high values of x but contributes in the low x regime up to $\approx 20\%$ of the observed events [Wei].

To correct for this effect events with opposite beam charge are subtracted bin by bin from the observed yields per spin orientation:

$$N^{\uparrow\uparrow} \equiv N^{\uparrow\uparrow}_{\mathrm{DIS}} = N^{\uparrow\uparrow}_{\mathrm{obs}} - N^{\uparrow\uparrow}_{\mathrm{cs}} \quad \text{and} \quad N^{\uparrow\downarrow} \equiv N^{\uparrow\downarrow}_{\mathrm{DIS}} = N^{\uparrow\downarrow}_{\mathrm{obs}} - N^{\uparrow\downarrow}_{\mathrm{cs}}. \qquad (4.7)$$

Also the average values $\langle x \rangle$, $\langle y \rangle$, $\langle Q^2 \rangle$, etc. are corrected by including these events with a weight of -1. This is reasonable as due to the symmetry of the cs processes both the e^- and the e^+ sample have identical kinematic distributions.

4.7 Measured asymmetries

The cross section asymmetry $A_\parallel$ is calculated from the background corrected counting rates (4.7) as

$$A_\parallel = \frac{\sigma^{\uparrow\downarrow} - \sigma^{\uparrow\uparrow}}{\sigma^{\uparrow\downarrow} + \sigma^{\uparrow\uparrow}} = \frac{N^{\uparrow\downarrow} L^{\uparrow\uparrow} - N^{\uparrow\uparrow} L^{\uparrow\downarrow}}{N^{\uparrow\downarrow} L_P^{\uparrow\uparrow} + N^{\uparrow\uparrow} L_P^{\uparrow\downarrow}} \tag{4.8}$$

where $L^{\uparrow\uparrow}$ and $L^{\uparrow\downarrow}$ are the dead-time[5] corrected luminosities

$$\begin{aligned} L^{\uparrow\uparrow(\uparrow\downarrow)} &= \int_{\uparrow\uparrow(\uparrow\downarrow)} dt\, \mathcal{L}(t)\, \tau(t) \qquad (4.9) \\ &= \sum_{\uparrow\uparrow(\uparrow\downarrow)} \text{burst duration} \times \text{lumi rate} \times \frac{\#\ \ \text{accepted triggers}}{\#\ \text{generated triggers}} \end{aligned}$$

and $L_P^{\uparrow\uparrow}$ and $L_P^{\uparrow\downarrow}$ are the dead-time corrected luminosities weighted with the absolute values of beam and target polarization,

$$\begin{aligned} L^{\uparrow\uparrow(\uparrow\downarrow)} &= \int_{\uparrow\uparrow(\uparrow\downarrow)} dt\, \mathcal{L}(t)\, \tau(t)\ \ |P_{\text{beam}}(t)\, P_{\text{target}}(t)| \qquad (4.10) \\ &= \sum_{\uparrow\uparrow(\uparrow\downarrow)} \text{burst duration} \times \text{lumi rate} \times \frac{\#\ \ \text{accepted triggers}}{\#\ \text{generated triggers}} \times \\ &\qquad \times |P_{\text{beam}}(t)\, P_{\text{target}}(t)|. \end{aligned}$$

The luminosities are summed up separately for both detector halves to account for periods when data of one detector half is discarded due to data quality problems. Only bursts with good data quality (i.e. where the measured events enter the analysis) contribute to the luminosity. The sums in Eqns. (4.9) and (4.10) indicate how the luminosity integration is done technically: for each burst the product of burst duration, coincidence rate measured by the luminosity monitor[6], trigger dead time and in case of Eq. (4.10) magnitude of beam and target polarization is summed up for the two spin states separately.

As the beam polarization P_{beam} is measured on the time scale of the length of bursts ($\approx$ 10 seconds) it shows fluctuations because of limited statistics. Therefore a fit is calculated during offline data production, smoothing out those fluctuations. The average beam polarization values during the relevant data taking periods are listed in Table 4.3.

[5] A typical value for the dead-time correction factor τ is ≈ 0.97 which corresponds to a trigger dead-time of 3%.

[6] smoothed by a fit, μDST field `g1Beam.rLumiFitBstGai`

year	$\langle P_{\text{beam}} \rangle$	fractional uncertainty
1996	0.528	3.4 %
1997	0.531	3.4 %
2000	0.533	1.9 %

Table 4.3: Average beam polarization values for the 1996, 1996 and 2000 data taking periods [HERMES05b]. In the analysis the actual beam polarization at the time of data taking (smoothed by a fit) was used.

year	target gas	$\langle P_{\text{target}} \rangle$	systematic uncertainty
1996	hydrogen	$\pm$ 0.759 $\pm$ 0.042	5.5 %
1997	hydrogen	$\pm$ 0.850 $\pm$ 0.032	3.8 %
2000	deuterium	+ 0.851 $\pm$ 0.031	3.6 %
		− 0.840 $\pm$ 0.028	3.3 %

Table 4.4: Average target polarization values for the 1996, 1996 and 2000 data taking periods [Bec03] [CDNE$^+$04a].

The stability of the target performance allowed to use constant average values for the target polarization P_{target} [Bec03] as listed in Table 4.4.

For technical reasons the cross-section asymmetry (4.8) is in an intermediate step calculated independently for the two detector halves of the HERMES spectrometer ($A_\parallel^{\text{top}}$ and $A_\parallel^{\text{bot}}$) and then combined to the total asymmetry $A_\parallel$. This has the advantage that in $A_\parallel^{\text{top}}$ and $A_\parallel^{\text{bot}}$ many systematic detector effects cancel. The two detector halves have e.g. slightly different acceptances; as the acceptance is spin-independent this effect cancels in the asymmetry for every detector half making a later acceptance correction for the combined asymmetry $A_\parallel$ unnecessary.

The calculation of the statistical errors on the measured cross-section asymmetry $A_\parallel$ has to take into account the statistical errors of the subtracted charge symmetric background contributions. With Eq. (4.7) we can write Eq. (4.8) as

$$A_\parallel = \frac{(N_{\text{obs}}^{\uparrow\downarrow} - N_{\text{cs}}^{\uparrow\downarrow})L^{\uparrow\uparrow} - (N_{\text{obs}}^{\uparrow\uparrow} - N_{\text{cs}}^{\uparrow\uparrow})L^{\uparrow\downarrow}}{(N_{\text{obs}}^{\uparrow\downarrow} - N_{\text{cs}}^{\uparrow\downarrow})L_P^{\uparrow\uparrow} + (N_{\text{obs}}^{\uparrow\uparrow} - N_{\text{cs}}^{\uparrow\uparrow})L_P^{\uparrow\downarrow}} \tag{4.11}$$

with the statistical error

$$\begin{aligned} \Delta A_\parallel \quad = \quad & \frac{L^{\uparrow\downarrow}L_P^{\uparrow\uparrow} + L_P^{\uparrow\downarrow}L^{\uparrow\uparrow}}{(N_{\text{DIS}}^{\uparrow\downarrow}L_P^{\uparrow\uparrow} + N_{\text{DIS}}^{\uparrow\uparrow}L_P^{\uparrow\downarrow})^2} \times \qquad (4.12) \\ & \times\sqrt{(N_{\text{DIS}}^{\uparrow\downarrow})^2(N_{\text{DIS}}^{\uparrow\uparrow} + 2N_{\text{cs}}^{\uparrow\uparrow}) + (N_{\text{DIS}}^{\uparrow\uparrow})^2(N_{\text{DIS}}^{\uparrow\downarrow} + 2N_{\text{cs}}^{\uparrow\downarrow})}. \end{aligned}$$

The charge symmetric background corrected asymmetries $A_{\parallel}^{p}$ and $A_{\parallel}^{d}$ for proton and deuteron are shown in Figs. 4.6 and 4.7. The upper panels show the asymmetries in the two-dimensional binning illustrated in Fig 4.4. The different branches formed by two or three asymmetry values for the same x range belong to x bins which are subdivided in two or three Q^2 bins. Lower points for a given value of x belong to bins with low $\langle Q^2 \rangle$ and low $\langle y \rangle$ values, higher points to higher $\langle Q^2 \rangle$ and higher $\langle y \rangle$ values. This splitting is understandable in consideration of the depolarization factor $D(y) \approx y$: low values of y correspond to small virtual photon polarizations, therefore leading to smaller measured values of the asymmetries $A_{\parallel}^{p,d}$.

The asymmetries in the upper panels of Figs. 4.6 and 4.7 will be corrected for QED radiative effects and detector smearing with the method described in the next chapter. The Q^2 averaged version of the asymmetries shown in the lower two panels are merely meant as an illustration to give an idea of the magnitude of the asymmetries when averaging over the Q^2 bins.

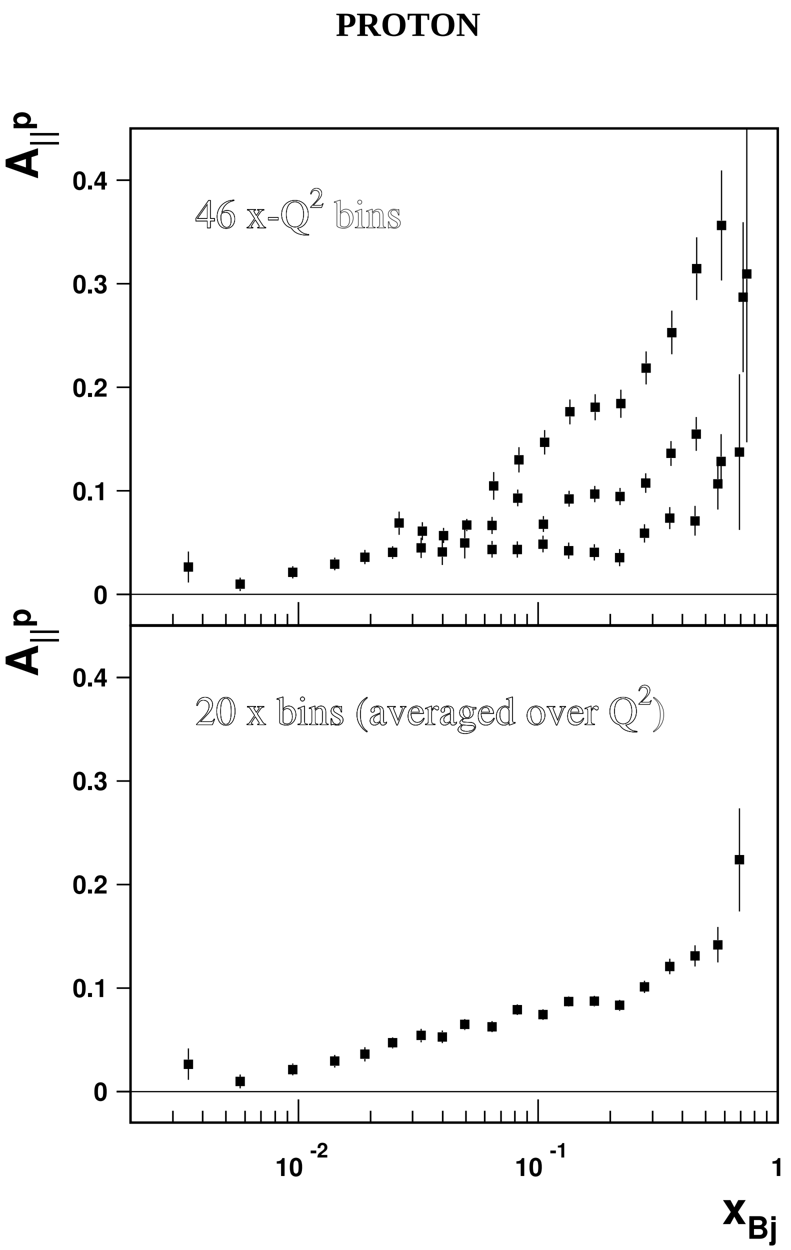

Figure 4.6: Measured asymmetry $A_{\|}^{p}$ after correction for charge symmetric background contributions. The error bars show only statistical errors. The asymmetry values shown in the upper panel (in a two-dimensional $x - Q^2$ binning) will be unfolded for smearing caused by QED radiative and detector effects with the method explained in Chapter 5.

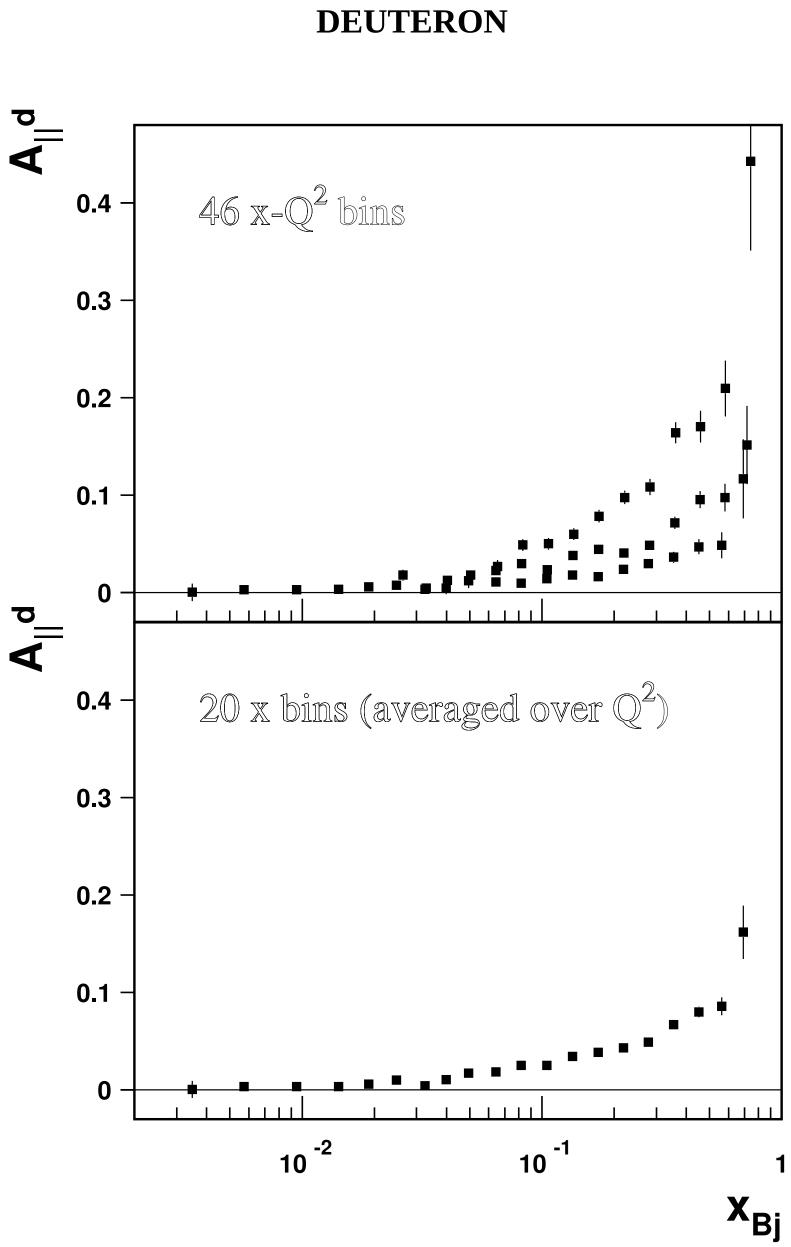

Figure 4.7: Measured asymmetry $A_{\|}^{d}$ after correction for charge symmetric background contributions. The error bars show only statistical errors. The asymmetry values shown in the upper panel (in a two-dimensional $x - Q^2$ binning) will be unfolded for smearing caused by QED radiative and detector effects with the method explained in Chapter 5.

Chapter 5

Unfolding

5.1 The general idea

The experimentally observed asymmetries extracted in the previous chapter (Figs. 4.6 and 4.7) are distorted by both higher order QED radiative effects and detector smearing as illustrated in Figure 5.1. To correct for this and retrieve the wanted BORN [1] asymmetries an unfolding algorithm [Mil02] [Mil04] [HERMES05b] [Wen] was applied.

The basic idea of this unfolding procedure is to simulate the mentioned parasitic effects in a Monte Carlo model with very high accuracy and to keep track how events migrate from one bin to another due to the changes in their kinematics. This makes it possible to describe with statistical methods the behaviour of event samples affected by a change of kinematic quantities due to those well-understood effects. The relative fractions of events which move from any given BORN bin to any given experimentally observed bin can be expressed by a two-dimensional migration matrix, containing in terms of statistics the information where the observed events come from. Inversion of this matrix and multiplication with the real-data asymmetries then delivers the BORN asymmetries in one step. The regained BORN asymmetries depend only on the experimentally measured asymmetries and the Monte Carlo models for background and detector behaviour. Before unfolding the experimentally observed asymmetry data points are correlated because each bin contains events which originally belong into other bins. After unfolding, the data points are uncorrelated, but now their errors are correlated; this requires the use of an error correlation matrix as treating them like independent statistical errors would overestimate the uncertainty.

[1] First-order QED ($\mathcal{O}(\alpha)$) is usally called BORN level.

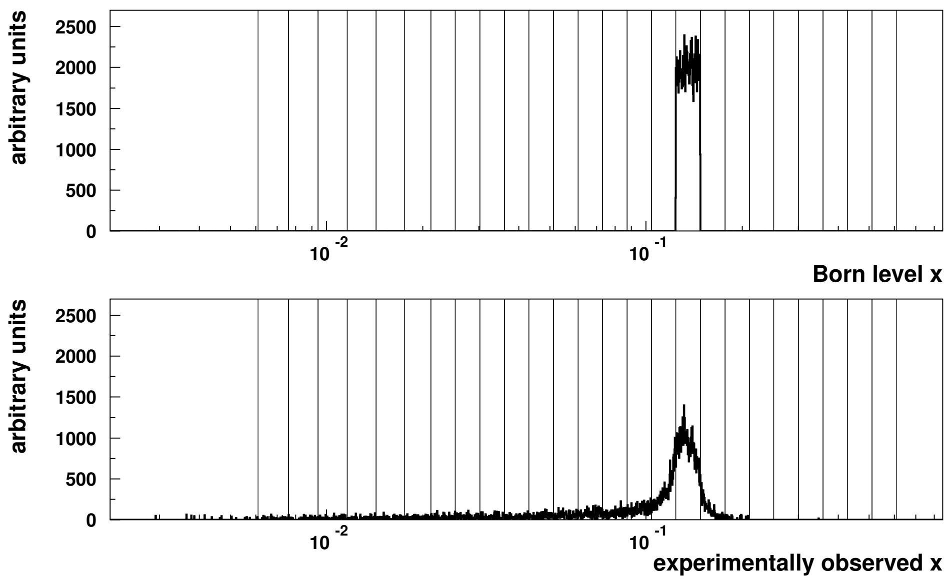

Figure 5.1: The consequences of QED radiative effects and detector smearing on the x distribution is illustrated in these two plots. The upper panel shows the distribution on BORN level as simulated by a Monte Carlo model for one single, arbitrarily selected x bin. The lower panel shows the distribution for the same events after a simulation of QED radiative effects and detector smearing has been applied. A significant part of the events cannot be reconstructed inside the bin to which they would belong according to their kinematics on BORN level. Events which migrate into (mostly adjacent) bins dilute the measured asymmetry there with the asymmetry of their original bin and therefore introduce a systematic correlation between bins. In this simulation a model of the 1997 HERMES detector configuration has been used. The vertical lines indicate bin boundaries.

5.2 Event migration

5.2.1 QED radiative effects

The four second-order QED radiative effects which affect the kinematics of the electromagnetic probe are displayed in Fig. 5.2:

Initial and final state bremsstrahlung modify the four-momentum of the detected DIS electron; the bremsstrahlung photon itself is not detected. In case of final state bremsstrahlung for example the electron kinematics change through the emission of a photon with 4-momentum ξ; afterwards this electron is detected with the four-momentum k'_X whereas its true four-momentum on BORN level would be k'_B. As a consequence also the experimentally observed squared four-momentum transfer Q^2_X and BJORKEN scaling variable x_X will differ from the true values Q^2_B and x_B. (In the following we will always use indices X to denote eXperimentally observed quantities and indices B to denote the true quantities on BORN level.) Due to the

	eXperimentally observed	BORN level
initial state brems- strahlung	$\nu_X = (E - E')$ $x_X = \dfrac{Q^2_X}{2M\nu_X}$ $Q^2_X = 4EE' \sin^2 \dfrac{\theta_X}{2}$	$\nu_B = ((E-\xi) - E')$ $x_B = \dfrac{Q^2_B}{2M\nu_B}$ $Q^2_B = 4(E-\xi)E' \sin^2 \dfrac{\theta_B}{2}$
final state brems- strahlung	$\nu_X = (E - E')$ $x_X = \dfrac{Q^2_X}{2M\nu_X}$ $Q^2_X = 4EE' \sin^2 \dfrac{\theta_X}{2}$	$\nu_B = (E - (E'+\xi))$ $x_B = \dfrac{Q^2_B}{2M\nu_B}$ $Q^2_B = 4E(E'+\xi) \sin^2 \dfrac{\theta_B}{2}$

Table 5.1: Differences between BORN level kinematics and eXperimentally observed kinematics in case of bremsstrahlung; see also Fig. 5.2.

energy loss caused by the emission of a photon the event appears to have a higher energy transfer than it really has ($\nu_X = (E-E') > (E-(E'+\xi) = \nu_B)$ and the relations $Q^2_X < Q^2_B$ and $x_X < x_B$ always hold true in case of bremsstrahlung (see Tab. 5.1).

This may – depending on the magnitude of the change in these variables and on the bin size used in the analysis – cause an event to be reconstructed in an experimental bin which is not identical with the bin on BORN level into which this event would correctly belong. Furthermore it causes a shift of the average kinematic variables $\langle Q^2_X \rangle$ and $\langle x_X \rangle$ *inside* each bin towards lower values compared to the respective BORN level average values. Of course, at the same time each bin is also invaded by events stemming from higher x- and Q^2-bins which tend to shift $\langle Q^2_X \rangle$ and $\langle x_X \rangle$ into the opposite direction. The unfolding formalism allows to correct for all these effects.

After emitting bremsstrahlung photons, elastic[2], quasi-elastic[3] and inelastic[4] scattering events can look like DIS events according to their measured x_X and Q^2_X values. These so-called elastic and inelastic tails contribute to the total measured cross-section. The unfolding procedure includes the simulation of these background contributions which enter the acceptance from outside and allows the subtraction of non-DIS background.

Vacuum polarization via loops of charged lepton pairs reduces the total cross section while the **vertex correction** changes the observed anoma-

[2] $x = 1$
[3] in case of the deuteron and other targets with more than one nucleon
[4] DIS events are by definition a subset of the sample of inelastic scattering events.

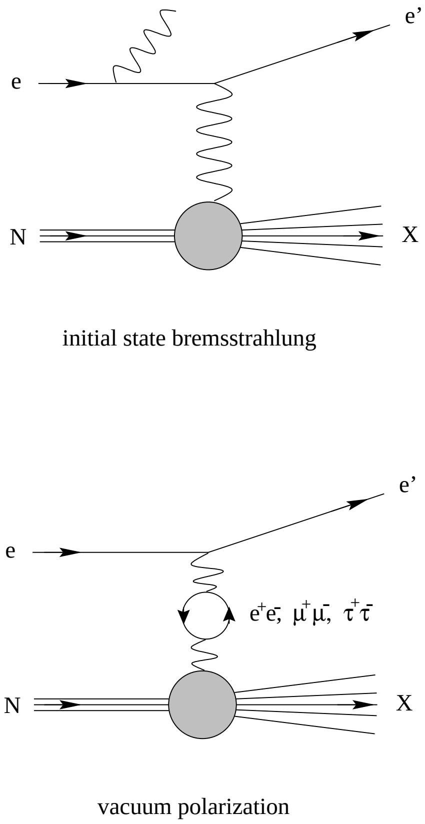

Figure 5.2: Second order QED effects which cause deviations between BORN level kinematics and experimentally observed DIS kinematics.

lous magnetic moment. Both effects contribute to the inelastic part of the cross-section and are also included in the simulation of QED radiative corrections used for the unfolding.

5.2.2 Detector smearing

The scattered electron can encounter multiple scattering with target and detector material after the DIS process. This might change momentum and energy of the reconstructed track to both lower or higher values with respect to the original kinematics. Those detector smearing effects usually cause events to leak into adjacent bins at both lower or higher $\langle x \rangle$ and/or $\langle Q^2 \rangle$. This was simulated by a detailed Monte Carlo model of the HERMES spectrometer which includes all relevant detector materials; the resulting migration of events is also incorporated in the migration matrix.

Detector smearing effects put a physical limit on the resolution of the spectrometer. Obviously choosing bin sizes below the resolving power of the detector doesn't make sense and results only in an unphysical increase of the uncertainties on the measurement. The binning used for the analysis presented here respects this limit and is always above the physical resolution of the spectrometer.

A second detector effect of entirely different nature is caused by misalignment of detector components. Misalignment introduces a systematic offset, e.g. on the measured scattering angle, not a stochastic distribution around the true value like multiple scattering does. Misalignment cannot be eliminated by unfolding and has to be either analytically corrected or – if not feasible – included into the systematic uncertainty (see Section 6.4.4).

5.3 The unfolding formalism

The unfolding formalism requires two sets of inclusive Monte Carlo data as input:

(1) **Fully reconstructed Monte Carlo data, including QED radiative effects and a complete detector simulation.** The events were generated in the angular range $|\theta_x| < 180$ mrad, 35 mrad $< |\theta_y| < 150$ mrad of *observed* kinematics. Starting from the observed kinematics, the BORN level kinematics were calculated 'backwards' simulating radiative effects with RADGEN [ABR98]. The electrons were tracked through a detailed GEANT [BHHL78] model of the HERMES spectrometer and reconstructed with the same HRC [Wan] reconstruction algorithm also used for real data.

(2) **Born Monte Carlo data** generated inside the same acceptance as the above described sample.

The first dataset is the basis for the migration matrices $n_{\uparrow\uparrow}(i,j)$ and $n_{\uparrow\downarrow}(i,j)$ for parallel and antiparallel spin orientation respectively. These matrices contain the count rates which fall both into bin i of eXperimental kinematics and bin j of BORN kinematics. The dimension of these matrices is $n_{\text{bins}} \times (n_{\text{bins}} + 1)$ where n_{bins} is the number of bins used in the analysis; the indices run in the range $i = 1, ..., n_{\text{bins}}$ and $j = 0, ..., n_{\text{bins}}$. Of course the binning for BORN and eXperimental kinematics is identical inside the acceptance (defined by the spectrometer acceptance and the DIS cuts restricting the phase space of the observed electron).

The square sub-matrices of $n_{\uparrow\uparrow}(i,j)$ and $n_{\uparrow\downarrow}(i,j)$ with $1 \leq i,j \leq n_{\text{bins}}$ describe events which remain inside the acceptance: diagonal elements ($i = j$) correspond to events which are reconstructed in the same bin in which they are located on BORN level whereas off-diagonal matrix elements describe events which migrated from BORN bin j to eXperimental bin i.

Apart from this migration between bins inside the acceptance there are two other possible cases: events can – according to their kinematics – either on BORN level or on eXperimental level fall outside of the acceptance[5].

- Events which are reconstructed inside the acceptance in a bin $i = 1, ..., n_{\text{bins}}$ but stem on BORN level from outside of the acceptance are sorted into BORN bin $j = 0$. The columns $n_{\uparrow\uparrow}(i, 0)$ and $n_{\uparrow\downarrow}(i, 0)$ of the migration matrices therefore contain the count rates of background entering the acceptance.

- The opposite case, events which are on BORN level inside the acceptance but get lost due to smearing, cannot be treated in the same way: these events are never seen experimentally. Ignoring this loss of events would lead to a BORN cross section which is too small. To correct for this effect, the second Monte Carlo data set mentioned above, the pure BORN Monte Carlo, is used for normalization.

During the calculation of the migration matrices a correction for an instrumental effect causing a reconstruction inefficiency due to electromagnetic showers is applied. Details can be found in Appendix B.

Figs. 5.3 and 5.4 illustrate the migration matrices $n_{\uparrow\uparrow,\uparrow\downarrow}(i, j)$. An x distribution like the one shown in the lower panel of Fig. 5.1 represents a slice along a given BORN bin j in the matrix displayed in Fig. 5.3. In Fig. 5.4 a migration matrix for the two-dimensional x-Q^2-binning is displayed. As the unfolding procedure is absolutely oblivious to the physical location of the bins relatively to each other and makes no use of the fact if bins are adjacent or not it can be used for any kind of kinematic binning. Therefore a two-dimensional smearing problem can simply be reduced to a one-dimensional problem by renumbering the bins in an arbitrary way. The bin numbering used here follows the scheme listed in Appendix C. As now increasing bin numbers no longer necessarily correspond to increasing x and Q^2 ranges the interpretation of the off-diagonal elements is not as obvious as in the one-dimensional case.

The spin-dependent eXperimental count rates $n^X_{\uparrow\uparrow}(i)$ and $n^X_{\uparrow\downarrow}(i)$ can be calculated from the migration matrices by summing up columns,

$$n^X_{\uparrow\uparrow}(i) = \sum_{j=0}^{n_{\text{bins}}} n_{\uparrow\uparrow}(i, j) \qquad \text{and} \qquad n^X_{\uparrow\downarrow}(i) = \sum_{j=0}^{n_{\text{bins}}} n_{\uparrow\downarrow}(i, j), \tag{5.1}$$

and the spin-independent count rates are given by

$$n^X_u(i) = n^X_{\uparrow\uparrow}(i) + n^X_{\uparrow\downarrow}(i). \tag{5.2}$$

[5]Needless to mention that events which are outside of the acceptance on *both* BORN level *and* eXperimental level are of no interest at all.

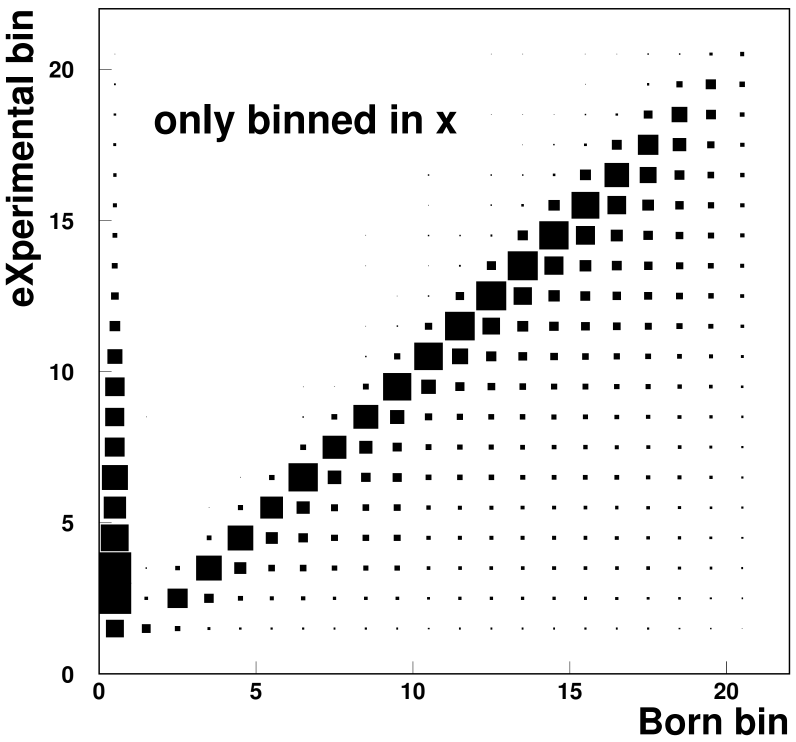

Figure 5.3: Migration matrix $n_{\uparrow\uparrow}$ (the $n_{\uparrow\downarrow}$ matrix looks similar) for a pure x binning. The matrix was extracted from a fully reconstructed Monte Carlo data set simulating both QED radiative and detector effects for inclusive DIS on a proton target.

As already mentioned it is not possible to calculate the BORN count rates in a similar way by summing up the lines of the matrix: the migration matrix contains only events which have been reconstructed inside the acceptance and misses the contribution of events which migrate out of the acceptance due to smearing. Therefore the BORN count rates $n^B_{\uparrow\uparrow}(j)$ and $n^B_{\uparrow\downarrow}(j)$ are extracted from the BORN Monte Carlo dataset. Based on these count rates, cross section normalized migration matrices

$$\begin{aligned} S_{\uparrow\uparrow}(i,j) &= \frac{\partial\sigma^X_{\uparrow\uparrow}(i)}{\partial\sigma^B_{\uparrow\uparrow}(j)} = \frac{n_{\uparrow\uparrow}(i,j)}{n^B_{\uparrow\uparrow}(j)} \qquad i,j = 1,...,n_{\text{bins}} \\ S_{\uparrow\downarrow}(i,j) &= \frac{\partial\sigma^X_{\uparrow\downarrow}(i)}{\partial\sigma^B_{\uparrow\downarrow}(j)} = \frac{n_{\uparrow\downarrow}(i,j)}{n^B_{\uparrow\downarrow}(j)} \end{aligned} \tag{5.3}$$

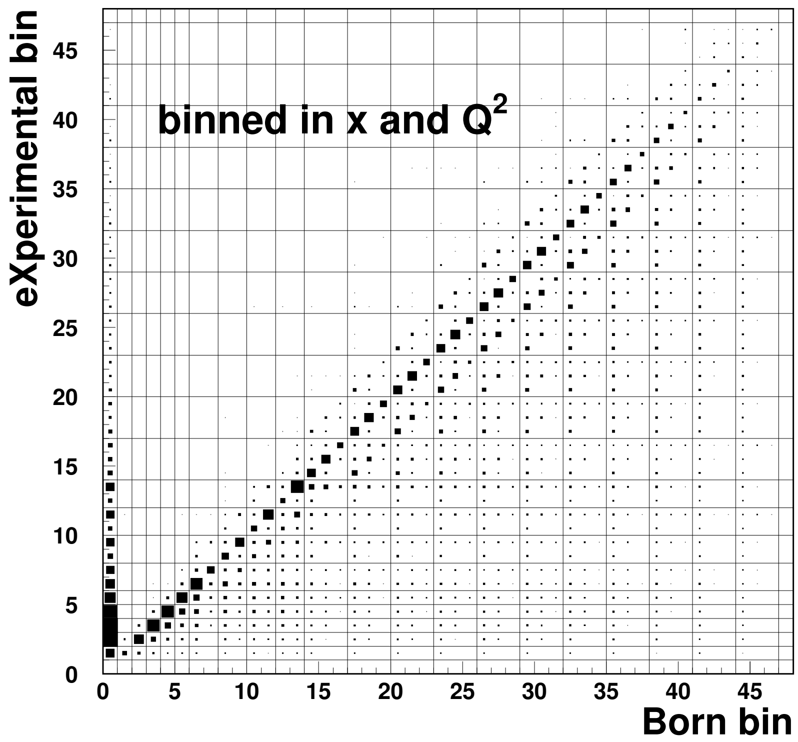

Figure 5.4: Migration matrix $n_{\uparrow\uparrow}$ (the $n_{\uparrow\downarrow}$ matrix looks similar) for the combined x and Q^2 binning used in this analysis. The lines indicate x bins which are subdivided in Q^2. The matrix was extracted from a fully reconstructed Monte Carlo data set simulating both QED radiative and detector effects for inclusive DIS on a proton target.

are calculated. Please note that both the numerator and the denominator of the matrix elements scale with the relative number of BORN events generated in each bin which causes any dependence on the Monte Carlo BORN model to cancel. This is essential as the aim is to calculate BORN asymmetries from a measurement and these extracted BORN asymmetries must not depend on the model used in the process of their extraction.

Nevertheless a certain dependence on the used BORN model enters through the back door in terms of spin-dependent background rates

$$n_p(i,0) = n_{\uparrow\downarrow}(i,0) - n_{\uparrow\uparrow}(i,0) \tag{5.4}$$

which smear into the acceptance from outside.

The relation between the Monte Carlo yields for eXperimental kinematics and the Monte Carlo yields for BORN level kinematics is

$$n^X_{\uparrow\uparrow}(i) = \sum_{j=0}^{n_{\rm bins}} S_{\uparrow\uparrow}(i,j)\, n^B_{\uparrow\uparrow}(j) \qquad i = 1, ..., n_{\rm bins} \tag{5.5}$$

$$n^X_{\uparrow\downarrow}(i) = \sum_{j=0}^{n_{\rm bins}} S_{\uparrow\downarrow}(i,j)\, n^B_{\uparrow\downarrow}(j) \tag{5.6}$$

which leads to the following expression for the spin dependent Monte Carlo asymmetry $A_{||}^{X_{\rm MC}}$:

$$\begin{aligned} A_{||}^{X_{\rm MC}}(i) &= \frac{n^X_{\uparrow\downarrow}(i) - n^X_{\uparrow\uparrow}(i)}{n^X_{\uparrow\downarrow}(i) + n^X_{\uparrow\uparrow}(i)} = \frac{n^X_{\uparrow\downarrow}(i) - n^X_{\uparrow\uparrow}(i)}{n^X_u(i)} \\ &= \frac{1}{n^X_u(i)} \sum_{j=0}^{n_{\rm bins}} [S_{\uparrow\downarrow}(i,j)\, n^B_{\uparrow\downarrow}(j) - S_{\uparrow\uparrow}(i,j)\, n^B_{\uparrow\uparrow}(j)]. \end{aligned} \tag{5.7}$$

The background term (Eq. (5.4)) can be separated from the sum and moved to the other side of the equation:

$$\begin{aligned} &\sum_{j=1}^{n_{\rm bins}} [S_{\uparrow\downarrow}(i,j)\, n^B_{\uparrow\downarrow}(j) - S_{\uparrow\uparrow}(i,j)\, n^B_{\uparrow\uparrow}(j)] = \\ &= A_{||}^{X_{\rm MC}}(i)\, n^X_u(i) - [S_{\uparrow\downarrow}(i,0)\, n^B_{\uparrow\downarrow}(0) - S_{\uparrow\uparrow}(i,0)\, n^B_{\uparrow\uparrow}(0)] \\ &= A_{||}^{X_{\rm MC}}(i)\, n^X_u(i) - n_p(i,0). \end{aligned} \tag{5.8}$$

The relation in Eq. 5.8 is also generally applicable to a *measured* asymmetry $A_{||}$ like the asymmetries $A^p_{||}$ and $A^d_{||}$ extracted in chapter 4. This gives access to the real world BORN rates $B_{\uparrow\uparrow}$ and $B_{\uparrow\downarrow}$ (provided the spin-independent BORN rates $n^B_u(j)$ – which are known from other experiments – are correctly reproduced by the Monte Carlo generating the input data sets, $n^B_u(j) = n^B_{\uparrow\downarrow}(j) + n^B_{\uparrow\uparrow}(j) \stackrel{!}{=} B_{\uparrow\downarrow} + B_{\uparrow\uparrow} \equiv B_u(j)$):

$$\sum_{j=1}^{n_{\rm bins}} [S_{\uparrow\downarrow}(i,j)\, B_{\uparrow\downarrow}(j) - S_{\uparrow\uparrow}(i,j)\, B_{\uparrow\uparrow}(j)] = A_{||}(i)\, n^X_u(i) - n_p(i,0). \tag{5.9}$$

We now may eliminate $B_{\uparrow\uparrow}$ in favour of $B_{\uparrow\downarrow}$ and $B_u(j)$,

$$\begin{aligned} &\sum_{j=1}^{n_{\rm bins}} [S_{\uparrow\downarrow}(i,j) + S_{\uparrow\uparrow}(i,j)]\, B_{\uparrow\downarrow}(j)] = \\ &= A_{||}(i)\, n^X_u(i) - n_p(i,0) + \sum_{j=1}^{n_{\rm bins}} S_{\uparrow\uparrow}(i,j)\, B_u(j) \\ &= A_{||}(i)\, n^X_u(i) - n_p(i,0) + \sum_{j=1}^{n_{\rm bins}} S_{\uparrow\uparrow}(i,j)\, n^B_u(j). \end{aligned} \tag{5.10}$$

We define $S(i,j) \equiv S_{\uparrow\downarrow}(i,j) + S_{\uparrow\uparrow}(i,j)$ and the square submatrix of $S(i,j)$ with $i,j = 1,...,n_{\mathrm{bins}}$ (without the column $j = 0$) as S'. If the migration is sufficiently small and the statistics of the Monte Carlo sample used to build up the matrix is high enough that statistical fluctuations on the matrix elements are negligible the matrix will be well defined and can be inverted to solve Eq. (5.10). Together with the substitution

$$A_{||}^{B}(j) = \frac{B_{\uparrow\downarrow}(j) - B_{\uparrow\uparrow}(j)}{B_{\uparrow\downarrow}(j) + B_{\uparrow\uparrow}(j)} = \frac{2B_{\uparrow\downarrow}(j) - B_u(j)}{B_u(j)} \tag{5.11}$$

this leads to the final expression for the unfolded asymmetry,

$$\begin{aligned} A_{||}^{B}(j) = -1 + \frac{2}{n_u^B(j)} \sum_{i=1}^{n_{\mathrm{bins}}} [S']^{-1}(j,i) \times \\ \left[A_{||}(i)\, n_u^X(i) \; - n_p(i,0) \sum_{k=1}^{n_{\mathrm{bins}}} S_{\uparrow\uparrow}(i,k)\, n_u^B(k) \right], \end{aligned} \tag{5.12}$$

for $j = 1,...,n_{\mathrm{bins}}$.

The covariance matrix C which follows from Eq. (5.12) describes the dependence between any given two points of the unfolded Born asymmetry $A_{||}^{B}$:

$$C(A_{||}^{B}(j), A_{||}^{B}(k)) = \sum_{i=1}^{n_{\mathrm{bins}}} D(j,i) D(k,i) \sigma^2(A_{||}(i)) \tag{5.13}$$

with the radiative dilution matrix $D(j,i)$ being defined as

$$D(j,i) \equiv \frac{\partial A_{||}^{B}(j)}{\partial A_{||}(i)} = \frac{2[S']^{-1}(j,i)\, n_u^X(i)}{n_u^B(j)} \tag{5.14}$$

and $\sigma(A_{||}(i))$ being the statistical error on the measured asymmetry $A_{||}(i)$.

As mentioned before event migration causes a shift of the mean kinematic values $\langle x \rangle$, $\langle y \rangle$, $\langle Q^2 \rangle$, etc. inside each bin. To correct for this, the assumption is made that the ratio between kinematical quantities on Born and eXperimental level is similar both in Monte Carlo and in reality (a presumption on which the whole unfolding method is based):

$$\frac{\langle x_B^{\mathrm{MC}} \rangle}{\langle x_X^{\mathrm{MC}} \rangle} = \frac{\langle x_B^{\mathrm{real\ data}} \rangle}{\langle x_X^{\mathrm{real\ data}} \rangle}, \quad \frac{\langle y_B^{\mathrm{MC}} \rangle}{\langle y_X^{\mathrm{MC}} \rangle} = \frac{\langle y_B^{\mathrm{real\ data}} \rangle}{\langle y_X^{\mathrm{real\ data}} \rangle}, \quad \frac{\langle Q_B^{2\,\mathrm{MC}} \rangle}{\langle Q_X^{2\,\mathrm{MC}} \rangle} = \frac{\langle Q_B^{2\,\mathrm{real\ data}} \rangle}{\langle Q_X^{2\,\mathrm{real\ data}} \rangle}, \quad \text{etc.} \tag{5.15}$$

5.4 Unfolded asymmetries $A_{||}^{p}$ and $A_{||}^{d}$

The unfolded cross section asymmetries $A_{||}^{p}$ and $A_{||}^{d}$ of the proton and the deuteron are shown in Fig. 5.5 and Fig. 5.6. Comparing these asymmetries with the asymmetries before unfolding as shown in Figs. 4.6 and 4.7 two effects of the unfolding procedure are obvious: (i) The fluctuations of the data points increased and the asymmetry appears to be "less smooth" due to the de-coupling of the individual asymmetry data points. (ii) The size of the error bars also increased.

It is important to note that a direct comparison of the size of the error bars before and after unfolding is meaningless. The error bars before unfolding as shown in Fig. 4.6 and Fig. 4.7 are purely statistical, which is no longer true for the error bars displayed in Figs. 5.5 and 5.6. The error bars of the unfolded asymmetry as shown in Figs. 5.5 and 5.6 correspond only to the diagonal elements of the associated covariance matrix given in Eq. (5.13). The off-diagonal elements of the covariance matrix contain the information how the error bars are correlated between each other. The correlation is especially strong between neighbouring data points as the dominant fraction of events which migrate out of their BORN bin end up in the adjacent bin (compare Fig. 5.1).

Although a Q^2 dependence of the structure function $g_1(x, Q^2)$ in form of scaling violations is expected like in the case of the unpolarized structure functions F_1 and F_2 it is certainly impossible to measure this Q^2 dependence within the limited Q^2 range covered by HERMES given the statistical and systematic accuracy of the data. The Q^2 binning in this analysis was merely chosen for technical reasons as explained in Section 4.5 and is not meant to reveal scaling violations by comparing the different Q^2 ranges measured at the same value of x.

The differences in the measured asymmetries visible in Fig. 5.5 and Fig. 5.6 at the same value of x but for different values of Q^2 comes from the y dependence of the depolarization factor (2.16): low values of Q^2 are associated with low values of y and thus with low polarization of the virtual photon. Comparing the size of the error bars in these asymmetries with the size of the error bars before unfolding as shown in Fig. 4.6 and Fig. 4.7 it is obvious that in the uncertainty inflation is much stronger in the low Q^2 (low y) region than at higher values of Q^2. The reason for this is more pronounced smearing due to the degrading spectrometer resolution in this kinematic region as explained in Section 4.5 (see Fig. 4.5). Fortunately the impact of this problematic region on the measurement is almost negligible because of the low virtual photon polarization. The increase of errors at very low values of x is driven by the subtraction of elastic (and in case of the deuteron quasi-elastic) background which entered the acceptance from outside.

Therefore the next step in the extraction of the structure function g_1 is the calculation of the structure function ratio g_1/F_1 in 46 $x - Q^2$ bins which are then averaged over Q^2, thus reducing the two-dimensional binning to a one-dimensional x binning. The extraction of g_1 will be the subject of the next chapter.

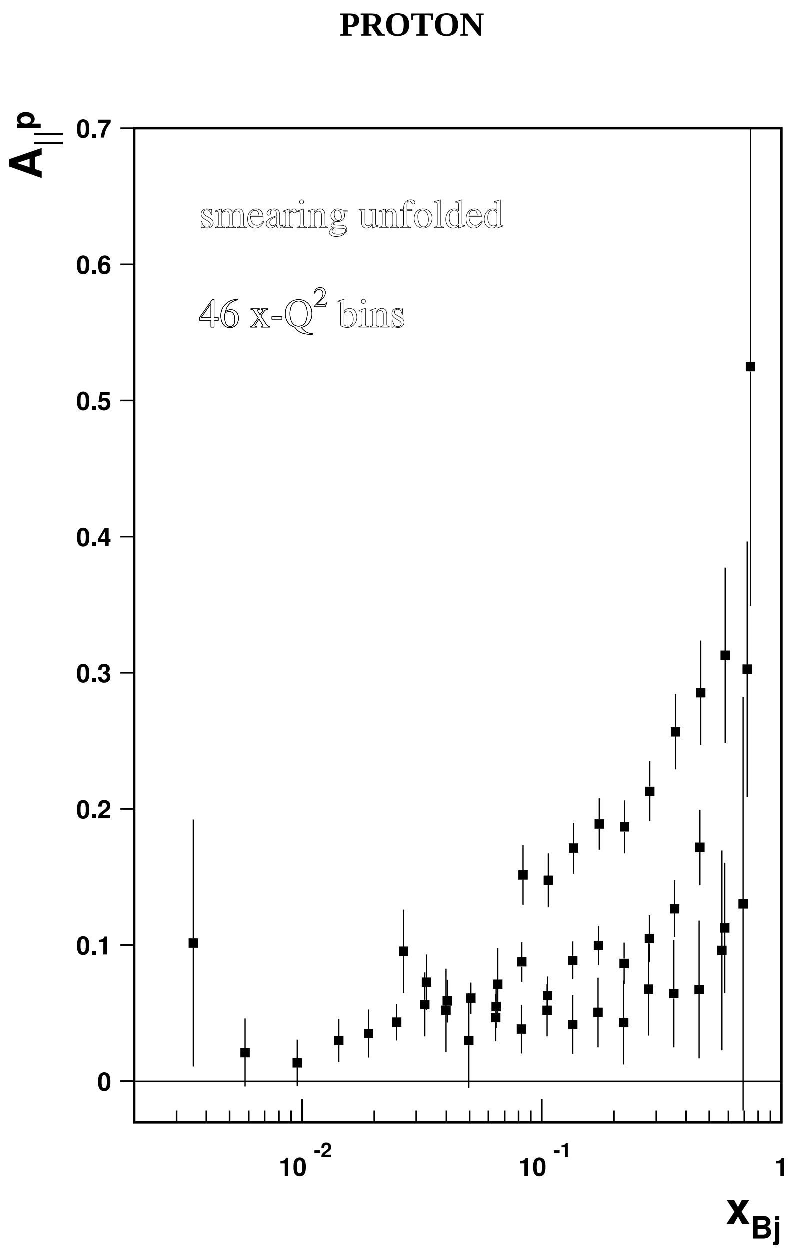

Figure 5.5: Unfolded (=BORN level) cross-section asymmetry $A_{\|}^{p}$. The two and three different branches of the asymmetry belong to x bins which are subdivided in two or three Q^2 bins (please compare Fig. 4.4). The lowest branch belongs to the bins in the low Q^2 region and the higher branches belongs to those which cover higher ranges in Q^2.

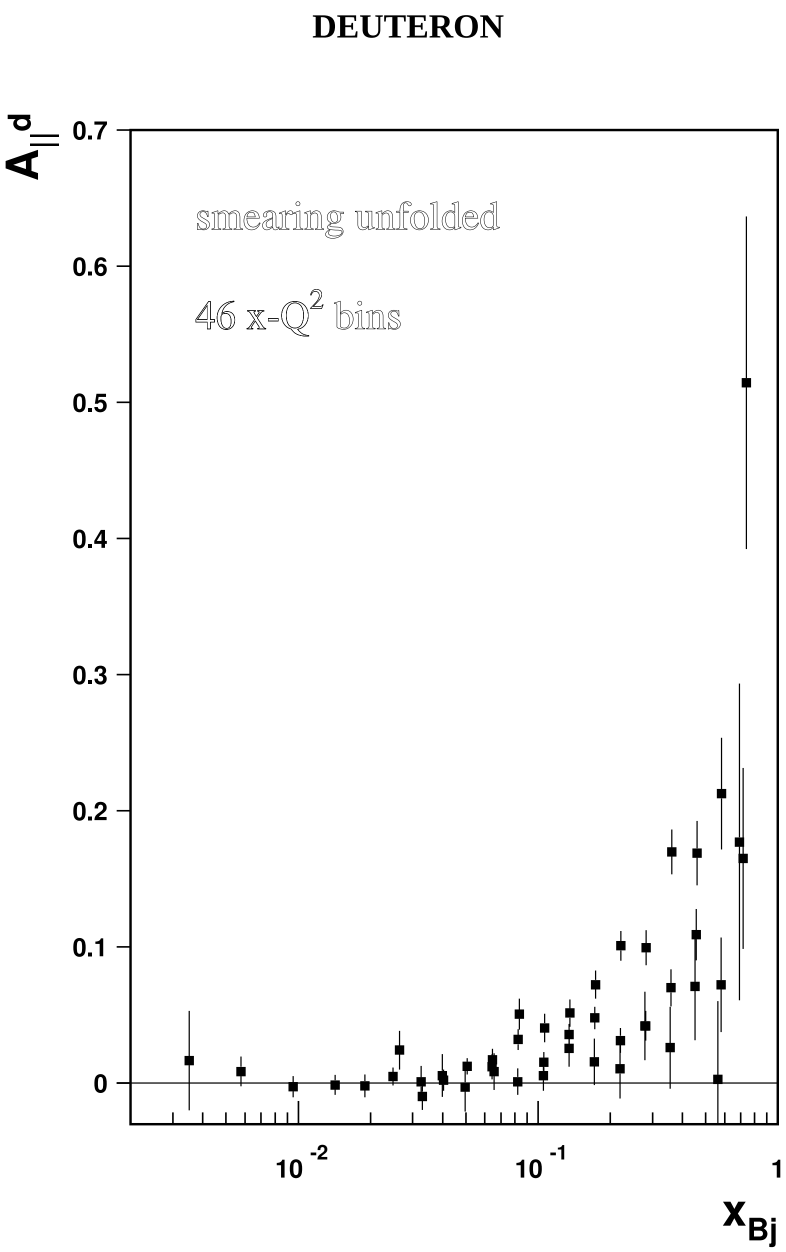

Figure 5.6: Unfolded (=BORN level) cross-section asymmetry $A_{\parallel}^{d}$. The two and three different branches of the asymmetry belong to x bins which are subdivided in two or three Q^2 bins (please compare Fig. 4.4). The lowest branch belongs to the bins in the low Q^2 region and the higher branches belongs to those which cover higher ranges in Q^2.

Chapter 6

Extraction of the Spin Structure Function g_1

6.1 From the unfolded $A_{\|}$ to g_1 for proton and deuteron

As shown in Section 2.2 the cross section asymmetry $A_{||}$ (2.11) which was unfolded for smearing effects in the previous chapter can be directly related to the structure function ratio g_1/F_1 and to the spin-dependent structure function g_1:

$$\frac{g_1}{F_1} = \frac{1}{1+\gamma^2}\left[\frac{A_{||}^B}{D} + (\eta - \zeta)A_2\right], \tag{6.1}$$

$$g_1 = \frac{F_1}{1+\gamma^2}\left[\frac{A_{||}^B}{D} + (\eta - \zeta)A_2\right]. \tag{6.2}$$

For the extraction of g_1 parametrizations of A_2 and F_1 have been used[1]. The A_2 parametrizations were obtained by fits to available proton and deuteron data on A_2 (see Fig. 6.1) [Muon96] [Muon94] [E15503] [E14396] [E15599b] [HER05]:

$$A_2^p = 0.53 \cdot M_p \frac{x}{\sqrt{Q^2}} \quad \text{and} \quad A_2^d = 0.22 \cdot M_p \frac{x}{\sqrt{Q^2}}. \tag{6.3}$$

The used parametrizations of the spin-independent structure function F_1 are based on the F_2 parametrization by Abramowicz, Levin, Levy and Maor (ALLM) [AL97], the ratio F_2^n/F_2^p measured by NMC [Muon92] (in case of the deuteron), and the ratio $R = \sigma_L/\sigma_T$ from [WRB$^+$90] ("R1990") using the relation [FJ01]

$$F_1(x, Q^2) = \frac{1+\gamma^2}{2x(1+R(x,Q^2))}\, F_2(x, Q^2). \tag{6.4}$$

[1] To be consistent, the same parametrizations have also been used for the production of the Monte Carlo dataset used for the unfolding procedure.

From Eq. (6.1) follows that the covariance matrix of the unfolded BORN asymmetry $A_{||}^B$ has to be weighted with the factors $1/(1+\gamma^2)$ and $1/D$ to obtain the covariance matrix for g_1/F_1. The matrix element $cov(g_1/F_1)_{i,k}$ describing the covariance between bin i and bin k is given by

$$cov(\frac{g_1}{F_1})_{i,k} = \frac{1}{(1+\gamma_i^2)D_i}\,\frac{1}{(1+\gamma_k^2)D_k}\,cov(A_{||}^B)_{i,k}. \tag{6.5}$$

In this expression γ_i^2 (γ_k^2) and D_i (D_k) are calculated at the average x and Q^2 values of bin i (k).

After calculating g_1/F_1 according to Eq. (6.1) in the two-dimensional x–Q^2 binning, the g_1/F_1 values of those x bins which are sub-divided in Q^2 have been averaged over Q^2 using the method described in Appendix A.

The resulting structure function ratios g_1/F_1 for proton and deuteron in 20 x bins are shown in Fig. 6.2. In this plot the error bars correspond only to the *diagonal* elements of the covariance matrix Eq. (6.5); the correlation between the errors of the individual data points is given by the correlation matrices which are illustrated in Fig. 6.3 and Fig. 6.4 (see also Appendix A.3). The correlation matrices show that there is a strong negative correlation between adjacent datapoints as expected from a distribution like the one shown in Fig. 5.1, but the strength of the correlation falls off rapidly for bins which are not direct neighbours.

6.1.1 Proton asymmetry g_1/F_1

With increasing x the proton asymmetry g_1/F_1 rises continuously to a value of 0.96 at the highest measured x point ($x = 0.72$) as can be seen in Fig. 6.2. For large values of x the asymmetry is sensitive to the valence quark distributions and it seems sensible to expect that the quark carrying most of the nucleon's momentum is also carrying most of its spin and therefore $A_1(\approx g_1/F_1) \rightarrow 1$ for $x \rightarrow 1$. In case of the proton the asymmetry at large x is dominated by scattering on u quarks due to the valence quark configuration uud and the larger absolute value of the electric charge of the u quark ($|\frac{2}{3}e|$) compared to the d quark ($|-\frac{1}{3}e|$). Hence a large positive proton asymmetry for $x \rightarrow 1$ can be interpreted as evidence for a significant positive polarization of the u valence quarks with respect to the proton's spin.

At small values of x the proton asymmetry decreases to very small values which become compatible with zero within the uncertainties for $x < 10^{-2}$ but with a clear tendency towards positive values. For $x \rightarrow 0$ the asymmetry is sensitive to the sea quark distributions and the size of the asymmetry may be interpreted as indication that the sea quarks contribute only little to the spin of the proton.

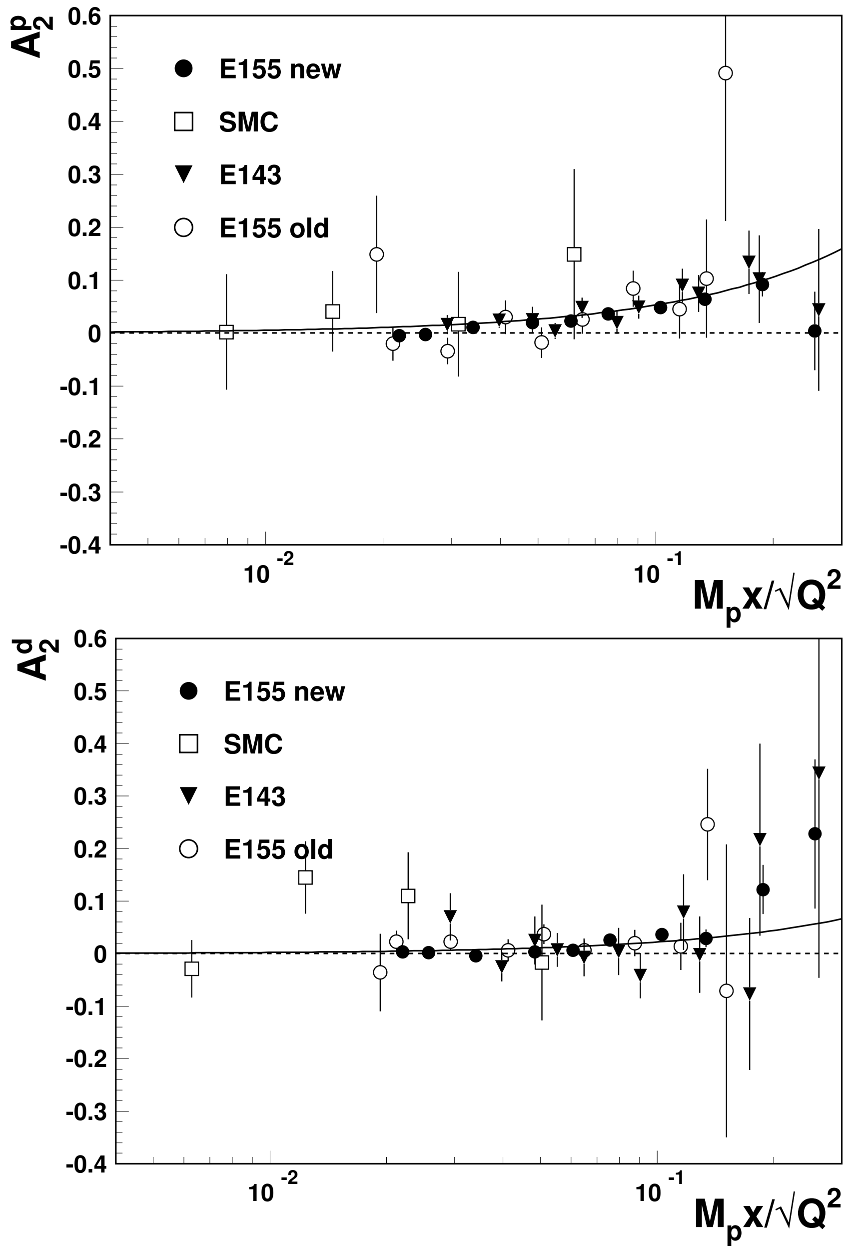

Figure 6.1: Fits to the virtual photon asymmetry A_2 of proton and deuteron used in this analysis. The fits give a χ^2/dof of 1.44 for A_2^p and 1.06 for A_2^d [HER05]. The data points are from [Muon96] [Muon94] [E15503] [E14396] [E15599b].

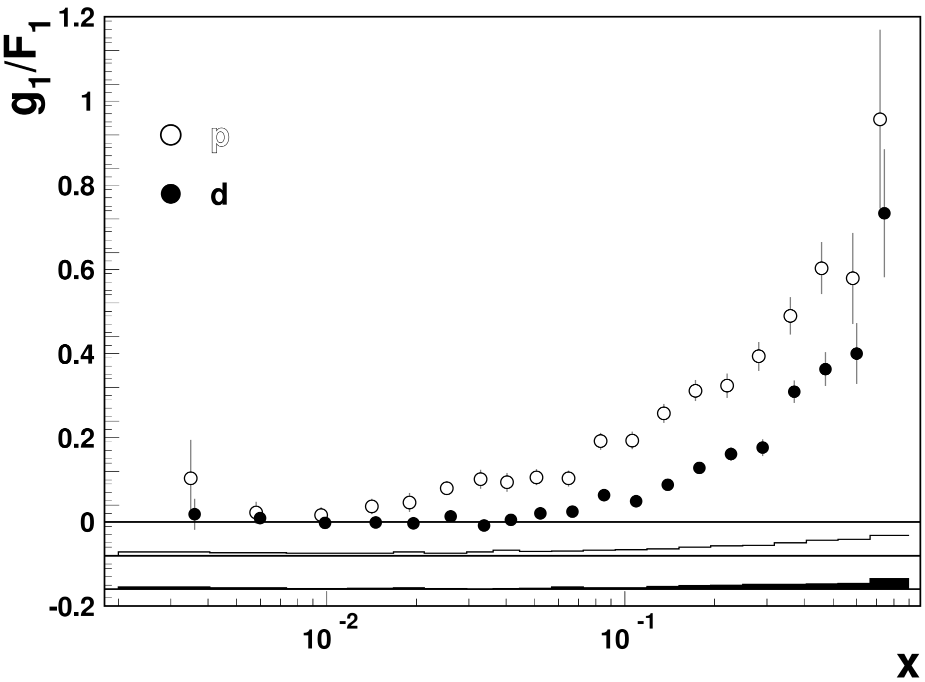

Figure 6.2: Structure function ratios g_1^p/F_1^p and g_1^d/F_1^d [CDNE+04a] for proton and deuteron. The error bars correspond to the diagonal elements of the covariance matrices; the correlation between the error bars is shown in Fig. 6.3 for the proton points and Fig. 6.4 for the deuteron points. The error bands indicate the systematic uncertainties of the two measurements.

6.1.2 Deuteron asymmetry g_1/F_1

The asymmetry g_1/F_1 measured on the deuteron is a mixture of the characteristics of it's constituents, proton and neutron. Like the proton asymmetry also the deuteron asymmetry rises for $x \to 1$, but to much lesser extent (see Fig. 6.2). The deuteron asymmetry has always lower values than the proton asymmetry which is an indication that the neutron asymmetry must have considerably smaller values than the proton asymmetry.

In the region $x < 4 \times 10^{-2}$ the deuteron asymmetry is compatible with zero, perhaps even with a slight tendency towards negative values. This leads to the conclusion that in this x range the spin-dependent contributions $\Delta u(x)$ and $\Delta d(x)$ are of similar absolute value but of opposite sign and therefore largely compensate each other.

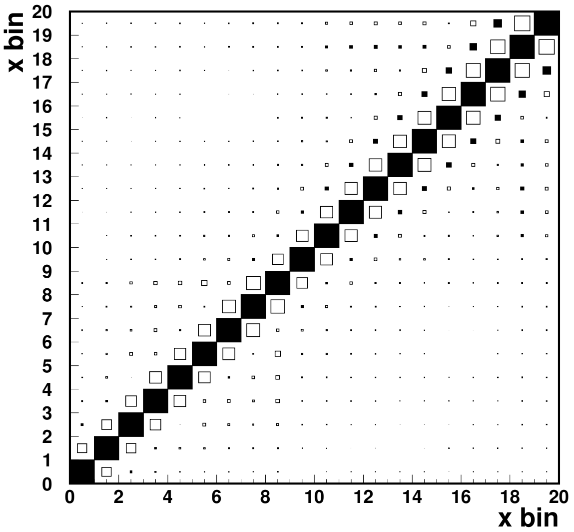

Figure 6.3: Error correlation matrix for g_1^p/F_1^p. Filled squares correspond to positive values while open squares correspond to negative values of the correlation; the diagonal element trivially equal a correlation of +1 as every error bar is 100% correlated with itself.

6.1.3 Spin structure functions xg_1 of proton and deuteron

The spin-dependent structure functions xg_1 of the proton and the deuteron are shown in Fig. 6.5. It can be seen that over the entire measured x range xg_1^p is larger than xg_1^d. Both xg_1^p and xg_1^d reach their maximum around $x \approx 4 \times 10^{-1}$, the magnitude of xg_1^p being about twice as large as the magnitude of xg_1^d.

xg_1^d becomes compatible with zero for $x < 4 \times 10^{-2}$ where xg_1^p still is clearly positive. xg_1^p becomes compatible with zero within its uncertainty for $x < 10^{-2}$ but with a clear tendency to positive values.

Based on these measurements we can calculate the spin-dependent structure function xg_1^n of the neutron as discussed in Section 6.2.2.

6.2 Extraction of the neutron spin structure function g_1^n

HERMES has performed two measurements of the neutron spin structure function g_1^n: In 1995, during the first year of data taking, g_1^n was measured with a polarized ^{3}He target, the results are published in [HERMES97]. A second, independent determination of g_1^n from the 1996–2000 measurements

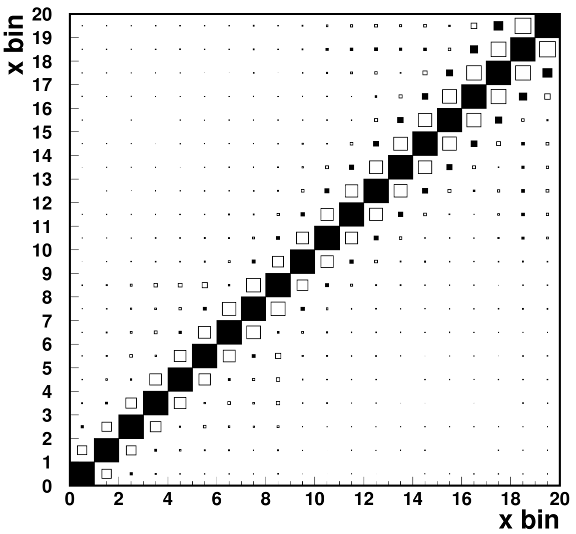

Figure 6.4: Error correlation matrix for g_1^d/F_1^d. Filled squares correspond to positive values while open squares correspond to negative values of the correlation; the diagonal element trivially equal a correlation of +1 as every error bar is 100% correlated with itself.

on hydrogen and deuterium targets is presented in this thesis.

6.2.1 g_1^n from ^{3}He

^{3}He can be considered in good approximation as a neutron target: the wave function of the ^{3}He nucleus is dominated by the configuration with the protons paired to zero spin. Therefore, most of the asymmetry measured on ^{3}He is due to the neutron [FGP$^+$90]. To obtain the neutron structure function g_1^n with a ^{3}He target corrections for nuclear effects are required. Binding effects and FERMI motion are negligible for the g_1^n extraction from ^{3}He and nuclear effects can be treated as a dilution due to scattering off the two largely unpolarized protons [CdASPS93]. A correction for the non-zero polarization of the protons (-0.028 ± 0.004) and the neutron polarization (0.86 ± 0.02) has been used in the analysis described in [HERMES97].

6.2.2 g_1^n from hydrogen and deuterium

Also from the structure functions g_1^d and g_1^p of deuteron and proton the neutron's spin structure function g_1^n can be extracted. Basically, the polarized proton inside the deuteron has to be subtracted, but in addition another correction has to be taken into account: the D-state admixture in the $p-n$

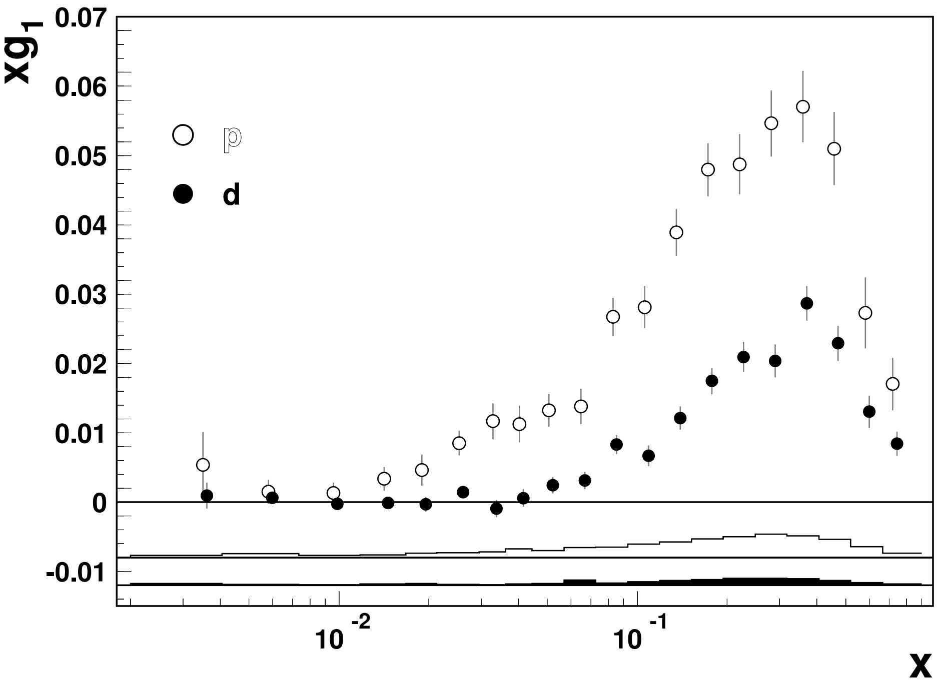

Figure 6.5: Spin-dependent structure functions xg_1 for proton and deuteron. The error bands represent total systematic uncertainties [CDNE+04a].

wave function reduces the deuteron spin structure function due to the opposite alignment of the $p-n$ spin system in this orbital state [FJ01]. The spin structure functions of neutron, deuteron and proton are related like

$$g_1^n = \frac{2\,g_1^d}{1-\frac{3}{2}\omega_D} - g_1^p, \tag{6.6}$$

where the constant factor $(1-\frac{3}{2}\omega_D)$ represents a dilution due to the above mentioned D-state admixture in the $p-n$ wave function and ω_D is the probability of the deuteron to be in the D orbital state. Here, a value of $\omega_D = 0.05 \pm 0.01$ was used which covers most of the published values [L+80] [L+81] [LSS98] [BG79] [ZT80] [MHE87] [Boe05].

The extracted spin structure function of the neutron is shown in the lower panel of Fig. 6.6 in comparison to the ^{3}He measurement described in Section 6.2.1. The agreement between these two independent measurements is excellent. The results from hydrogen and deuterium cover a much larger x range than the ^{3}He data.

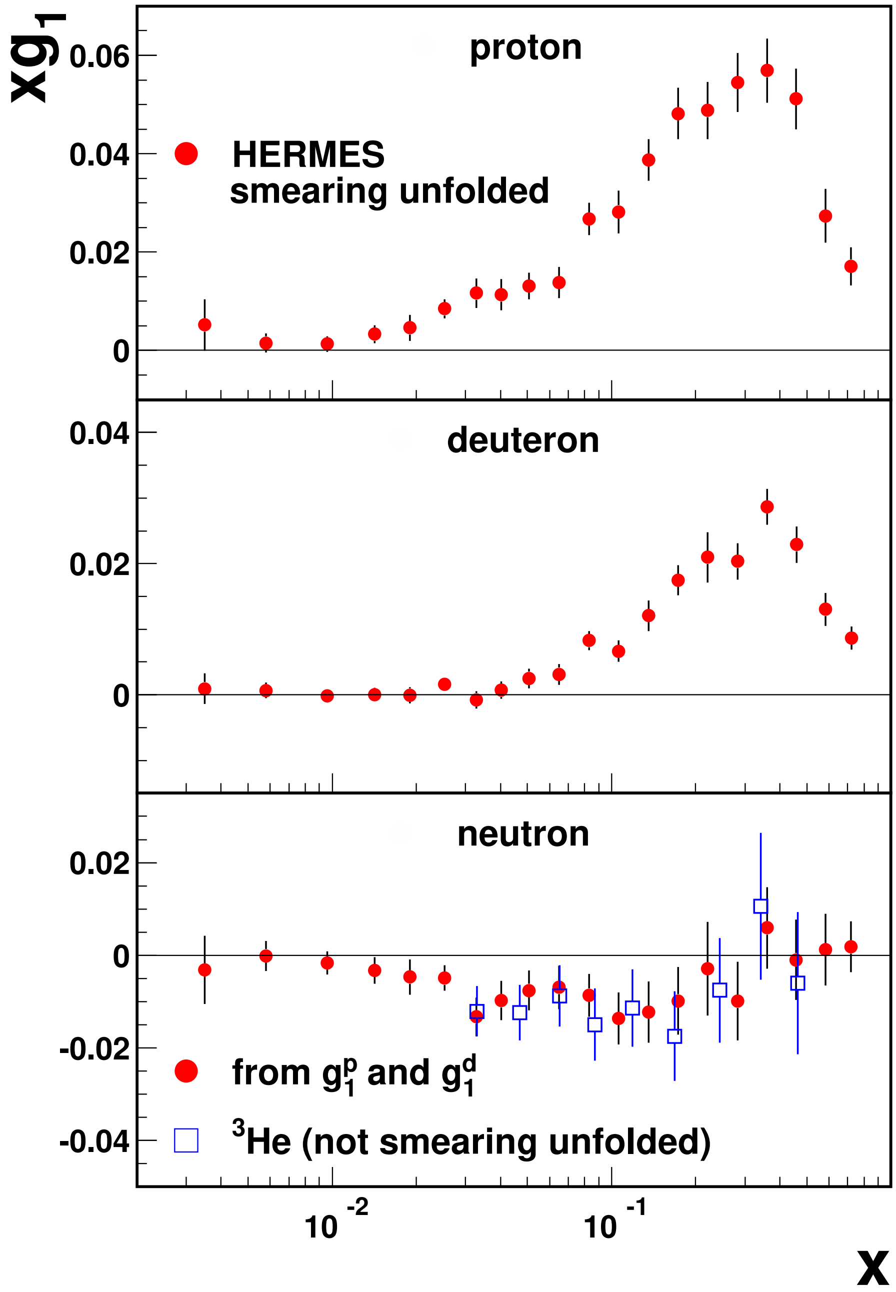

Figure 6.6: Spin structure functions xg_1 of the proton, deuteron and neutron [CDNE+04a]. The proton spin structure function is found to be positive and of large magnitude while the neutron spin structure function is of small magnitude and negative. The neutron spin structure function as extracted from the proton and deuteron measurements presented in this analysis (see Eq. (6.6)) is shown in comparison to a previous HERMES measurement on ^{3}He [HERMES97]. Note that the result obtained on ^{3}He is not unfolded for detector smearing and QED radiative effects. The error bars represent total uncertainties.

xg_1^n is of small magnitude and negative over almost the entire measured x range. For $x > 0.3$, xg_1^n becomes compatible with zero or even slightly positive. In the region $10^{-2} < x < 4 \times 10^{-2}$ xg_1^n is negative due to the fact that xg_1^d is compatible with zero while xg_1^p is definitely positive.

Although $g_1(x)$ — being defined in the QPM as the *sum* over spin-dependent quark distributions — is not flavour sensitive, certain conclusions about the distributions Δu and Δd in the valence quark region can be drawn by comparing the spin structure functions of proton and neutron. According to Eq. (2.30) $g_1^p(x)$ and $g_1^n(x)$ can be written as:

$$g_1^p(x) = \frac{1}{2}\left[\frac{4}{9}(\Delta u^p + \Delta\overline{u}^p) + \frac{1}{9}(\Delta d^p + \Delta\overline{d}^p) + ...\right] \tag{6.7}$$

$$g_1^n(x) = \frac{1}{2}\left[\frac{4}{9}(\Delta u^n + \Delta\overline{u}^n) + \frac{1}{9}(\Delta d^n + \Delta\overline{d}^n) + ...\right]. \tag{6.8}$$

Because of isospin symmetry we know that $\Delta u^p = \Delta d^n$ and $\Delta d^p = \Delta u^n$. In Section 6.1.1 we concluded from the measurement on the proton that Δu^p is large and positive, hence the same must be valid for Δd^n, but now entering the cross-section with a four times smaller charge weight in case of the neutron. Therefore we can conclude from $g_1^n(x)$ that Δu^n (=Δd^p) must be of significantly smaller magnitude and negative in the valence quark region.

6.3 First moments of g_1^p and g_1^d

The first moments of the structure functions g_1^p and g_1^d within the measured range have been calculated. Only data points with a cut of $Q^2 > 1$ GeV^2 have been included into the integration, restricting the integral to the range

$$\tilde{\Gamma}_1 = \int_{0.02124}^{0.9} g_1(x)\, \mathrm{d}x. \tag{6.9}$$

As the acceptance of the spectrometer introduces a kinematic correlation between x and Q^2 (see Fig. 6.7) it is necessary to evolve all g_1 values from the measured $\langle Q^2\rangle$ to a common value of Q^2 before evaluating the integral. The structure function ratio g_1/F_1 seems to be independent of Q^2 as can be seen from Fig. 7.1 (especially for the very precise proton data in the upper panel): Although $\langle Q^2\rangle$ of the various experiments covers about one order of magnitude, the measured g_1/F_1 values are compatible within their accuracy. As both F_1 and g_1 are functions of Q^2 this leads to the conclusion that they must have a very similar Q^2 dependence so that it cancels in the ratio. Using this assumption the measured g_1 points can be evolved to a common value of Q_0^2 like

$$g_1(\langle x_i\rangle, Q_0^2) = \frac{g_1}{F_1}(\langle x_i\rangle, \langle Q_i^2\rangle) \cdot F_1(\langle x_i\rangle, Q_0^2), \tag{6.10}$$

where $\langle x_i \rangle$ and $\langle Q_i^2 \rangle$ denote the average x and Q^2 values in bin i and F_1 can be parametrized as discussed in Section 6.1.

Using the hypothesis that the structure function ratio g_1/F_1 can be approximated by a constant over the bin width one could evaluate (6.9) as the sum over the rectangles given by the value of $g_1(\langle x_i \rangle, Q_0^2)$ in bin i times the bin width,

$$\tilde{\Gamma}_1 = \sum_{i=1}^{n} \left(\frac{g_1}{F_1}(\langle x_i \rangle, \langle Q_i^2 \rangle) \cdot F_1(\langle x_i \rangle, Q_0^2) \cdot (x_{i+1} - x_i) \right), \tag{6.11}$$

where x_i, x_{i+1} denote the boundaries of bin i. However, the drawback of this integration method is that it doesn't take into account the fall off of the cross section for $x \to 1$. Expecially the upper boundary of the highest x bin is hard to justify as the population of events in this bin rapidly decreases with increasing x and one risks large contributions to the integral from an x range where in fact no events are left.

Therefore another integration method was chosen to take into account the cross section fall off: instead of $F_1(\langle x_i \rangle, Q_0^2) \cdot (x_{i+1} - x_i)$ like in Eqn. (6.11) the integral over the the bin width, $\int_{x_i}^{x_{i+1}} F_1(x, Q_0^2)\mathrm{d}x$, was used:

$$\tilde{\Gamma}_1 = \sum_{i=1}^{n} \left(\frac{g_1}{F_1}(\langle x_i \rangle, \langle Q_i^2 \rangle) \cdot \int_{x_i}^{x_{i+1}} F_1(x, Q_0^2)\mathrm{d}x \right). \tag{6.12}$$

Here, i runs over the 15 x bins which fulfill the $Q^2 > 1$ GeV^2 criterion, x_i and x_{i+1} denote the corresponding bin boundaries and $\langle x_i \rangle$, $\langle Q_i^2 \rangle$ are the average values of x, Q^2 in bin i.

To take into account the correlations between the uncertainties of individual data points, the covariance matrix $\mathcal{C}_{g_1/F_1}(i, j)$ has to be used to obtain the statistical error on $\tilde{\Gamma}_1$:

$$\sigma_{\tilde{\Gamma}_1}^2 = \sum_{i=1}^{n} \sum_{j=1}^{n} \mathcal{C}_{g_1/F_1}(i, j) \int_{x_i}^{x_{i+1}} F_1(x)\mathrm{d}x \int_{x_j}^{x_{j+1}} F_1(x)\mathrm{d}x. \tag{6.13}$$

The statistical error on $\tilde{\Gamma}_1$ correctly calculated using the covariance matrix is about 26% smaller than a statistical error obtained with a naïve calculation which takes into account only the diagonal elements of the covariance matrix but neglects the fact that the uncertainties are correlated [HER05].

The resulting first moments of g_1 evolved to $Q_0^2 = 5$ GeV^2 for proton and deuteron in the range $0.02124 < x < 0.9$ are:

$$\tilde{\Gamma}_1^p = \int_{0.02124}^{0.9} g_1^p(x)\,\mathrm{d}x = 0.1246 \pm 0.0032 \pm 0.0074 \tag{6.14}$$

$$\tilde{\Gamma}_1^d = \int_{0.02124}^{0.9} g_1^d(x)\,\mathrm{d}x = 0.0452 \pm 0.0015 \pm 0.0017. \tag{6.15}$$

These HERMES results will be compared to the measurements of other experiments in Section 7.4.

Although the extrapolations to the full x range from 0 to 1 are not yet calculated, the first moment for the deuteron in the measured x range, $\tilde{\Gamma}_1^d$, already allows to estimate the magnitude of the total contribution from the quarks to the nucleon's spin. $\tilde{\Gamma}_1^d$ can be written and approximated as:

$$\begin{aligned}
\tilde{\Gamma}_1^d &= \frac{1-\frac{3}{2}\omega_D}{2}\left[\frac{5}{18}(\Delta u + \Delta\overline{u} + \Delta d + \Delta\overline{d} + \Delta s + \Delta\overline{s}) - \frac{1}{6}(\Delta s + \Delta\overline{s})\right] \\
&= \frac{1-\frac{3}{2}\omega_D}{2}\left[\frac{5}{18}\Delta\Sigma - \frac{1}{6}(\Delta s + \Delta\overline{s})\right] \qquad (6.16) \\
&\overset{\Delta s \simeq 0}{\approx} \frac{1-\frac{3}{2}\omega_D}{2}\left[\frac{5}{18}\Delta\Sigma\right]. \qquad (6.17)
\end{aligned}$$

As $g_1^d(x)$ becomes compatible with zero for $x < 4 \times 10^{-2}$ (and therefore already within the measured range) one may assume that there are no contributions to the integral below this value and a complicated extrapolation towards $x = 0$ can be omitted. In a semi-inclusive analysis of the HERMES data all extracted sea quark distributions were found to be consistent with zero within the uncertainties of the measurement [HERMES05b], allowing the approximation $\Delta s \simeq 0$ in Eq. (6.17) to be made. For $x \to 1$ $g_1(x)$ is also almost zero, but in this region certainly some (small) contribution to the integral is neglected. Under the assumptions and approximations mentioned above and using a value of $\omega_D = 0.05$, a value of $\Delta\Sigma = 0.352 \pm 0.025$ in the measured x-range and evolved to $Q_0^2 = 5$ GeV^2 is found, which is in agreement with the result of the semi-inclusive analysis [HERMES05b] mentioned above.

Assuming SU(3) flavour symmetry one can deduce a corresponding value of $\Delta s + \Delta\overline{s} = -\frac{1}{3}(a_8 - a_0) = -0.076 \pm 0.017$ (with $a_0 = \Delta\Sigma = 0.352 \pm 0.025$ and $a_8 = 3F - D = 0.579 \pm 0.025$) which is of much smaller absolute value than the EMC result ($(\Delta s + \Delta\overline{s}) = -0.190 \pm 0.032 \pm 0.046$) derived with the same method [Muon88] [Muon89].

The value of $\Delta\Sigma$ measured by HERMES is significantly higher than the value determined by EMC ($\Delta\Sigma = 0.120 \pm 0.094 \pm 0.138$) which gave rise to the so-called 'spin crisis'. In consideration of the new HERMES data the fraction of the nucleon's spin originating from the spins of the quarks seems to be larger than assumed so far.

6.4 Systematic uncertainties

An overview of the systematic uncertainties on the measurement is given in Table 6.4. Systematic uncertainties enter the analysis at three different stages:

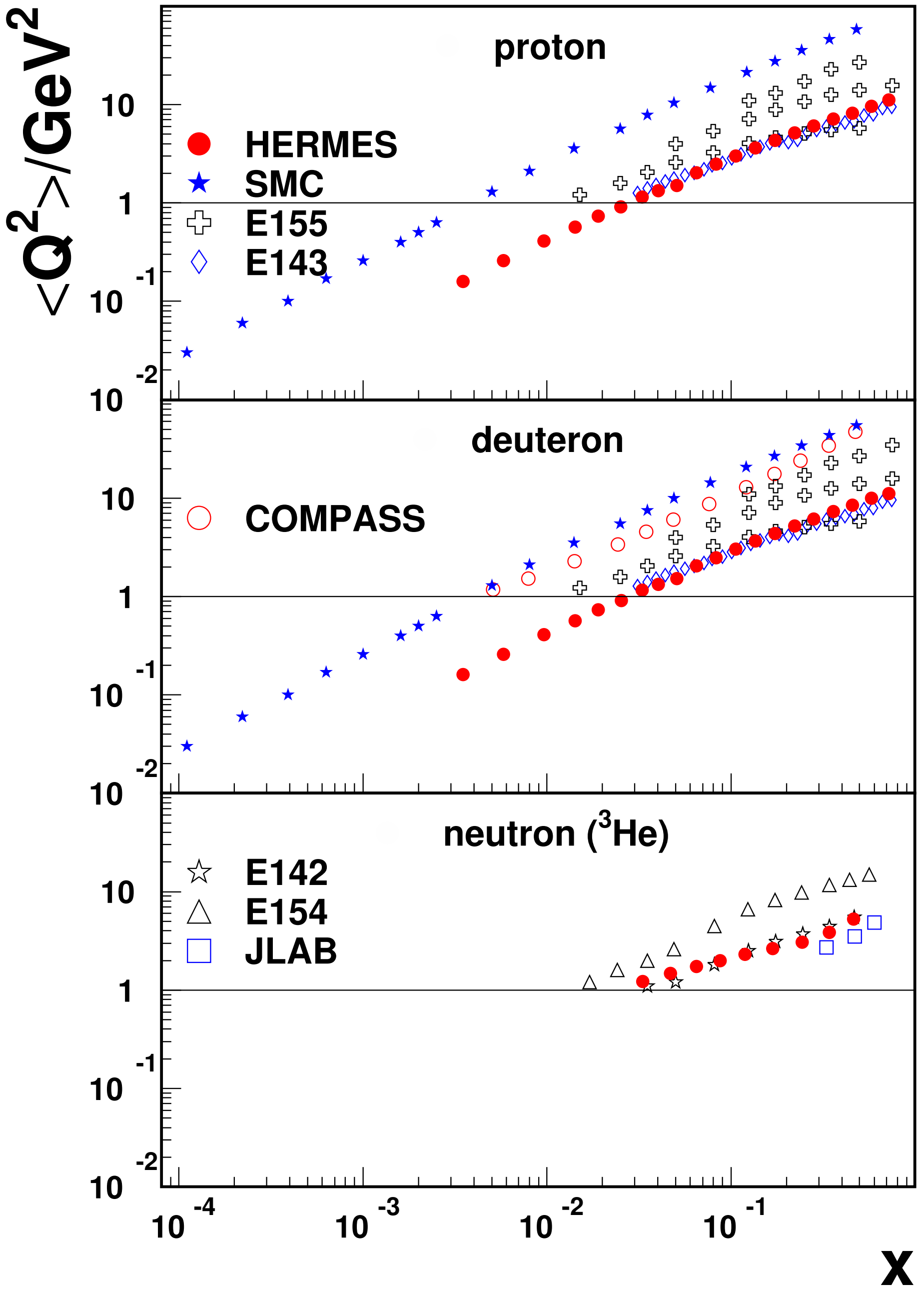

Figure 6.7: Comparison of the average Q^2 values of various experiments [CDNE+04a].

- Experimental uncertainties (e.g. uncertainties on beam and target polarizations) are already present at the level of the measured spin-dependent cross-section asymmetry $A_{||}$.

- Additional uncertainties contribute through the unfolding formalism, e.g. the influence of input parametrizations to the Monte Carlo (A_2, R, F_2, A_1) and uncertainties originating from limited statistics of the Monte Carlo data set used for unfolding.

- At the level of extraction of the structure functions, the uncertainties on parametrizations used in the calculation contribute to the systematic error.

Note that the uncertainties on the parametrizations used in the analysis contribute (to different degree) at two stages of the analysis: the unfolding procedure shows a weak model dependence on the input parametrizations used in the generation of the Monte Carlo, caused by the background subtraction explained in Chapter 5 (see Eq. (5.4)). At the stage of extraction of the structure functions, the uncertainties on the parametrizations contribute again, e.g. the parametrization of $R(x, Q^2)$ affects both the depolarization factor D (Eq. (2.16)) and the spin-independent structure function $F_1(x, Q^2)$ (Eq. (6.4)).

6.4.1 Beam and target polarizations

The experimental systematic uncertainty is dominated by the uncertainties on beam and target polarizations. The polarization values of beam and target were varied within their uncertainties (see Tables 4.3 and 4.4) and the change in the central value of the resulting asymmetry was assigned as systematic error.

6.4.2 Particle identification, contamination of the inclusive DIS sample from hadrons

The PID cut (Eq. (4.5)), which was chosen for this analysis as PID > 1, was varied within the reasonable limits PID > 0 and PID > 2, corresponding to a variation of the lepton/hadron probability ratio by two orders of magnitude. The resulting variations in g_1^p/F_1^p (g_1^d/F_1^d) did not exceed 0.002 (0.001) over the entire x range.

The hadron contamination in the inclusive DIS sample was estimated to be less than 0.2%; the systematic error due to this tiny contamination can be safely neglected [HER05].

	g_1^p/F_1^p	g_1^d/F_1^d	level
beam and target polarization	5.2%	3.8%	experimental
particle identification	<0.002	<0.002	experimental
hadron contamination	negligible	negligible	experimental
luminosity measurement	negligible	negligible	experimental
b_1 (tensor polarization)	–	1%	experimental
detector misalignment	2.5%	2.5%	experimental
reconstruction inefficiencies (App. B)	<0.001	<0.001	unfolding
MC parametrizations (A_2, R, F_2, A_1)	<0.003	<0.003	unfolding
finite MC statistics for unfolding	∼0.005	∼0.004	unfolding
$R(x, Q^2)$ parametrization	6%	4%	extraction
$A_2(x, Q^2)$ parametrization	1%	1%	extraction

additional source of uncertainty on g_1^p *and* g_1^d*:*

	g_1^p, g_1^d	level
$F_2(x, Q^2)$ parametrization (Eq. (6.4))	– (see Section 6.4.8)	extraction

additional source of uncertainty on g_1^n*:*

	g_1^n	level
ω_D (Eq. (6.6))	< 0.0036	extraction

Table 6.1: Sources and magnitudes of systematic uncertainties on g_1/F_1 and g_1. Precise bin-by-bin values of the systematic uncertainties are listed in the tables given in Appendix D.

6.4.3 Structure function b_1^d

The deuteron as a spin-1 target has in addition to the two vector polarization states a third tensor polarization state [Rie05]. A vector-polarized spin-1 target is in general simultaneously tensor-polarized. Thus the measured cross section σ_m does not only depend on the target vector polarization P_T and longitudinal asymmetry $A_{||}$, but also on the target tensor polarization P_{zz} and the corresponding tensor asymmetry A_{zz}:

$$\sigma_m = \sigma_0 \left[1 - P_B P_T A_{||} + \frac{1}{2} P_{zz} A_{zz} \right] . \tag{6.18}$$

The tensor asymmetry introduces an additional term in the expression for $A_{||}$:

$$A_{||} = \frac{\sigma^{\uparrow\uparrow} - \sigma^{\uparrow\downarrow}}{\sigma^{\uparrow\uparrow} + \sigma^{\uparrow\downarrow}} \left[1 + \frac{1}{2} P_{zz} A_{zz} \right] . \tag{6.19}$$

At HERMES the average target tensor polarization P_{zz} was 0.83 ± 0.03. The tensor asymmetry A_{zz} is of the order of 10^{-2} and the systematic error arising from neglecting the tensor term therefore was estimated to be 1% [HER05].

6.4.4 Detector misalignment

Studies concerning the misalignment of the HERMES detector have shown that the two halves of the HERMES spectrometer are not perfectly aligned to each other; with respect to a perfectly aligned detector, the top detector half seems to be tilted by ≈ 1 mrad and the bottom detector half appears to be shifted by ≈ 1 mm [Bru04] [Asc04]. To study the impact of this misalignment on the reconstructed spin asymmetries, two Monte Carlo datasets were produced, one of them simulating a perfectly aligned detector, the other one simulating the scenario described above. Misalignment leads to an overall shift in the kinematic distributions as it affects the reconstructed angles of the particle tracks. Note that detector misalignment cannot be corrected by unfolding as described in Chapter 5 as it is not a stochastic effect. If the magnitude of the misalignment were known exactly it could be perfectly corrected (track by track) by adding appropriate offset values to all measured quantities affected by it. Unfortunately at the time of this analysis the misalignement is still under study and no analytical correction is available. Therefore the above described reasonable scenario was studied in Monte Carlo and the deviations in the central values of the unfolded Monte Carlo asymmetry with respect to the ideally aligned case were assigned as systematic error [HER05], being overall of the order of 2.5%. A detailed discussion of these studies can be found in [Rie05].

6.4.5 Reconstruction inefficiencies

During the unfolding procedure the experimentally observed count rates are corrected for electromagnetic background as explained in Chapter 5. In this correction the reconstruction efficiency has to be taken into account as showers cause events with very high hit multiplicity in the tracking chambers which are rejected by the track reconstruction algorithm. Therefore assuming a reconstruction efficiency of 100% would cause the unfolding algorithm to overcorrect the electromagnetic background. This correction is discussed in Appendix B; the systematic uncertainty on g_1/F_1 due to this correction is estimated to be smaller than 0.001 for both proton and deuteron.

6.4.6 Monte Carlo input parametrizations

Within the acceptance the unfolding algorithm is expected to be independent on the model of the cross section, as can be seen from Eq. (5.3). Possible effects from modelling it outside the acceptance which can contribute through spin-dependent background rates (Eq. (5.4)) have been studied, using several Monte Carlo samples for both the proton and the deuteron with parameterization sets different from the default one. No significant deviations were revealed in the unfolded Born asymmetry. As a measure for the accuracy of these studies, the deviations in the unfolded Born asymmetry $A_{||}^{B}$ found between the different samples and the default one do not exceed 0.003. This approximately corresponds to a 1σ accuracy of the Monte Carlo test samples used. Note that this accuracy is about three times higher than that of the data sample [HER05].

6.4.7 Finite Monte Carlo statistics

Although this uncertainty due to finite Monte Carlo statistics is listed among the systematic uncertainties, it is in a certain sense a statistical error. The statistical uncertainties of the Monte Carlo data enter via the eXperimental count rates $n^X_{\uparrow\uparrow}(i)$, $n^X_{\uparrow\downarrow}(i)$ and the Born count rates $n^B_{\uparrow\uparrow}(j)$, $n^B_{\uparrow\downarrow}(j)$ the cross section normalized migration matrices $S_{\uparrow\uparrow}(i,j)$, $S_{\uparrow\downarrow}(i,j)$ (Eq. (5.3)). Thus, each matrix element is afflicted with a statistical uncertainty. To propagate these statistical uncertainties through the unfolding algorithm with its matrix inversion and evaluate the influence on the unfolded Born level asymmetry $A_{||}^{B}$ a variational ansatz was used: all matrix elements were randomly varied at the same time, each element within its respective statistical uncertainty according to a Gauss distribution. Then the measured asymmetry was unfolded using this modified migration matrix and the resulting Born level asymmetry values for each bin were stored in histograms. This procedure was repeated $10,000$ times, resulting in $10,000$ possible Born level asymmetries based on the same input asymmetry. The standard deviation of the distribution found for each bin in the respective histogram was then assigned as 'systematic' uncertainty due to finite Monte Carlo statistics. Compared to the statistical uncertainty of the measurement this uncertainty is already very small and is expected to decrease further until the upcoming HERMES g_1 publication [HERMES05a] by an increase in Monte Carlo statistics.

6.4.8 Parametrizations used in the extraction of the structure functions

The systematic uncertainties arising from the parametrizations which were used in the extraction of the structure functions were obtained from the difference in the central values of the extracted structure functions observed between *a)* the default parametrizations and *b)* parametrizations which were changed within a reasonable margin of uncertainty as discussed below.

R parametrization

As default parametrization for R the parametrization $R1990$ [WRB+90] was used which is only valid for $Q^2 > 0.3$ GeV^2. Below this value R was forced to zero for $Q^2 \rightarrow 0$ GeV^2 to respect the fact that for real photons $R = 0$. The systematic error on the extracted asymmetry was obtained by extracting the asymmetry once with the default R parametrization described above and once with $R = R1990 + dR$, where dR is the uncertainty on the parametrization given in [WRB+90]. For the kinematic region $Q^2 < 0.3$ GeV^2 the expression $R = R(Q^2 = 0.3\,\mathrm{GeV}^2) + dR(Q^2 = 0.3\,\mathrm{GeV}^2)$ was used.

The systematic uncertainty on g_1/F_1 arising from the uncertainty on R was determined to be 6% for the proton and 4% for the deuteron.

A_2 parametrization

The systematic uncertainty on g_1/F_1 caused by the A_2 parametrizations (see Eq. (6.3) and Fig. 6.1) was estimated to be of the order of 1% for both proton and deuteron. This source of systematic uncertainty was at the time of completion of this thesis still under investigation and changes are expected. Final values will be given in the upcoming HERMES g_1 publication [HERMES05a].

F_2 parametrization

The default parametrization for F_1 used in this analysis is based on the ALLM F_2 parametrization [AL97] as explained in Section 6.1. The ALLM parametrization however is given without uncertainty. At the time of completion of this thesis the systematic uncertainty arising from the used F_2 parametrization is still being studied. Therefore no systematic error due to the F_2 parametrization used at the stage of extraction was assigned in the analysis presented here. Final values will be given in the upcoming HERMES g_1 publication [HERMES05a].

ω_D parameter

The parameter for the probability of the deuteron to be in the D orbital state was varied within the range $\omega_D = 0.05 \pm 0.01$ (see Section 6.2.2) and half of the change in the resulting values for $g_1^n(x)$ was assigned as systematic uncertainty. The uncertainty is found to be less than 0.0036 over the entire x range apart from the lowest data point in x where the uncertainty is 0.0089.

Chapter 7

Comparison to world data

7.1 Proton

HERMES has measured the spin-dependent structure function $g_1^p(x, Q^2)$ of the proton with an accuracy comparable to the hitherto most precise measurements of the SLAC experiments E143 [E14398] and E155 [E15500]. The results of these measurements agree very well as shown in the upper panels of Figures 7.1 (for better visibility magnified in Fig. 7.2), 7.4 (magnified in Fig. 7.5) and 7.9. The HERMES measurement extends to lower values in x than the SLAC data points into an region up to now only covered by SMC data [Muon98]. It should be noted that the HERMES data points for $x < 0.03$ are measured at $\langle Q^2 \rangle < 1$ GeV^2 (see Q^2 comparison in the lower panel of Fig. 7.1).

The structure function ratio g_1/F_1 of the proton (Fig. 7.1 upper panel and Fig. 7.2) shows no significant Q^2 dependence although the range of the various measurements from different experiments spans about one order of magnitude in $\langle Q^2 \rangle$ (Fig 6.7). This leads to the conclusion that $g_1(x, Q^2)$ and $F_1(x, Q^2)$ must have a very similar Q^2 dependence[1] so that the ratio is independent of Q^2,

$$\frac{g_1(x, Q^2)}{F_1(x, Q^2)} = \frac{g_1(x)}{F_1(x)}. \tag{7.1}$$

Even at very low values of Q^2, where the transition from lepto-production to photo-production occurs and the application of perturbative QCD becomes questionable, the Q^2 dependence of g_1 and F_1 seems to be very similar as can be seen from the agreement between the SMC and the HERMES data points. Apparentely higher-twist contributions and QCD radiative corrections have similar relative magnitudes for both structure functions and therefore cancel in the ratio g_1/F_1.

[1] This behaviour was already used in Section 6.3 for the evolution of the g_1 data points from their measured $\langle Q^2 \rangle$ value to a common value of Q_0^2 in order to calculate the first moment Γ_1.

In the extracted structure function $g_1^p(x, Q^2)$ however the Q^2 dependence is visible as one can see in Figs. 7.4 and 7.5 (where all data points are shown at their *measured* value of $\langle Q^2 \rangle$), e.g. by comparing the values of HERMES and SMC which are different by one order of magnitude in $\langle Q^2 \rangle$. For $x < 0.1$ the HERMES measurement suggests a constant value for $g_1^p(x, Q^2)$ of about 0.25 while SMC measured values around 0.4 in the same region.

7.2 Deuteron

Based on more than 10 million DIS events, HERMES was able to perform the up to now most precise measurement of the deuteron spin-structure function $g_1^d(x, Q^2)$. The results are shown in the middle panels of Figures 7.1 (for better visibility magnified in Fig. 7.3), 7.4 (magnified in Fig. 7.6) and 7.9 (magnified in Fig. 7.10). The available world data for g_1^d/F_1^d are considerably less accurate than in case of the proton and show large point-to-point fluctuations but within the experimental uncertainties also here no significant Q^2 dependence can be observed.

In the region $x < 0.03$, a strong disagreement between the HERMES and SMC measurements is found: SMC clearly favours negative values for g_1^d while the HERMES data are compatible with zero in the same region. On the other hand, the COMPASS[2] results for $x < 0.03$ are consistent with zero and don't show the tendency of the SMC data of negative g_1^d values [COMPASS05a].

If g_1^d is zero in this x range one can conclude that the spin-dependent quark distributions $\Delta u(x)$ and $\Delta d(x)$ are of similar magnitude but have opposite signs and therefore cancel. On the other hand negative values of g_1^d could either be attributed to $|\Delta d(x)| > |\Delta u(x)|$ or to an in total negative sea quark helicity distribution.

7.3 Neutron

The high precision of the deuteron dataset allowed HERMES the so far most precise determination of the spin-dependent neutron structure function $g_1^n(x, Q^2)$ based on $g_1^p(x, Q^2)$ and $g_1^d(x, Q^2)$ measurements (Fig. 7.4 lower panel, magnified in Fig. 7.7, and 7.9 lower panel).

Compared to the SLAC data, the HERMES measurement shows much smaller point-to-point fluctuations and restricts $g_1^n(x, Q^2)$ now very well.

In the low-x region, the HERMES and SMC data deviate significantly which is caused by the differences in the proton and deuteron measurements: SMC favours more positive values for the proton while the SMC deuteron points are clearly negative where the HERMES measurement is compatible with zero. This leads to the observed difference in $g_1^n(x, Q^2)$.

[2]The COMPASS experiment at CERN uses a polarized LiD target.

Based on previous measurements by E143 and SMC a dramatic drop-off of $g_1^n(x, Q^2)$ for $x \to 0$ was discussed as shown in Fig. 7.8 [E15497b] [E14296]. The new HERMES data presented in this analysis restrict $g_1^n(x, Q^2)$ much better now and exclude such a behaviour in the low x region.

7.4 First moments of proton and deuteron

The first moments in the measured range $\tilde{\Gamma}_1^p$ and $\tilde{\Gamma}_1^d$ calculated in Section 6.3 can be compared to the results obtained by E143 and SMC when restricting the integration to a common x range [E14398] [CDNE$^+$04b]:

Expt.	target	Q^2	x range	$\tilde{\Gamma}_1 = \int g_1(x)\mathrm{d}x$	HERMES $\tilde{\Gamma}_1$
E143	proton	5 GeV^2	$0.03 < x < 0.8$	$0.117 \pm 0.003 \pm 0.006$	0.1174 ± 0.0027
SMC	proton	5 GeV^2	$0.03 < x < 0.7$	0.128 ± 0.006	0.1141 ± 0.0026
E143	deuteron	5 GeV^2	$0.03 < x < 0.8$	$0.043 \pm 0.003 \pm 0.002$	0.0433 ± 0.0013
SMC	deuteron	5 GeV^2	$0.03 < x < 0.7$	0.043 ± 0.007	0.0416 ± 0.0013

The agreement between the measurements by E143 and HERMES is excellent. In case of the proton measurement the statistical accuracy is about the same for E143 and HERMES, for the deuteron measurement HERMES is able to improve the accuracy of the measurement by more than a factor of two in the x range covered by E143.

E155 measured a first moment for deuteron of $\tilde{\Gamma}_1^d = 0.0408 \pm 0.0025 \pm 0.0024$ (evolved to $Q^2 = 5$ GeV^2) in the range $0.01 < x < 0.9$ [E15599a]. The first moment of the HERMES deuteron measurement was not calculated in this range as it would imply to include our data at a measured $Q^2 < 1$ GeV^2 to cover the low-x region.

The moments measured by SMC deviate from the ones measured by HERMES in the same x range as already expected from Fig. 7.4.

7.5 The spin puzzle

Understanding the nucleon's spin structure turned out to be a much more complex problem than assumed originally and a detailed decomposition of the spin of the nucleon is still missing. The HERMES data support a scenario where (at $Q_0^2 = 5$ GeV^2) about 35% of the nucleon's spin arise from the spins of the quarks while the sea quark polarizations are consistent with zero within experimental uncertainties.

There are indications that the gluon polarization is substantial and positive, but the precise value is poorly constrained and the extraction is model dependent. Based on the spin asymmetry in the photo-production of pairs of high-p_T hadrons HERMES determined a value of $\Delta G/G = 0.41 \pm 0.18 \pm 0.03$ [HERMES00]. More precise measurements of the gluon polarization will be performed by the COMPASS experiment [COMPASS05b] and the RHIC spin program [PHENIX98].

Recent measurements by HERMES on a transversely polarized target indicate a non-zero result for the SIVERS function which might provide access to the up to now completely unknown orbital angular momentum of the quarks, L_z^q [HERMES05c].

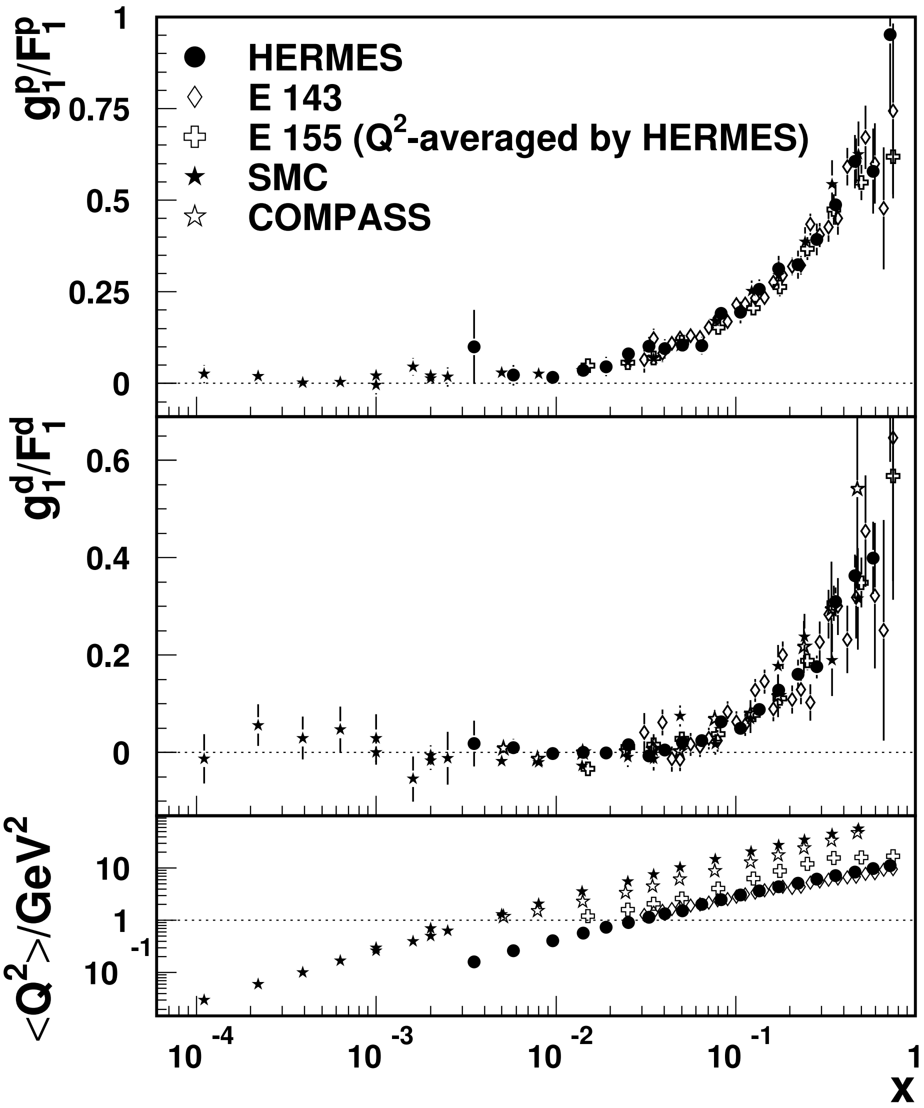

Figure 7.1: Structure function ratios g_1^p/F_1^p and g_1^d/F_1^d [CDNE$^+$04a] superimposed with results from SMC [Muon98] [Muon99] [Muon00], COMPASS [COMPASS05a], E143 [E14398] and E155 [E15599a], [E15500]. Although these experiments cover a range of about one order of magnitude in Q^2 as shown in the lowest panel, the measured values of g_1/F_1 are compatible as especially visible in the proton measurements due to the better accuracy of the data points. This leads to the conclusion that $g_1(x, Q^2)$ and $F_1(x, Q^2)$ have a very similar (if not identical) Q^2 dependence. The error bars represent total errors. The upper two panels are magnified for better visibility in Fig. 7.2 and Fig. 7.3.

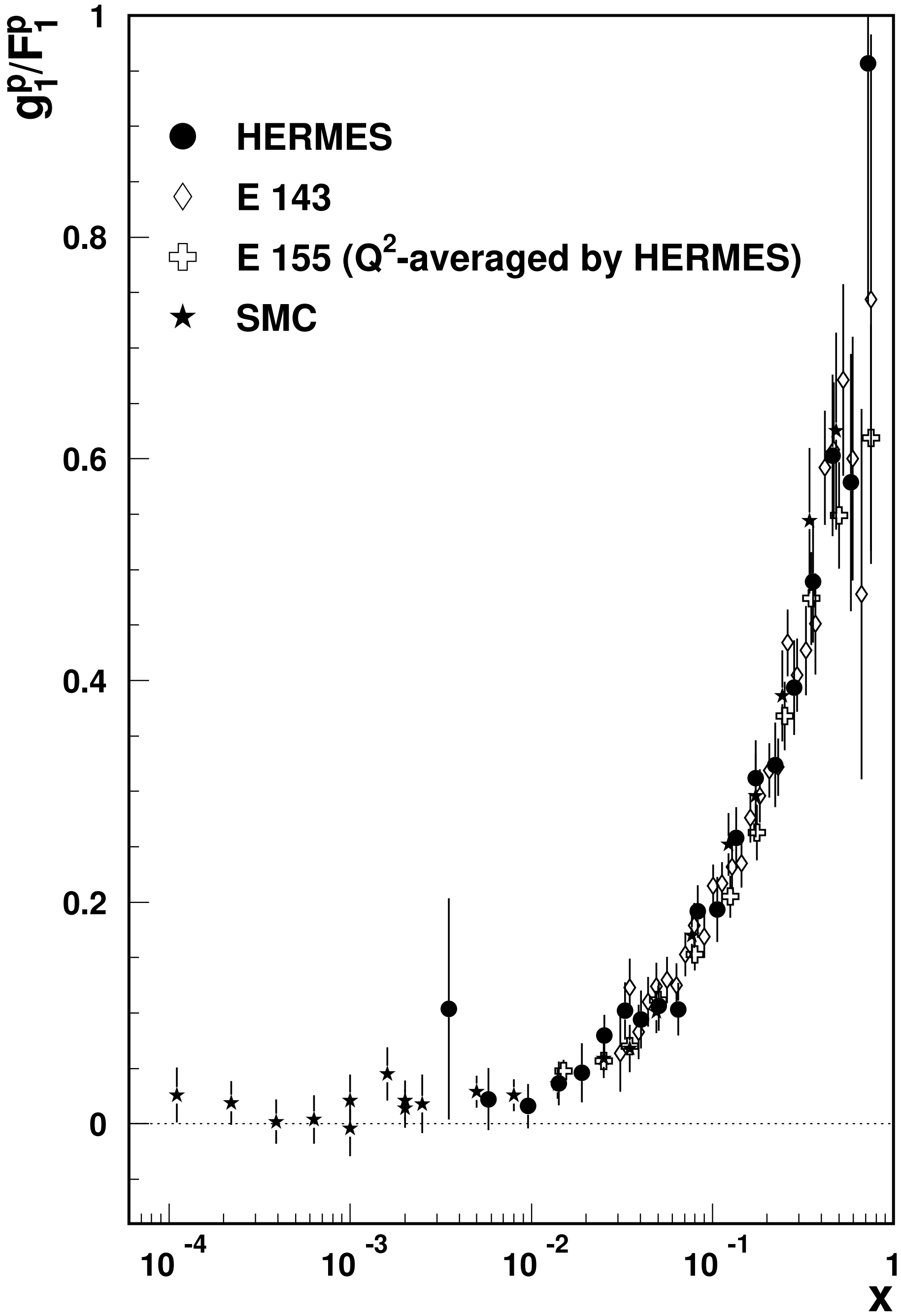

Figure 7.2: Structure function ratio g_1^p/F_1^p superimposed with results from SMC [Muon98] [Muon99] [Muon00], E143 [E14398] and E155 [E15599a], [E15500].

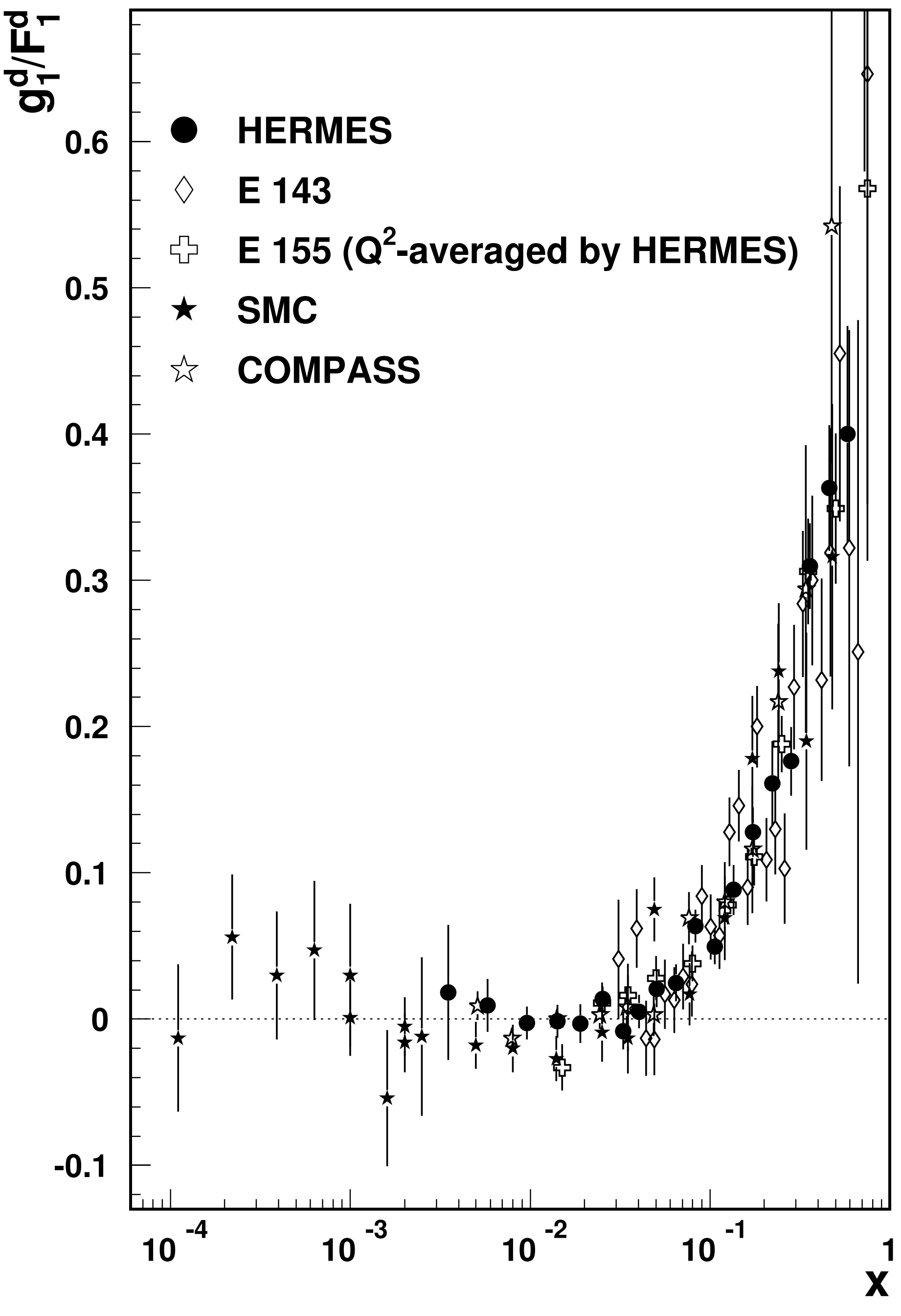

Figure 7.3: Structure function ratio g_1^d/F_1^d superimposed with results from SMC [Muon98] [Muon99] [Muon00], COMPASS [COMPASS05a], E143 [E14398] and E155 [E15599a], [E15500].

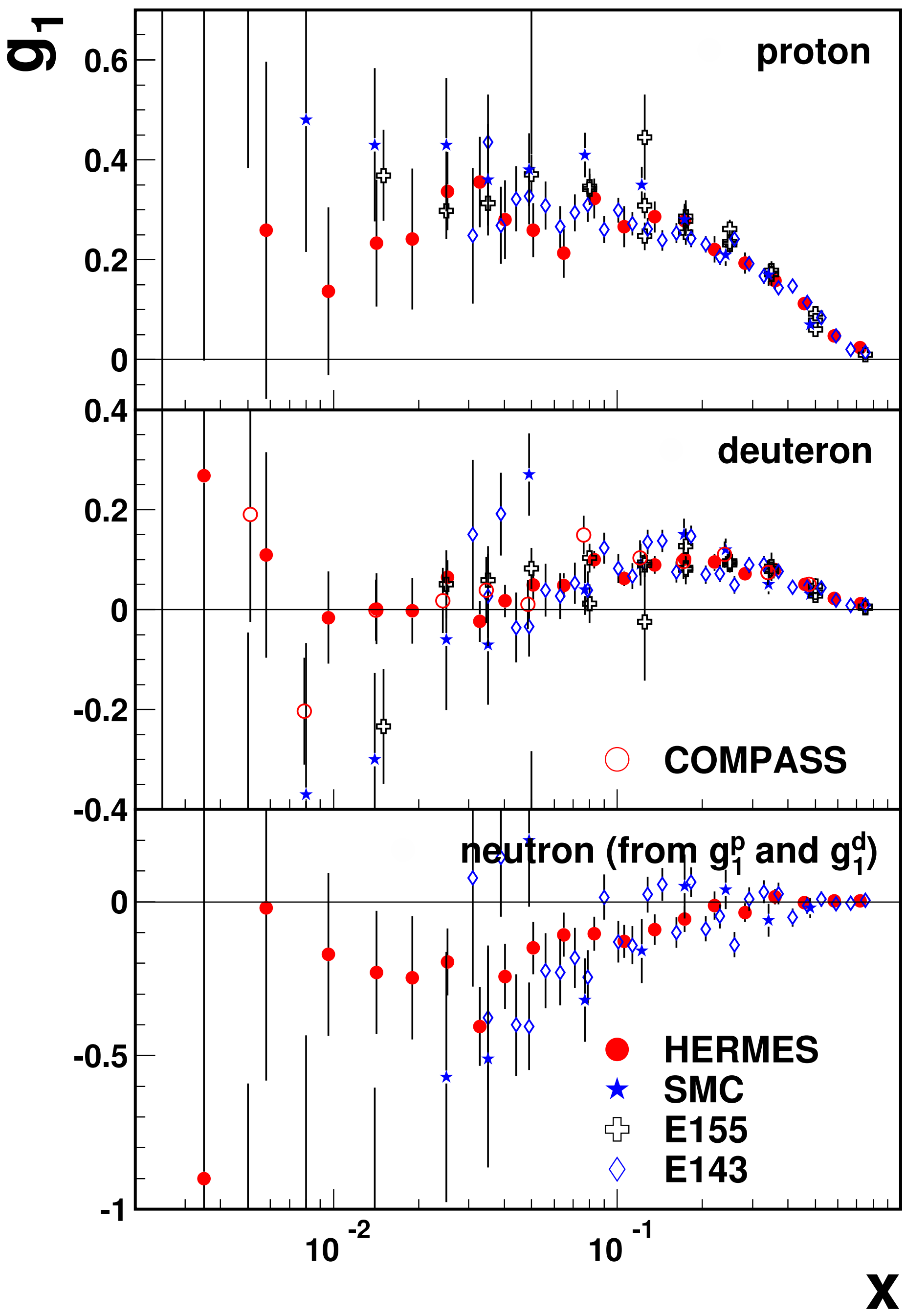

Figure 7.4: g_1^p, g_1^d and g_1^n compared to other experiments [CDNE+04a]. The error bars of the HERMES points reflect the quadratic sum of statistical and systematic uncertainties. The data of all experiments are shown at their respective measured average Q^2 values. For better visibility the three panels are magnified in Figures 7.5, 7.6 and 7.7.

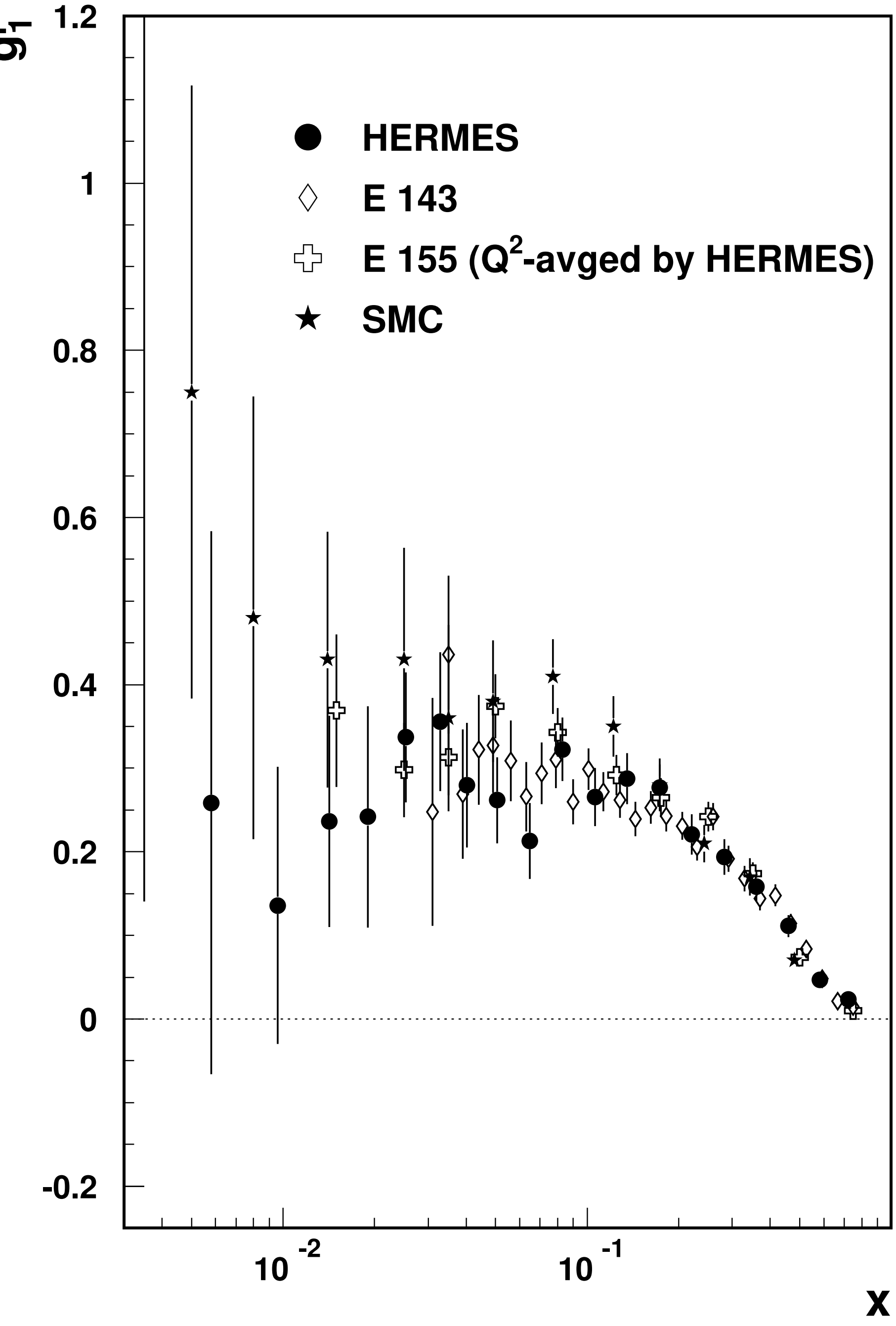

Figure 7.5: g_1^p compared to other experiments [CDNE+04a]. The error bars show total uncertainties. The data of all experiments are shown at their respective measured Q^2 values.

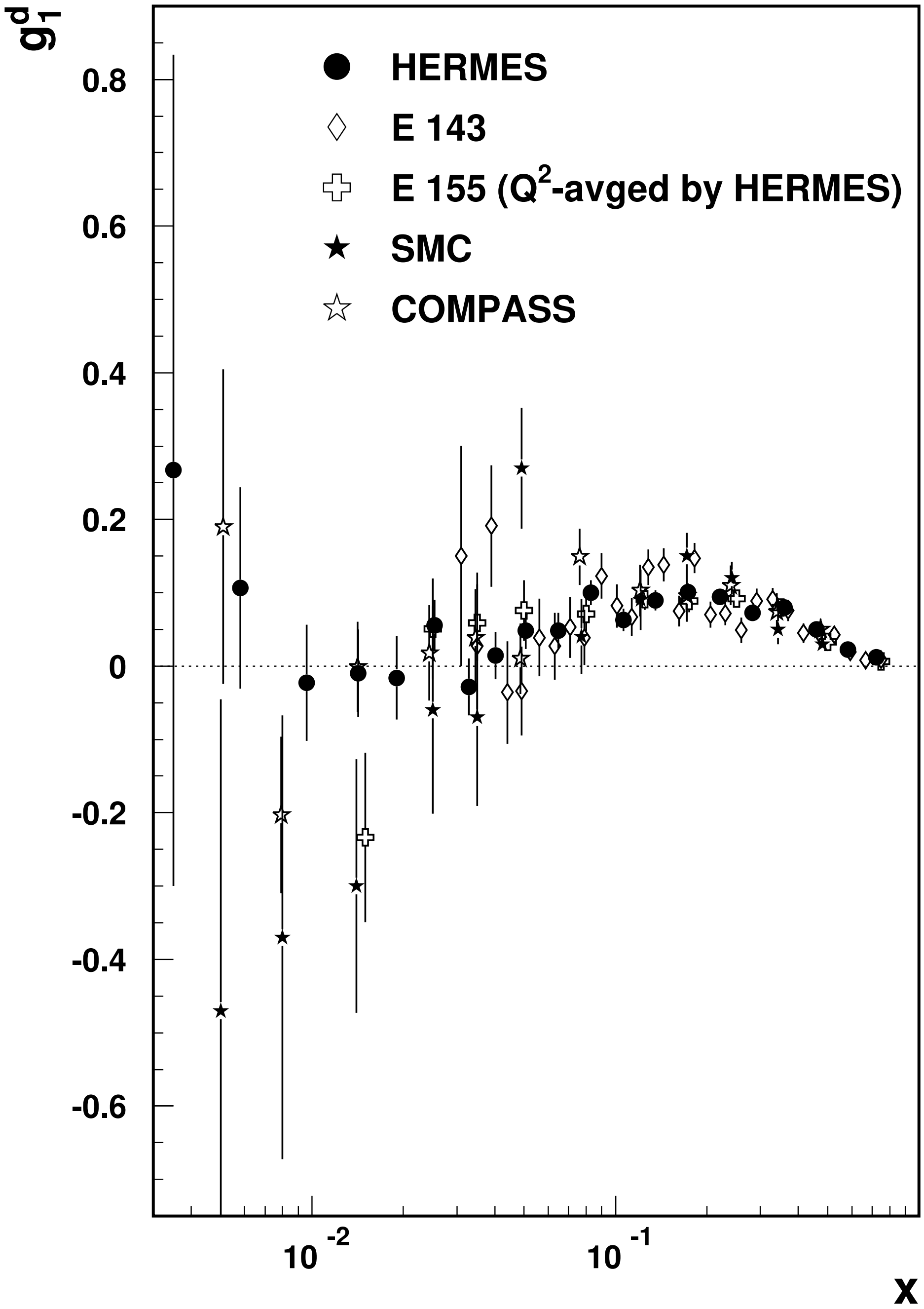

Figure 7.6: g_1^d compared to other experiments [CDNE$^+$04a]. The error bars show total uncertainties. The data of all experiments are shown at their respective measured Q^2 values.

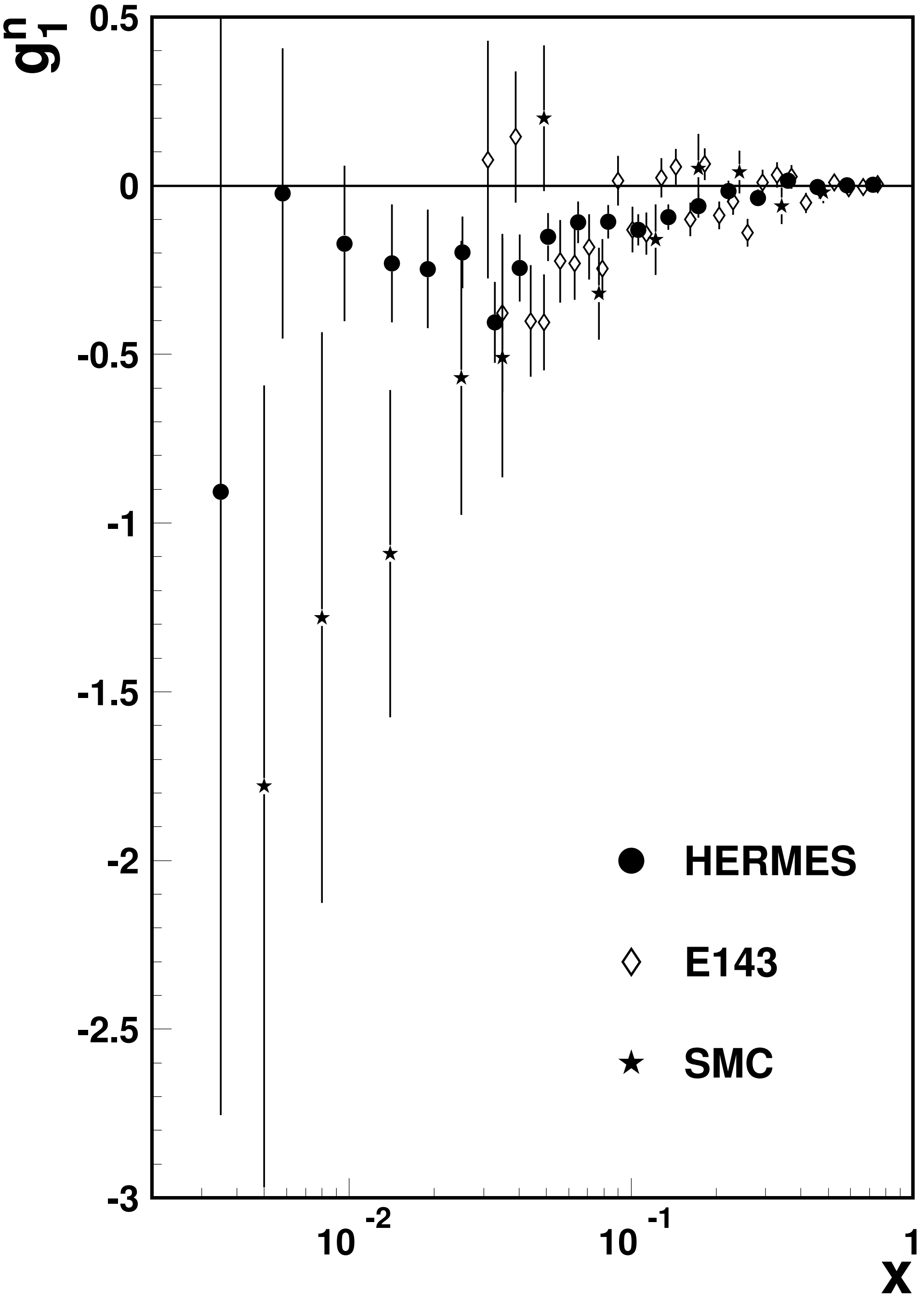

Figure 7.7: g_1^n (extracted from g_1^p and g_1^d) compared to other experiments [CDNE+04a]. The error bars show total uncertainties. The data of all experiments are shown at their respective measured Q^2 values.

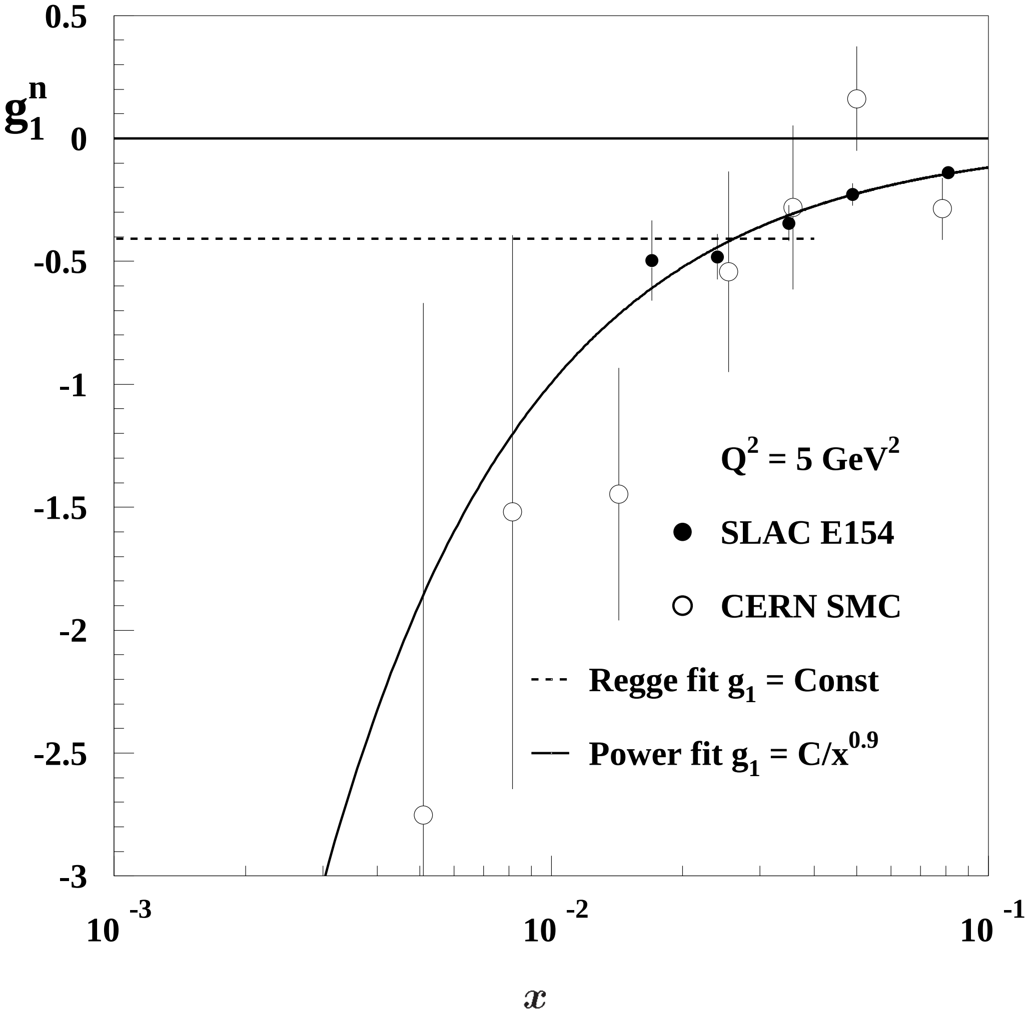

Figure 7.8: Low x extrapolations for g_1^n as discussed in [E15497b]. The new HERMES data presented in this analysis (see Fig. 7.7) restrict g_1^n much better now and exclude such a dramatic drop-off for $x \rightarrow 0$.

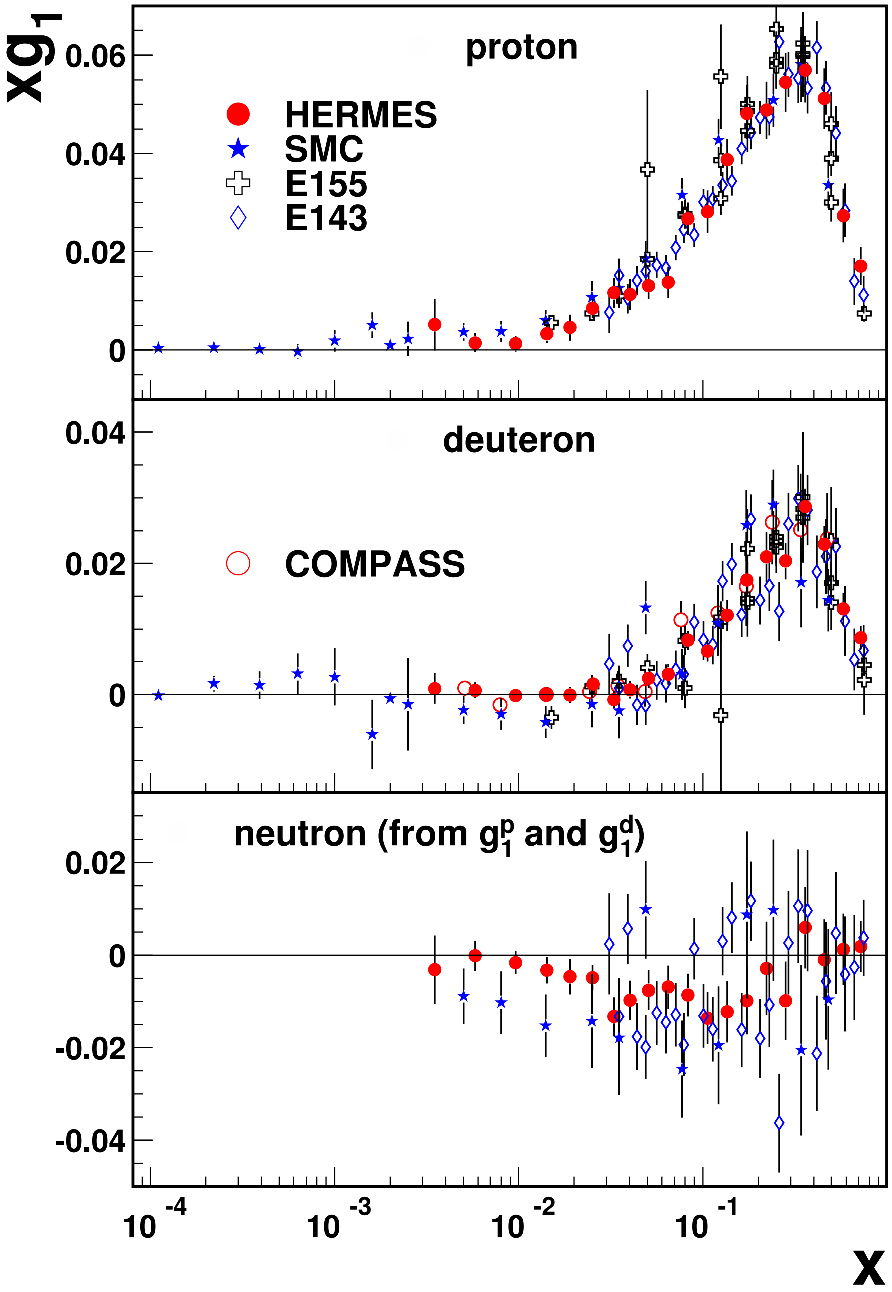

Figure 7.9: Comparison with world data on xg_1^p, xg_1^d and xg_1^n [CDNE+04a]. The error bars represent total uncertainties. All data points are shown at their measured values of Q^2 (compare Fig. 6.7). The middle panel is magnified for better visibility in Fig. 7.10.

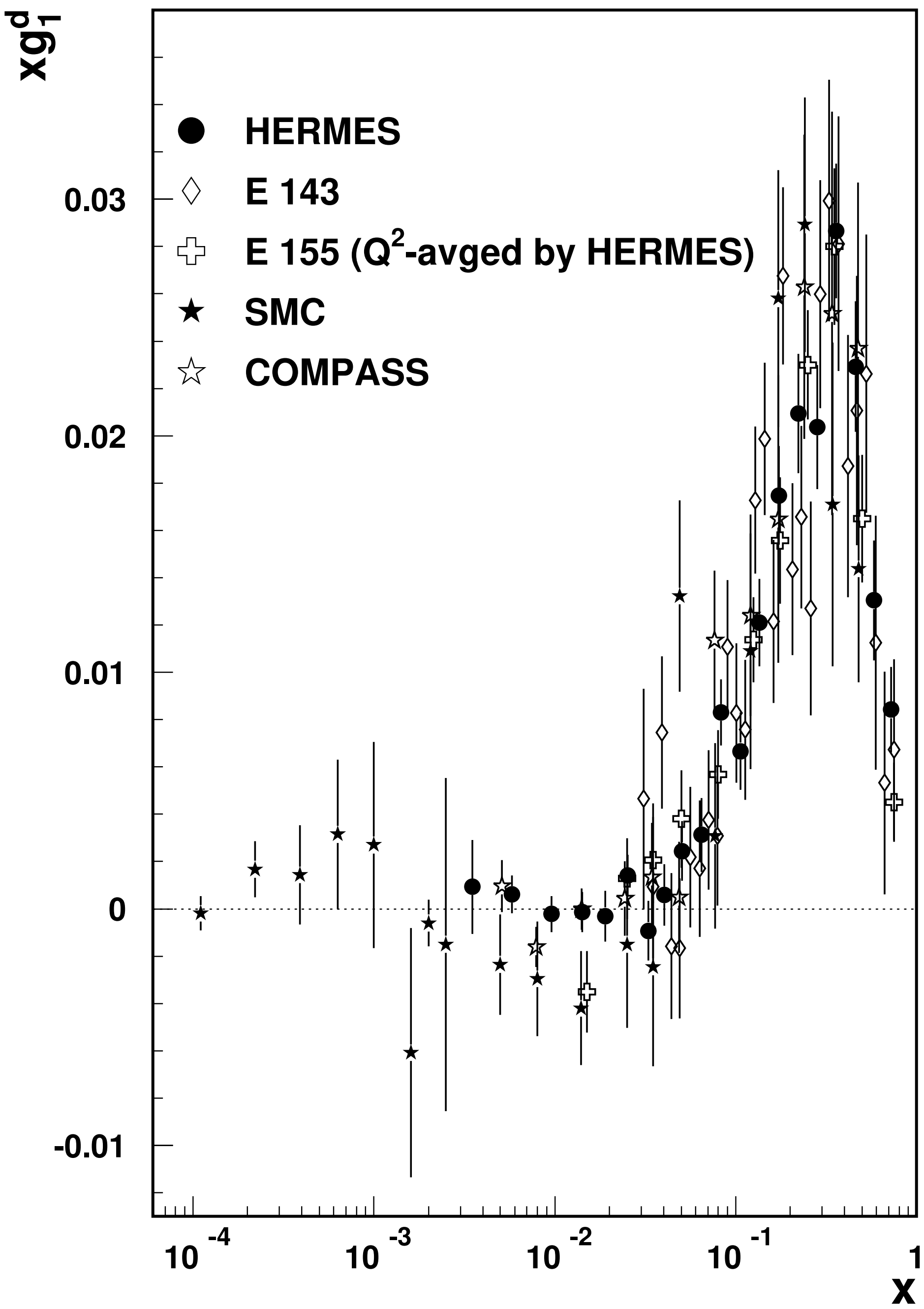

Figure 7.10: Comparison with world data on xg_1^d. The E155 values have been Q^2-averaged by HERMES [CDNE+04a]. Note that the HERMES data show significantly smaller point-to-point fluctuations than the hitherto available data on xg_1^d.

Chapter 8

Summary

HERMES has measured the spin-dependent structure functions $g_1(x, Q^2)$ of the proton and the deuteron in the kinematic range $0.0021 < x < 0.9$ and $0.1\ \mathrm{GeV}^2 < Q^2 < 20\ \mathrm{GeV}^2$. Combining the two data samples the neutron spin-dependent structure function $g_1^n(x, Q^2)$ was calculated.

The HERMES proton data have a statistical precision comparable to the hitherto most precise data from SLAC in the same kinematic range. In the structure function ratio g_1^p/F_1^p very good agreement is seen between all experiments and no significant Q^2 dependence can be observed. The low-x HERMES data points are measured at $\langle Q^2 \rangle$ values down to $0.16\ \mathrm{GeV}^2$ where the applicability of pQCD becomes questionable. It may be concluded that even in this kinematic region QCD radiative corrections and higher-twist effects are very similar for both g_1^p and F_1^p and therefore cancel in the ratio.

The HERMES deuteron measurement, based on more than 10 million DIS events, constitutes the presently most precise determination of the spin-dependent structure function $g_1^d(x, Q^2)$ of the deuteron. The available world data for g_1^d/F_1^d are considerably less accurate than those of the proton but within the experimental uncertainties also here no significant Q^2 dependence can be observed. In the region $x < 0.03$ a disagreement between HERMES and SMC measurements is observed: SMC favours negative values for g_1^d while the HERMES data are compatible with zero in the same region. In agreement with HERMES, the COMPASS results for $x < 0.03$ are consistent with zero.

The presently most precise determination of the spin-dependent structure function g_1^n of the neutron is obtained by combining the HERMES high precision deuteron and proton data.

In the HERMES analysis, the two measured asymmetries were corrected for detector smearing and QED radiative effects by applying an unfolding algorithm. As a consequence the resulting data points are not any longer systematically but statistically correlated. The correlation matrix contains the full information on the correlation between the statistical uncertainty of the data points. Hence it is mandatory to take into account its off-diagonal elements when using the data for a fit or for the calculation of moments to avoid overestimating the uncertainties.

A fair comparison of the statistical power of different experiments is given by the accuracy of moments of structure functions. The HERMES g_1 measurement on the deuteron improves by more than a factor of two the precision of existing data in the range $0.03 < x < 0.8$.

Based on the first moment $\tilde{\Gamma}_1^d = \int g_1^d(x)\,\mathrm{d}x$ within the measured x range the fraction of the nucleon's spin originating from the spins of the quarks was calculated to be $\Delta\Sigma = 0.352 \pm 0.025$. This value is about three times as high as the value determined by EMC which caused the so-called 'spin crisis'.

Chapter 9

Zusammenfassung

Das HERMES-Experiment am Deutschen Elektronen-Synchrotron in Hamburg hat die spinabhängigen Strukturfunktionen $g_1(x, Q^2)$ des Protons und des Deuterons im kinematischen Bereich $0.0021 < x < 0.9$ und 0.1 GeV^2 $< Q^2 < 20$ GeV^2 mit hoher Genauigkeit vermessen. Basierend auf diesen beiden Messungen wurde die spinabhängige Strukturfunktion $g_1^n(x, Q^2)$ des Neutrons berechnet.

Die Messung der Protonen-Spinstrukturfunktion $g_1^p(x, Q^2)$, die von HERMES an einem polarisierten Wasserstoff-Gastarget vorgenommen wurde, ist bezüglich ihrer statistischen Präzission mit den bislang genauesten Messungen am SLAC im gleichen kinematischen Bereich vergleichbar. Ein Vergleich des Strukturfunktionsverhältnisses g_1^p/F_1^p zeigt sehr gute Übereinstimmungen zwischen den Messungen verschiedener Experimente und es ist keine signifikante Abhängigkeit von Q^2 zu beobachten. Die bei sehr kleinen x-Werten gemessenen HERMES Datenpunkte sind zugleich bei sehr kleinen Werten von Q^2 gemessen – bis hinunter zu $\langle Q^2 \rangle = 0.16$ GeV^2 – und liegen somit in einem kinematischen Bereich, in dem die Anwendung der quantenchromodynamischen Störungsrechnung fragwürdig wird. Die beobachtete Q^2-Unabhängigkeit von $g_1^p(x, Q^2)/F_1^p(x, Q^2)$ legt die Schlussfolgerung nahe, dass selbst unter diesen Bedingungen sowohl für $g_1^p(x, Q^2)$ als auch für $F_1^p(x, Q^2)$ QCD Strahlungskorrekturen und *higher-twist*-Effekte sehr ähnlich sind und sich daher im Strukturfunktionsverhältnis aufheben.

Die HERMES Deuterium-Messung basiert auf mehr als 10 Millionen tiefunelastischen Streuereignissen und ist die bislang präziseste verfügbare Messung der Strukturfunktion $g_1^d(x, Q^2)$ des Deuterons. Obgleich die verfügbaren Weltdaten hier beträchtlich weniger genau sind als im Fall des Protons und starke Fluktuationen von Datenpunkt zu Datenpunkt zeigen, ist auch hier keine signifikante Q^2-Abhängigkeit des Strukturfunktionsverhältnisses g_1^d/F_1^d zu beobachten. Im Bereich $x < 0.03$ weichen die von HERMES gemessenen Daten deutlich von den Resultaten des SMC-Experiments ab: Die SMC-Daten zeigen eine deutliche Tendenz zu negativen Werten von g_1^d, während die HERMES-Daten im gleichen Bereich mit Null verträglich sind. Die kürzlich veröffentlichten Messergebnisse des COMPASS-Experiments hingegen sind – in Übereinstimmung mit den HERMES-Ergebnissen – im Bereich $x < 0.03$ ebenfalls mit Null konsistent.

Durch Kombination der von HERMES an Proton und Deuteron gemessenen Strukturfunktionen konnte die zur Zeit präziseste Bestimmung der spinabhängigen Neutron-Strukturfunktion g_1^n in diesem kinematischen Bereich vorgenommen werden.

Die gemessenen Spinasymmetrien wurden mittels eines Entfaltungsalgorithmus um Verschmierungseffekte, die die Messung aufgrund von Detektor-*Smearing* und QED-Strahlungseffekten verfälschen, berichtigt. Diese Korrektur hat zur Folge, dass die Datenpunkte nunmehr nicht mehr systematisch, dafür aber statistisch korreliert sind. Die Korrelationsmatrix enthält die Information über diese Korrelationen zwischen den statistischen Fehlerbalken der Datenpunkte. Daher ist es zwingend erforderlich, die Korrelationsmatrix zu berücksichtigen, wenn die Datenpunkte für einen *fit* oder für die Berechnung von Momenten verwendet werden, da man andernfalls die statistischen Fehler überschätzen würde.

Die statistische Präzission verschiedener Experimente lässt sich anhand der statistischen Genauigkeit der Momente der Strukturfunktionen vergleichen. Dabei zeigt sich, dass die HERMES Deuteron-Messung die Genauigkeit bisheriger Messungen im kinematischen Bereich $0.03 < x < 0.8$ um mehr als einen Faktor von zwei verbessert.

Basierend auf dem ersten Moment der Deuteron-Spinstrukturfunktion im gemessenen x-Bereich, $\tilde{\Gamma}_1^d = \int g_1^d(x)\,\mathrm{d}x$, wurde der Anteil des Nukleonen-Spins, der von den Spins der Quarks herrührt, als $\Delta\Sigma = 0.352 \pm 0.025$ bestimmt. Dieser Wert ist etwa dreimal so gross wie der von EMC bestimmte Wert, der 1987 die sogenannte 'Spin-Krise' auslöste.

Appendix A

Averaging of correlated quantities

A.1 Weighted average of correlated quantities

An expression for the weighted average of correlated quatities [CDNE+04a] [HER05] can be derived starting from the χ^2 definition,

$$\chi^2 = (\mathbf{y} - F\,\mathbf{I})^T \;\; \mathcal{C}^{-1} \;\; (\mathbf{y} - F\,\mathbf{I}) \tag{A.1}$$

where $\mathbf{y}$ is the vector of n measurements, F is the functional expression to be fitted (in our case a constant), $\mathcal{C}$ is the covariance matrix of the measurements and $\mathbf{I}$ is a vector of n components which are all equal 1. The value of F is optimized by minimizing χ^2 with respect to F:

$$\frac{\partial \chi^2}{\partial F} = -\mathbf{I}^T\mathcal{C}^{-1}\mathbf{y} - \mathbf{y}^T\mathcal{C}^{-1}\mathbf{I} + 2F\;(\mathbf{I}^T\mathcal{C}^{-1}\mathbf{I}) \stackrel{!}{=} 0 \tag{A.2}$$

so that

$$F = (\mathbf{I}^T\mathcal{C}^{-1}\mathbf{I})^{-1}\mathbf{I}^T\mathcal{C}^{-1}\mathbf{y} = \mathbf{A}\,\mathbf{y}. \tag{A.3}$$

Note that $(\mathbf{I}^T\mathcal{C}^{-1}\mathbf{I})^{-1}$ is a scalar quantity and therefore commutes with the vectors and the matrix in the equation. The covariance of F is given by:

$$\begin{aligned}
\sigma_F^2 &= \left(\frac{\partial F}{\partial \mathbf{y}}\right)\mathcal{C}\left(\frac{\partial F}{\partial \mathbf{y}}\right)^T = \mathbf{A}\,\mathcal{C}\,\mathbf{A}^T = \\
&= (\mathbf{I}^T\,\mathcal{C}^{-1}\,\mathbf{I})^{-2}\,(\mathbf{I}^T\,\mathcal{C}^{-1})\,\mathcal{C}\,(\mathbf{I}^T\,\mathcal{C}^{-1})^T \\
&= (\mathbf{I}^T\,\mathcal{C}^{-1}\,\mathbf{I})^{-1}.
\end{aligned} \tag{A.4}$$

Applying this formalism to the concrete case of averaging $n = 2$ or $n = 3$ values of g_1/F_1 over Q^2 as done in Section 6.1, we obtain the following expressions wherein $\mathbf{y} = (y_1, ..., y_n)$ is the vector of the n values of g_1/F_1 we want to average and F is the resulting average value:

n=2:

$$F = \frac{y_1(\mathcal{C}_{2,2} - \mathcal{C}_{1,2}) + y_2(\mathcal{C}_{1,1} - \mathcal{C}_{1,2})}{\mathcal{C}_{1,1} + \mathcal{C}_{2,2} - 2\,\mathcal{C}_{1,2}} \tag{A.5}$$

$$\sigma_F^2 = \frac{\mathcal{C}_{1,1}\,\mathcal{C}_{2,2} - \mathcal{C}_{1,2}^2}{\mathcal{C}_{1,1} + \mathcal{C}_{2,2} - 2\,\mathcal{C}_{1,2}} \tag{A.6}$$

where

$$\mathcal{C} = \begin{pmatrix} \mathcal{C}_{1,1} & \mathcal{C}_{1,2} \\ \mathcal{C}_{2,1} & \mathcal{C}_{2,2} \end{pmatrix} \tag{A.7}$$

is the 2×2 sub-covariance matrix belonging to the two values $\mathbf{y} = (y_1, y_2)^T$.

n=3: In the case $n = 3$ we obtain the expresssions

$$F = \frac{a_1 y_1 + a_2 y_2 + a_3 y_3}{a_1 + a_2 + a_3} \tag{A.8}$$

$$\sigma_F^2 = \frac{\det \mathcal{C}}{a_1 + a_2 + a_3} \tag{A.9}$$

with the coefficients a_1, a_2, a_3 being defined as

$$\begin{aligned} a_1 &= \mathcal{C}_{2,2}\,\mathcal{C}_{3,3} - \mathcal{C}_{2,3}^2 - \mathcal{C}_{1,2}\,\mathcal{C}_{3,3} + \mathcal{C}_{1,3}\,\mathcal{C}_{2,3} + \mathcal{C}_{1,2}\,\mathcal{C}_{2,3} - \mathcal{C}_{2,2}\,\mathcal{C}_{1,3} \\ a_2 &= \mathcal{C}_{1,1}\,\mathcal{C}_{3,3} - \mathcal{C}_{1,3}^2 - \mathcal{C}_{1,2}\,\mathcal{C}_{3,3} + \mathcal{C}_{1,3}\,\mathcal{C}_{2,3} + \mathcal{C}_{1,2}\,\mathcal{C}_{1,3} - \mathcal{C}_{1,1}\,\mathcal{C}_{2,3} \\ a_3 &= \mathcal{C}_{1,1}\,\mathcal{C}_{2,2} - \mathcal{C}_{1,2}^2 - \mathcal{C}_{1,3}\,\mathcal{C}_{2,2} + \mathcal{C}_{1,2}\,\mathcal{C}_{2,3} + \mathcal{C}_{1,2}\,\mathcal{C}_{1,3} - \mathcal{C}_{1,1}\,\mathcal{C}_{2,3} \end{aligned} \tag{A.10}$$

and the 3×3 sub-covariance matrix

$$\mathcal{C} = \begin{pmatrix} \mathcal{C}_{1,1} & \mathcal{C}_{1,2} & \mathcal{C}_{1,3} \\ \mathcal{C}_{2,1} & \mathcal{C}_{2,2} & \mathcal{C}_{2,3} \\ \mathcal{C}_{3,1} & \mathcal{C}_{3,2} & \mathcal{C}_{3,3} \end{pmatrix} \tag{A.11}$$

belonging to $\mathbf{y} = (y_1, y_2, y_3)^T$.

A.2 Covariance matrix of Q^2-averaged g_1/F_1 values

After averaging those x bins which were initially sub-divided into two or three Q^2 bins as described in Section A.1, 20 bins in x remain. The errors of the obtained g_1/F_1 values in these 20 bins are still correlated; to describe this the 20×20 covariance matrix $\mathcal{C}^{20\times20}_{g_1/F_1}$ needs to be calculated based on the 46×46 covariance matrix of the unfolded Born asymmetry $\mathcal{C}^{46\times46}_{A_{||}^{Born}}$ [CDNE+04a].

The elements (i,j) of the covariance matrix of g_1/F_1 in 46 bins are given by

$$\mathcal{C}^{46\times 46}_{g_1/F_1}(i,j) = \frac{\mathcal{C}^{46\times 46}_{A_{||}^{Born}}(i,j)}{D_i\, D_j\,(1+\gamma_i^2)\,(1+\gamma_j^2)}, \tag{A.12}$$

where the depolarization factor D (2.16) and the kinematic factor $\gamma = \sqrt{Q^2}/\nu$ are calculated at the average kinematics of bin i and bin j respectively. The elements (i,j) of the covariance matrix for g_1/F_1 in 20 bins are then given by

$$\mathcal{C}^{20\times 20}_{g_1/F_1}(i,j) = \frac{1}{(\sum_n a_{j,n})\,(\sum_l a_{i,l})} \sum_k \sum_m a_{i,k} a_{j,m}\;\; \mathcal{C}^{46\times 46}_{g_1/F_1}((i,k),(j,m)). \tag{A.13}$$

In this expression the indices $1 \le i,j \le 20$ denote the elements in the 20×20 matrix and the indices n,l,k,m run over the elements of the 46×46 matrix which contribute to element (i,j). The coefficients $a_{ij,nlkm}$ are functions of $\mathcal{C}^{46\times 46}_{g_1/F_1}$.

In case of two bins being averaged the indices n,l,k,m run over the elements of the corresponding 2×2 sub-matrix of $\mathcal{C}^{46\times 46}_{g_1/F_1}$ and the coefficients $a_{ij,nlkm}$ are given by:

$$a'_1 = \mathcal{C}_{2,2} - \mathcal{C}_{1,2} \qquad \text{and} \qquad a'_2 = \mathcal{C}_{1,1} - \mathcal{C}_{1,2} \tag{A.14}$$

(please compare Eqns. (A.5) – (A.7) and note that due to the symmetry of the covariance matrix $\mathcal{C}_{1,2} = \mathcal{C}_{2,1}$).

In case of three bins being averaged the coefficients $a_{ij,nlkm}$ are defined like a_1, a_2, a_3 in Eq. (A.10) calculated from the corresponding 3×3 sub-matrix (A.11).

A.3 Correlation matrix

The correlation between the uncertainties of distinct data poins can be expressed by a correlation matrix. The general relation between a covariance matrix $cov(i,j)$ and a correlation matrix $corr(i,j)$ is

$$cov(i,j) = \sigma(i)\,\sigma(j)\,corr(i,j) \tag{A.15}$$

$$= \sqrt{cov(i,i)}\,\sqrt{cov(j,j)}\,corr(i,j). \tag{A.16}$$

Therefore the correlation matrices as shown e.g. in Figs. 6.3 and 6.4 are given by

$$corr^{20\times 20}(i,j) = \frac{cov^{20\times 20}(i,j)}{\sqrt{cov^{20\times 20}(i,i)}\,\sqrt{cov^{20\times 20}(j,j)}}, \tag{A.17}$$

where the indices run in the range $1 \le i,j \le 20$.

Appendix B

Reconstruction inefficiencies

In the unfolding procedure described in Chapter 5, a correction for elastic and quasi-elastic background is applied. These background events are dominantly found in the region of small values of observed x and Q^2. Hard photons which are associated with elastic and quasi-elastic scattering processes have a high probability of hitting the detector frames surrounding the beam line in front of the dipole magnet and producing extensive electromagnetic showers that cause very high hit multiplicities in the tracking detectors [HERMES03]. The reconstruction of these events is often impossible because they are rejected by the tracking software due to their high hit multiplicity and hence are missing in the analyzed data set. If one didn't take into account the reconstruction efficiency in the background subtraction (i.e. wrongly assuming an efficiency of 100%), one would *overcorrect* by subtracting more elastic and quasi-elastic background events than are in fact present in the analyzed event sample.

Therefore the reconstruction efficiencies for elastic and quasi-elastic events were determined using a GEANT [BHHL78] based Monte Carlo in which all materials close to the beam pipe are implemented in detail. The minimum energy for secondary particles tracked through the detector was set to a value which makes sure that the effects of the full electromagnetic shower are simulated. The reconstruction efficiency for elastic and quasi-elastic events can be estimated by comparing the yields found in two Monte Carlo samples, the first one containing all the materials close to the beam pipe which cause showers, the second one not. The minimum of reconstruction efficiency is reached in the kinematic range $1 \times 10^{-2} < x < 3 \times 10^{-2}$ where it can be as low as 58% for a deuterium target and 82% for a proton target [CDNE$^+$04a] [HER05]. At higher values of x the efficiency rises to 100%.

To avoid an overcorrection when subtracting the background during unfolding, elastic and quasi-elastic events are weighted with their respective reconstruction efficiencies when the smearing matrices for the unfolding are computed based on Monte Carlo.

Appendix C

Binning

The binning used in this analysis divides the kinematic plane into **20 bins in x** . The first five x bins are not subdivided in Q^2, the next four x bins are subdivided into two bins in Q^2 with a common bin border at $Q^2 = 1$ GeV^2 and the remaining eleven x bins are subdivided into three Q^2 bins each. In total there are *46* xQ^2 *cells* (compare Fig. 4.4). All Q^2 values in the table below are given in units of GeV^2.

x bin	x_{min}	x_{max}	(xQ^2)	Q^2_{min}	Q^2_{max}	(xQ^2)	Q^2_{min}	Q^2_{max}	(xQ^2)	Q^2_{min}	Q^2_{max}
1	0.00200	0.00406	(*1*)	0.1	1.						
2	0.00406	0.00733	(*2*)	0.1	1.						
3	0.00733	0.01177	(*3*)	0.1	1.						
4	0.01177	0.01677	(*4*)	0.1	1.						
5	0.01677	0.02124	(*5*)	0.1	1.						
6	0.02124	0.02948	(*6*)	0.1	1.	(*7*)	1.	22.			
7	0.02948	0.03619	(*8*)	0.1	1.	(*9*)	1.	22.			
8	0.03619	0.04442	(*10*)	0.1	1.	(*11*)	1.	22.			
9	0.04442	0.05681	(*12*)	0.1	1.	(*13*)	1.	22.			
10	0.05681	0.07265	(*14*)	1.	1.505	(*15*)	1.505	2.265	(*16*)	2.265	22.
11	0.07265	0.09291	(*17*)	1.	1.620	(*18*)	1.620	2.623	(*19*)	2.623	22.
12	0.09291	0.11882	(*20*)	1.	1.740	(*21*)	1.740	3.026	(*22*)	3.026	22.
13	0.11882	0.15195	(*23*)	1.	1.882	(*24*)	1.882	3.491	(*25*)	3.491	22.
14	0.15195	0.19432	(*26*)	1.	2.061	(*27*)	2.061	4.032	(*28*)	4.032	22.
15	0.19432	0.24850	(*29*)	1.	2.237	(*30*)	2.237	4.614	(*31*)	4.614	22.
16	0.24850	0.31780	(*32*)	1.	2.657	(*33*)	2.657	5.491	(*34*)	5.491	22.
17	0.31780	0.40641	(*35*)	1.	3.305	(*36*)	3.305	6.645	(*37*)	6.645	22.
18	0.40641	0.51974	(*38*)	1.	4.093	(*39*)	4.093	7.967	(*40*)	7.967	22.
19	0.51974	0.66466	(*41*)	1.	5.043	(*42*)	5.043	9.458	(*43*)	9.458	22.
20	0.66466	0.90000	(*44*)	1.	7.655	(*45*)	7.655	12.528	(*46*)	12.528	22.

Appendix D

Tables

In the tables below, the values for $(g_1/F_1)(x)$ and $g_1(x)$ are listed together with their statistical and systematical uncertainties:

- Δ_{stat} is the statistical uncertainty; the correlations between the statistical uncertainties of different bins can be seen from the corresponding correlation matrices.
- Δ_{sys}^{exp} is the systematical uncertainty arising from experimental sources and includes the uncertainties on beam and target polarization, particle identification, contributions from the target spin-dependent tensor asymmetry and detector misalignment.
- Δ_{sys}^{par} is the systematical uncertainty due to the used parametrizations.
- Δ_{MC} is the uncertainty due to the finite statistics of the Monte Carlo data set used for the unfolding procedure.

D.1 Proton

x bin	$\langle x \rangle$	$\langle Q^2 \rangle$	g_1/F_1	Δ_{stat}	Δ_{sys}^{exp}	Δ_{sys}^{par}	Δ_{MC}	g_1	Δ_{stat}	Δ_{sys}^{exp}	Δ_{sys}^{par}	Δ_{MC}
1	0.0035	0.1631	0.1049	0.0930	0.0051	0.0063	0.0247	1.5617	1.3832	0.6990	0.0127	0.3668
2	0.0058	0.2605	0.0224	0.0265	0.0011	0.0039	0.0064	0.2602	0.3083	0.0617	0.0836	0.0745
3	0.0095	0.4085	0.0162	0.0188	0.0006	0.0036	0.0038	0.1381	0.1603	0.0170	0.0014	0.0322
4	0.0142	0.5750	0.0371	0.0189	0.0013	0.0039	0.0034	0.2395	0.1215	0.0161	0.0041	0.0216
5	0.0190	0.7253	0.0475	0.0229	0.0018	0.0071	0.0039	0.2479	0.1194	0.0090	0.0161	0.0201
6	0.0253	0.9096	0.0817	0.0170	0.0036	0.0017	0.0034	0.3441	0.0716	0.0066	0.0110	0.0143
7	0.0329	1.1462	0.1038	0.0229	0.0042	0.0048	0.0051	0.3607	0.0794	0.0036	0.0014	0.0177
8	0.0403	1.3159	0.0962	0.0225	0.0039	0.0070	0.0050	0.2848	0.0663	0.0027	0.0044	0.0148
9	0.0506	1.4896	0.1089	0.0197	0.0045	0.0053	0.0046	0.2678	0.0481	0.0035	0.0011	0.0113
10	0.0649	2.0227	0.1039	0.0193	0.0035	0.0039	0.0031	0.2136	0.0393	0.0038	0.0041	0.0063
11	0.0830	2.4679	0.1909	0.0196	0.0073	0.0074	0.0031	0.3211	0.0326	0.0079	0.0021	0.0051
12	0.1061	2.9904	0.1918	0.0207	0.0068	0.0066	0.0031	0.2629	0.0280	0.0075	0.0052	0.0042
13	0.1355	3.6140	0.2564	0.0221	0.0090	0.0065	0.0031	0.2858	0.0242	0.0080	0.0051	0.0034
14	0.1732	4.3030	0.3098	0.0249	0.0101	0.0096	0.0033	0.2754	0.0216	0.0062	0.0015	0.0028
15	0.2211	5.0819	0.3235	0.0288	0.0099	0.0129	0.0034	0.2206	0.0190	0.0028	0.0003	0.0022
16	0.2824	6.0060	0.3937	0.0345	0.0120	0.0082	0.0037	0.1939	0.0162	0.0008	0.0031	0.0017
17	0.3605	7.0366	0.4898	0.0443	0.0153	0.0135	0.0040	0.1587	0.0134	0.0004	0.0012	0.0012
18	0.4591	8.1467	0.6033	0.0626	0.0198	0.0193	0.0044	0.1113	0.0105	0.0012	0.0002	0.0007
19	0.5823	9.5712	0.5782	0.1089	0.0200	0.0199	0.0053	0.0470	0.0078	0.0010	0.0003	0.0004
20	0.7243	10.9888	0.9566	0.2127	0.0351	0.0279	0.0065	0.0228	0.0043	0.0007	0.0000	0.0001

Table D.1: g_1/F_1 and g_1 values in 20 x bins for the proton.

x bin	$\langle x\rangle$	$\langle Q^2\rangle$	g_1/F_1	Δ_{stat}	Δ_{sys}^{exp}	Δ_{sys}^{par}	Δ_{MC}	g_1	Δ_{stat}	Δ_{sys}^{exp}	Δ_{sys}^{par}	Δ_{MC}
6	0.0265	1.1163	0.1131	0.0353	0.0032	0.0020	0.0041	0.4533	0.1412	0.0060	0.0112	0.0164
7	0.0330	1.2401	0.0996	0.0271	0.0036	0.0045	0.0036	0.3451	0.0935	0.0033	0.0020	0.0126
8	0.0404	1.3616	0.0924	0.0239	0.0037	0.0072	0.0035	0.2732	0.0704	0.0029	0.0047	0.0104
9	0.0506	1.5157	0.1096	0.0203	0.0044	0.0052	0.0035	0.2694	0.0496	0.0032	0.0013	0.0084
10	0.0649	2.0227	0.1039	0.0193	0.0035	0.0039	0.0031	0.2136	0.0393	0.0038	0.0041	0.0063
11	0.0830	2.4679	0.1909	0.0196	0.0073	0.0074	0.0031	0.3211	0.0326	0.0079	0.0021	0.0051
12	0.1061	2.9904	0.1918	0.0207	0.0068	0.0066	0.0031	0.2629	0.0280	0.0075	0.0052	0.0042
13	0.1355	3.6140	0.2564	0.0221	0.0090	0.0065	0.0031	0.2858	0.0242	0.0080	0.0051	0.0034
14	0.1732	4.3030	0.3098	0.0249	0.0101	0.0096	0.0033	0.2754	0.0216	0.0062	0.0015	0.0028
15	0.2211	5.0819	0.3235	0.0288	0.0099	0.0129	0.0034	0.2206	0.0190	0.0028	0.0003	0.0022
16	0.2824	6.0060	0.3937	0.0345	0.0120	0.0082	0.0037	0.1939	0.0162	0.0008	0.0031	0.0017
17	0.3605	7.0366	0.4898	0.0443	0.0153	0.0135	0.0040	0.1587	0.0134	0.0004	0.0012	0.0012
18	0.4591	8.1467	0.6033	0.0626	0.0198	0.0193	0.0044	0.1113	0.0105	0.0012	0.0002	0.0007
19	0.5823	9.5712	0.5782	0.1089	0.0200	0.0199	0.0053	0.0470	0.0078	0.0010	0.0003	0.0004
20	0.7243	10.9888	0.9566	0.2127	0.0351	0.0279	0.0065	0.0228	0.0043	0.0007	0.0000	0.0001

Table D.2: g_1/F_1 and g_1 values in 15 x bins ($Q^2 > 1$ GeV^2) for the proton.

x bin	1	2	3	4	5	6	7	8	9	10
1	**1.000**	-0.145	0.007	-0.002	-0.001	-0.001	-0.001	-0.000	-0.001	0.000
2	-0.145	**1.000**	-0.159	0.005	-0.005	-0.003	-0.002	-0.002	-0.003	-0.000
3	0.007	-0.159	**1.000**	-0.196	0.000	-0.014	-0.006	-0.003	-0.008	-0.001
4	-0.002	0.005	-0.196	**1.000**	-0.230	-0.012	-0.014	-0.007	-0.022	-0.001
5	-0.001	-0.005	0.000	-0.230	**1.000**	-0.223	0.004	-0.012	-0.024	-0.002
6	-0.001	-0.003	-0.014	-0.012	-0.223	**1.000**	-0.247	0.002	-0.049	-0.004
7	-0.001	-0.002	-0.006	-0.014	0.004	-0.247	**1.000**	-0.289	-0.012	-0.008
8	-0.000	-0.002	-0.003	-0.007	-0.012	0.002	-0.289	**1.000**	-0.316	0.010
9	-0.001	-0.003	-0.008	-0.022	-0.024	-0.049	-0.012	-0.316	**1.000**	-0.192
10	0.000	-0.000	-0.001	-0.001	-0.002	-0.004	-0.008	0.010	-0.192	**1.000**
11	0.000	-0.000	-0.001	-0.001	-0.002	-0.003	-0.003	-0.008	0.006	-0.231
12	0.000	-0.000	-0.000	-0.001	-0.001	-0.002	-0.002	-0.002	-0.010	0.010
13	-0.000	-0.000	-0.000	-0.000	-0.001	-0.001	-0.001	-0.002	-0.003	-0.014
14	0.000	0.000	-0.000	-0.000	-0.000	-0.001	-0.001	-0.001	-0.002	-0.004
15	-0.000	-0.000	0.000	-0.000	-0.000	-0.000	-0.000	-0.001	-0.001	-0.003
16	0.000	0.000	-0.000	0.000	-0.000	-0.000	0.000	0.000	-0.001	-0.002
17	0.000	-0.000	0.000	-0.000	0.000	-0.000	0.000	-0.000	0.001	-0.001
18	-0.000	0.001	-0.000	0.000	-0.001	0.000	-0.000	-0.000	-0.001	-0.001
19	-0.000	-0.000	0.001	0.001	0.001	0.001	0.001	0.002	0.002	0.002
20	0.000	0.000	-0.001	-0.001	-0.001	-0.001	-0.001	-0.001	-0.002	-0.002

Table D.3: g_1 correlation matrix in 20 x bins for the proton (columns 1 - 10).

x bin	6	7	8	9	10	11	12	13	14	15
6	**1.000**	-0.160	0.009	-0.004	-0.004	-0.002	-0.002	-0.001	-0.001	-0.001
7	-0.160	**1.000**	-0.201	0.011	-0.010	-0.004	-0.003	-0.002	-0.001	-0.001
8	0.009	-0.201	**1.000**	-0.223	0.010	-0.009	-0.003	-0.002	-0.001	-0.001
9	-0.004	0.011	-0.223	**1.000**	-0.218	0.008	-0.011	-0.003	-0.003	-0.002
10	-0.004	-0.010	0.010	-0.218	**1.000**	-0.231	0.010	-0.014	-0.004	-0.003
11	-0.002	-0.004	-0.009	0.008	-0.231	**1.000**	-0.242	0.017	-0.014	-0.002
12	-0.002	-0.003	-0.003	-0.011	0.010	-0.242	**1.000**	-0.252	0.022	-0.014
13	-0.001	-0.002	-0.002	-0.003	-0.014	0.017	-0.252	**1.000**	-0.268	0.027
14	-0.001	-0.001	-0.001	-0.003	-0.004	-0.014	0.022	-0.268	**1.000**	-0.284
15	-0.001	-0.001	-0.001	-0.002	-0.003	-0.002	-0.014	0.027	-0.284	**1.000**
16	-0.001	-0.001	-0.000	-0.001	-0.002	-0.002	0.000	-0.016	0.034	-0.292
17	-0.001	-0.000	0.000	-0.001	-0.001	0.001	-0.001	0.003	-0.017	0.043
18	-0.000	-0.001	-0.001	-0.000	-0.001	-0.004	-0.004	-0.009	-0.002	-0.026
19	0.000	0.002	0.003	0.002	0.002	0.009	0.013	0.017	0.011	0.014
20	-0.000	-0.002	-0.003	-0.002	-0.002	-0.008	-0.011	-0.015	-0.011	-0.015

Table D.4: g_1 correlation matrix in 15 x bins with a cut of $Q^2 > 1$ GeV^2 for the proton.

11	12	13	14	15	16	17	18	19	20
0.000	0.000	-0.000	0.000	-0.000	0.000	0.000	-0.000	-0.000	0.000
-0.000	-0.000	-0.000	0.000	-0.000	0.000	-0.000	0.001	-0.000	0.000
-0.001	-0.000	-0.000	-0.000	0.000	-0.000	0.000	-0.000	0.001	-0.001
-0.001	-0.001	-0.000	-0.000	-0.000	0.000	-0.000	0.000	0.001	-0.001
-0.002	-0.001	-0.001	-0.000	-0.000	-0.000	0.000	-0.001	0.001	-0.001
-0.003	-0.002	-0.001	-0.001	-0.000	-0.000	-0.000	0.000	0.001	-0.001
-0.003	-0.002	-0.001	-0.001	-0.000	0.000	0.000	-0.000	0.001	-0.001
-0.008	-0.002	-0.002	-0.001	-0.001	0.000	-0.000	-0.000	0.002	-0.001
0.006	-0.010	-0.003	-0.002	-0.001	-0.001	0.001	-0.001	0.002	-0.002
-0.231	0.010	-0.014	-0.004	-0.003	-0.002	-0.001	-0.001	0.002	-0.002
1.000	-0.242	0.017	-0.014	-0.002	-0.002	0.001	-0.004	0.009	-0.008
-0.242	**1.000**	-0.252	0.022	-0.014	0.000	-0.001	-0.004	0.013	-0.011
0.017	-0.252	**1.000**	-0.268	0.027	-0.016	0.003	-0.009	0.017	-0.015
-0.014	0.022	-0.268	**1.000**	-0.284	0.034	-0.017	-0.002	0.011	-0.011
-0.002	-0.014	0.027	-0.284	**1.000**	-0.292	0.043	-0.026	0.014	-0.015
-0.002	0.000	-0.016	0.034	-0.292	**1.000**	-0.308	0.052	-0.011	-0.001
0.001	-0.001	0.003	-0.017	0.043	-0.308	**1.000**	-0.337	0.075	-0.045
-0.004	-0.004	-0.009	-0.002	-0.026	0.052	-0.337	**1.000**	-0.344	0.102
0.009	0.013	0.017	0.011	0.014	-0.011	0.075	-0.344	**1.000**	-0.391
-0.008	-0.011	-0.015	-0.011	-0.015	-0.001	-0.045	0.102	-0.391	**1.000**

continued: g_1 correlation matrix in 20 x bins for the proton.

16	17	18	19	20
-0.001	-0.001	-0.000	0.000	-0.000
-0.001	-0.000	-0.001	0.002	-0.002
-0.000	0.000	-0.001	0.003	-0.003
-0.001	-0.001	-0.000	0.002	-0.002
-0.002	-0.001	-0.001	0.002	-0.002
-0.002	0.001	-0.004	0.009	-0.008
0.000	-0.001	-0.004	0.013	-0.011
-0.016	0.003	-0.009	0.017	-0.015
0.034	-0.017	-0.002	0.011	-0.011
-0.292	0.043	-0.026	0.014	-0.015
1.000	-0.308	0.052	-0.011	-0.001
-0.308	**1.000**	-0.337	0.075	-0.045
0.052	-0.337	**1.000**	-0.344	0.102
-0.011	0.075	-0.344	**1.000**	-0.391
-0.001	-0.045	0.102	-0.391	**1.000**

continued: g_1 correlation matrix in 15 x bins for the proton.

D.2 Deuteron

x bin	$\langle x \rangle$	$\langle Q^2 \rangle$	g_1/F_1	Δ_{stat}	Δ_{sys}^{exp}	Δ_{sys}^{par}	Δ_{MC}	g_1	Δ_{stat}	Δ_{sys}^{exp}	Δ_{sys}^{par}	Δ_{MC}
1	0.0035	0.1627	0.0173	0.0377	0.0009	0.0007	0.0155	0.2541	0.5541	0.1209	0.0153	0.2282
2	0.0058	0.2595	0.0090	0.0116	0.0004	0.0026	0.0043	0.1033	0.1337	0.0252	0.0189	0.0494
3	0.0095	0.4086	-0.0030	0.0086	0.0001	0.0008	0.0028	-0.0248	0.0718	0.0028	0.0010	0.0238
4	0.0142	0.5764	-0.0014	0.0088	0.0001	0.0014	0.0026	-0.0089	0.0554	0.0006	0.0112	0.0167
5	0.0190	0.7285	-0.0028	0.0108	0.0001	0.0027	0.0032	-0.0145	0.0552	0.0006	0.0105	0.0163
6	0.0253	0.9155	0.0141	0.0082	0.0007	0.0001	0.0028	0.0577	0.0336	0.0013	0.0009	0.0116
7	0.0329	1.1532	-0.0087	0.0113	0.0004	0.0004	0.0043	-0.0292	0.0379	0.0003	0.0007	0.0145
8	0.0403	1.3236	0.0052	0.0113	0.0002	0.0015	0.0043	0.0147	0.0319	0.0003	0.0032	0.0122
9	0.0505	1.4945	0.0213	0.0100	0.0009	0.0013	0.0040	0.0501	0.0234	0.0010	0.0015	0.0094
10	0.0649	2.0389	0.0250	0.0099	0.0008	0.0040	0.0028	0.0487	0.0192	0.0010	0.0098	0.0053
11	0.0829	2.4877	0.0632	0.0103	0.0025	0.0024	0.0028	0.0997	0.0160	0.0022	0.0001	0.0043
12	0.1060	3.0205	0.0493	0.0110	0.0018	0.0017	0.0028	0.0625	0.0138	0.0012	0.0022	0.0035
13	0.1355	3.6443	0.0873	0.0122	0.0031	0.0037	0.0029	0.0884	0.0121	0.0016	0.0007	0.0028
14	0.1732	4.3688	0.1270	0.0139	0.0041	0.0071	0.0030	0.1003	0.0107	0.0015	0.0017	0.0023
15	0.2211	5.1784	0.1610	0.0165	0.0050	0.0049	0.0032	0.0948	0.0094	0.0009	0.0005	0.0018
16	0.2823	6.1401	0.1763	0.0205	0.0054	0.0082	0.0037	0.0722	0.0080	0.0003	0.0005	0.0014
17	0.3605	7.2162	0.3098	0.0271	0.0101	0.0064	0.0041	0.0796	0.0065	0.0006	0.0004	0.0010
18	0.4590	8.3693	0.3631	0.0402	0.0124	0.0065	0.0046	0.0500	0.0051	0.0009	0.0004	0.0006
19	0.5823	9.8574	0.4004	0.0727	0.0143	0.0081	0.0059	0.0225	0.0036	0.0007	0.0001	0.0003
20	0.7240	11.1583	0.7314	0.1519	0.0277	0.0184	0.0076	0.0113	0.0020	0.0007	0.0001	0.0001

Table D.5: g_1/F_1 and g_1 values in 20 x bins for the deuteron.

x bin	$\langle x \rangle$	$\langle Q^2 \rangle$	g_1/F_1	Δ_{stat}	Δ_{sys}^{exp}	Δ_{sys}^{par}	Δ_{MC}	g_1	Δ_{stat}	Δ_{sys}^{exp}	Δ_{sys}^{par}	Δ_{MC}
6	0.0265	1.1177	0.0281	0.0166	0.0008	0.0002	0.0035	0.1096	0.0647	0.0033	0.0008	0.0136
7	0.0330	1.2441	-0.0122	0.0133	0.0005	0.0003	0.0031	-0.0409	0.0443	0.0011	0.0008	0.0105
8	0.0403	1.3666	0.0042	0.0119	0.0002	0.0016	0.0031	0.0120	0.0338	0.0003	0.0031	0.0089
9	0.0506	1.5200	0.0226	0.0103	0.0009	0.0012	0.0031	0.0532	0.0241	0.0010	0.0017	0.0072
10	0.0649	2.0389	0.0250	0.0099	0.0008	0.0040	0.0028	0.0487	0.0192	0.0010	0.0098	0.0053
11	0.0829	2.4877	0.0632	0.0103	0.0025	0.0024	0.0028	0.0997	0.0160	0.0022	0.0001	0.0043
12	0.1060	3.0205	0.0493	0.0110	0.0018	0.0017	0.0028	0.0625	0.0138	0.0012	0.0022	0.0035
13	0.1355	3.6443	0.0873	0.0122	0.0031	0.0037	0.0029	0.0884	0.0121	0.0016	0.0007	0.0028
14	0.1732	4.3688	0.1270	0.0139	0.0041	0.0071	0.0030	0.1003	0.0107	0.0015	0.0017	0.0023
15	0.2211	5.1784	0.1610	0.0165	0.0050	0.0049	0.0032	0.0948	0.0094	0.0009	0.0005	0.0018
16	0.2823	6.1401	0.1763	0.0205	0.0054	0.0082	0.0037	0.0722	0.0080	0.0003	0.0005	0.0014
17	0.3605	7.2162	0.3098	0.0271	0.0101	0.0064	0.0041	0.0796	0.0065	0.0006	0.0004	0.0010
18	0.4590	8.3693	0.3631	0.0402	0.0124	0.0065	0.0046	0.0500	0.0051	0.0009	0.0004	0.0006
19	0.5823	9.8574	0.4004	0.0727	0.0143	0.0081	0.0059	0.0225	0.0036	0.0007	0.0001	0.0003
20	0.7240	11.1583	0.7314	0.1519	0.0277	0.0184	0.0076	0.0113	0.0020	0.0007	0.0001	0.0001

Table D.6: g_1/F_1 and g_1 values in 15 x bins ($Q^2 > 1$ GeV^2) for the deuteron.

x bin	1	2	3	4	5	6	7	8	9	10
1	**1.000**	-0.147	0.009	-0.002	-0.001	-0.000	-0.000	-0.000	-0.001	-0.000
2	-0.147	**1.000**	-0.150	0.007	-0.004	-0.002	-0.002	-0.001	-0.003	-0.000
3	0.009	-0.150	**1.000**	-0.187	0.003	-0.013	-0.005	-0.003	-0.007	-0.001
4	-0.002	0.007	-0.187	**1.000**	-0.225	-0.004	-0.014	-0.005	-0.022	-0.001
5	-0.001	-0.004	0.003	-0.225	**1.000**	-0.225	0.009	-0.010	-0.024	-0.001
6	-0.000	-0.002	-0.013	-0.004	-0.225	**1.000**	-0.249	0.016	-0.049	-0.002
7	-0.000	-0.002	-0.005	-0.014	0.009	-0.249	**1.000**	-0.301	0.005	-0.006
8	-0.000	-0.001	-0.003	-0.005	-0.010	0.016	-0.301	**1.000**	-0.332	0.018
9	-0.001	-0.003	-0.007	-0.022	-0.024	-0.049	0.005	-0.332	**1.000**	-0.198
10	-0.000	-0.000	-0.001	-0.001	-0.001	-0.002	-0.006	0.018	-0.198	**1.000**
11	0.000	-0.000	-0.000	-0.001	-0.001	-0.002	-0.002	-0.007	0.016	-0.240
12	0.000	-0.000	-0.000	-0.000	-0.001	-0.001	-0.001	-0.001	-0.009	0.021
13	-0.000	0.000	0.000	-0.000	-0.000	-0.001	-0.001	-0.001	-0.002	-0.012
14	0.000	-0.000	-0.000	-0.000	0.000	-0.000	-0.001	-0.001	-0.002	-0.002
15	0.000	0.000	0.000	-0.000	-0.001	-0.000	0.000	-0.000	-0.001	-0.002
16	-0.000	-0.000	-0.000	0.000	0.000	-0.000	-0.001	-0.000	-0.000	-0.001
17	0.000	0.000	0.000	0.000	-0.000	0.000	0.000	0.001	-0.000	-0.001
18	-0.000	0.000	-0.000	0.000	-0.000	-0.000	-0.000	-0.001	0.000	-0.001
19	0.000	-0.000	0.000	0.001	0.001	0.001	0.000	0.002	0.001	0.002
20	-0.000	0.000	-0.000	-0.000	-0.001	-0.001	-0.000	-0.001	-0.001	-0.002

Table D.7: g_1 correlation matrix in 20 x bins for the deuteron (columns 1 - 10).

x bin	6	7	8	9	10	11	12	13	14	15
6	**1.000**	-0.175	0.018	-0.004	-0.002	-0.002	-0.001	-0.001	-0.001	-0.001
7	-0.175	**1.000**	-0.215	0.021	-0.009	-0.003	-0.002	-0.001	-0.001	-0.001
8	0.018	-0.215	**1.000**	-0.233	0.019	-0.008	-0.002	-0.002	-0.001	-0.001
9	-0.004	0.021	-0.233	**1.000**	-0.224	0.018	-0.010	-0.002	-0.002	-0.001
10	-0.002	-0.009	0.019	-0.224	**1.000**	-0.240	0.021	-0.012	-0.002	-0.002
11	-0.002	-0.003	-0.008	0.018	-0.240	**1.000**	-0.252	0.029	-0.013	-0.001
12	-0.001	-0.002	-0.002	-0.010	0.021	-0.252	**1.000**	-0.267	0.035	-0.013
13	-0.001	-0.001	-0.002	-0.002	-0.012	0.029	-0.267	**1.000**	-0.282	0.041
14	-0.001	-0.001	-0.001	-0.002	-0.002	-0.013	0.035	-0.282	**1.000**	-0.300
15	-0.001	-0.001	-0.001	-0.001	-0.002	-0.001	-0.013	0.041	-0.300	**1.000**
16	-0.001	-0.000	-0.000	-0.001	-0.001	-0.001	0.001	-0.016	0.049	-0.310
17	-0.000	-0.000	0.000	-0.000	-0.001	0.001	0.000	0.005	-0.016	0.058
18	-0.000	-0.000	-0.001	-0.000	-0.001	-0.003	-0.005	-0.009	-0.001	-0.026
19	0.001	0.001	0.002	0.002	0.002	0.008	0.013	0.014	0.010	0.012
20	-0.001	-0.001	-0.002	-0.001	-0.002	-0.006	-0.010	-0.012	-0.008	-0.012

Table D.8: g_1 correlation matrix in 15 x bins with a cut of $Q^2 > 1$ GeV^2 for the deuteron.

11	12	13	14	15	16	17	18	19	20
0.000	0.000	-0.000	0.000	0.000	-0.000	0.000	-0.000	0.000	-0.000
-0.000	-0.000	0.000	-0.000	0.000	-0.000	0.000	0.000	-0.000	0.000
-0.000	-0.000	0.000	-0.000	0.000	-0.000	0.000	-0.000	0.000	-0.000
-0.001	-0.000	-0.000	-0.000	-0.000	0.000	0.000	0.000	0.001	-0.000
-0.001	-0.001	-0.000	0.000	-0.001	0.000	-0.000	-0.000	0.001	-0.001
-0.002	-0.001	-0.001	-0.000	-0.000	-0.000	0.000	-0.000	0.001	-0.001
-0.002	-0.001	-0.001	-0.001	0.000	-0.001	0.000	-0.000	0.000	-0.000
-0.007	-0.001	-0.001	-0.001	-0.000	-0.000	0.001	-0.001	0.002	-0.001
0.016	-0.009	-0.002	-0.002	-0.001	-0.000	-0.000	0.000	0.001	-0.001
-0.240	0.021	-0.012	-0.002	-0.002	-0.001	-0.001	-0.001	0.002	-0.002
1.000	-0.252	0.029	-0.013	-0.001	-0.001	0.001	-0.003	0.008	-0.006
-0.252	**1.000**	-0.267	0.035	-0.013	0.001	0.000	-0.005	0.013	-0.010
0.029	-0.267	**1.000**	-0.282	0.041	-0.016	0.005	-0.009	0.014	-0.012
-0.013	0.035	-0.282	**1.000**	-0.300	0.049	-0.016	-0.001	0.010	-0.008
-0.001	-0.013	0.041	-0.300	**1.000**	-0.310	0.058	-0.026	0.012	-0.012
-0.001	0.001	-0.016	0.049	-0.310	**1.000**	-0.326	0.067	-0.011	0.003
0.001	0.000	0.005	-0.016	0.058	-0.326	**1.000**	-0.361	0.090	-0.052
-0.003	-0.005	-0.009	-0.001	-0.026	0.067	-0.361	**1.000**	-0.375	0.132
0.008	0.013	0.014	0.010	0.012	-0.011	0.090	-0.375	**1.000**	-0.425
-0.006	-0.010	-0.012	-0.008	-0.012	0.003	-0.052	0.132	-0.425	**1.000**

continued: g_1 correlation matrix in 20 x bins for the deuteron.

16	17	18	19	20
-0.001	-0.000	-0.000	0.001	-0.001
-0.000	-0.000	-0.000	0.001	-0.001
-0.000	0.000	-0.001	0.002	-0.002
-0.001	-0.000	-0.000	0.002	-0.001
-0.001	-0.001	-0.001	0.002	-0.002
-0.001	0.001	-0.003	0.008	-0.006
0.001	0.000	-0.005	0.013	-0.010
-0.016	0.005	-0.009	0.014	-0.012
0.049	-0.016	-0.001	0.010	-0.008
-0.310	0.058	-0.026	0.012	-0.012
1.000	-0.326	0.067	-0.011	0.003
-0.326	**1.000**	-0.361	0.090	-0.052
0.067	-0.361	**1.000**	-0.375	0.132
-0.011	0.090	-0.375	**1.000**	-0.425
0.003	-0.052	0.132	-0.425	**1.000**

continued: g_1 correlation matrix in 15 x bins for the deuteron.

D.3 Neutron

x bin	$\langle x \rangle$	$\langle Q^2 \rangle$	g_1	Δ_{stat}	Δ_{sys}^{exp}	Δ_{sys}^{par}	$\Delta_{sys}^{\omega_D}$	Δ_{MC}
1	0.0035	0.1629	-1.0124	1.8304	0.4378	0.0354	0.0089	0.6148
2	0.0058	0.2600	-0.0368	0.4228	0.0086	0.0931	0.0036	0.1302
3	0.0095	0.4085	-0.1917	0.2233	0.0256	0.0026	0.0009	0.0607
4	0.0142	0.5757	-0.2588	0.1708	0.0198	0.0245	0.0003	0.0420
5	0.0190	0.7269	-0.2791	0.1690	0.0133	0.0278	0.0005	0.0406
6	0.0253	0.9125	-0.2192	0.1047	0.0073	0.0111	0.0020	0.0289
7	0.0329	1.1497	-0.4238	0.1236	0.0107	0.0021	0.0010	0.0360
8	0.0403	1.3197	-0.2531	0.1039	0.0052	0.0082	0.0005	0.0302
9	0.0506	1.4921	-0.1594	0.0751	0.0030	0.0034	0.0018	0.0234
10	0.0649	2.0308	-0.1082	0.0576	0.0026	0.0216	0.0017	0.0131
11	0.0829	2.4778	-0.1055	0.0481	0.0049	0.0021	0.0035	0.0106
12	0.1060	3.0055	-0.1278	0.0415	0.0059	0.0070	0.0022	0.0087
13	0.1355	3.6291	-0.0947	0.0364	0.0057	0.0053	0.0031	0.0069
14	0.1732	4.3359	-0.0586	0.0325	0.0046	0.0040	0.0035	0.0057
15	0.2211	5.1302	-0.0157	0.0288	0.0035	0.0011	0.0033	0.0045
16	0.2823	6.0730	-0.0378	0.0249	0.0026	0.0033	0.0025	0.0035
17	0.3605	7.1264	0.0134	0.0208	0.0029	0.0015	0.0028	0.0025
18	0.4590	8.2580	-0.0032	0.0166	0.0035	0.0001	0.0018	0.0014
19	0.5823	9.7143	0.0017	0.0125	0.0027	0.0000	0.0008	0.0001
20	0.7241	11.0735	0.0017	0.0072	0.0022	0.0000	0.0004	0.0000

Table D.9: g_1 values in 20 x bins for the neutron.

x bin	1	2	3	4	5	6	7	8	9	10
1	**1.000**	-0.145	0.008	-0.002	-0.001	-0.001	-0.000	-0.000	-0.001	-0.000
2	-0.145	**1.000**	-0.155	0.006	-0.005	-0.003	-0.002	-0.001	-0.003	-0.000
3	0.008	-0.155	**1.000**	-0.192	0.002	-0.013	-0.006	-0.003	-0.008	-0.001
4	-0.002	0.006	-0.192	**1.000**	-0.228	-0.008	-0.014	-0.006	-0.022	-0.001
5	-0.001	-0.005	0.002	-0.228	**1.000**	-0.224	0.006	-0.011	-0.024	-0.001
6	-0.001	-0.003	-0.013	-0.008	-0.224	**1.000**	-0.248	0.009	-0.049	-0.003
7	-0.000	-0.002	-0.006	-0.014	0.006	-0.248	**1.000**	-0.295	-0.003	-0.007
8	-0.000	-0.001	-0.003	-0.006	-0.011	0.009	-0.295	**1.000**	-0.324	0.014
9	-0.001	-0.003	-0.008	-0.022	-0.024	-0.049	-0.003	-0.324	**1.000**	-0.195
10	-0.000	-0.000	-0.001	-0.001	-0.001	-0.003	-0.007	0.014	-0.195	**1.000**
11	0.000	-0.000	-0.000	-0.001	-0.001	-0.003	-0.002	-0.008	0.011	-0.236
12	0.000	-0.000	-0.000	-0.000	-0.001	-0.001	-0.002	-0.002	-0.009	0.016
13	-0.000	0.000	-0.000	-0.000	-0.001	-0.001	-0.001	-0.002	-0.002	-0.013
14	0.000	-0.000	-0.000	-0.000	-0.000	-0.001	-0.001	-0.001	-0.002	-0.003
15	0.000	0.000	0.000	-0.000	-0.000	-0.000	-0.000	-0.001	-0.001	-0.003
16	-0.000	0.000	-0.000	0.000	0.000	-0.000	-0.000	-0.000	-0.001	-0.001
17	0.000	-0.000	0.000	-0.000	0.000	0.000	0.000	0.000	0.000	-0.001
18	-0.000	0.000	-0.000	0.000	-0.000	0.000	-0.000	-0.001	-0.001	-0.001
19	0.000	-0.000	0.001	0.001	0.001	0.001	0.001	0.002	0.001	0.002
20	-0.000	0.000	-0.000	-0.001	-0.001	-0.001	-0.001	-0.001	-0.001	-0.002

Table D.10: g_1 correlation matrix in 20 x bins for the neutron (columns 1 - 10).

11	12	13	14	15	16	17	18	19	20
0.000	0.000	-0.000	0.000	0.000	-0.000	0.000	-0.000	0.000	-0.000
-0.000	-0.000	0.000	-0.000	0.000	0.000	-0.000	0.000	-0.000	0.000
-0.000	-0.000	-0.000	-0.000	0.000	-0.000	0.000	-0.000	0.001	-0.000
-0.001	-0.000	-0.000	-0.000	-0.000	0.000	-0.000	0.000	0.001	-0.001
-0.001	-0.001	-0.001	-0.000	-0.000	0.000	0.000	-0.000	0.001	-0.001
-0.003	-0.001	-0.001	-0.001	-0.000	-0.000	0.000	0.000	0.001	-0.001
-0.002	-0.002	-0.001	-0.001	-0.000	-0.000	0.000	-0.000	0.001	-0.001
-0.008	-0.002	-0.002	-0.001	-0.001	-0.000	0.000	-0.001	0.002	-0.001
0.011	-0.009	-0.002	-0.002	-0.001	-0.001	0.000	-0.001	0.001	-0.001
-0.236	0.016	-0.013	-0.003	-0.003	-0.001	-0.001	-0.001	0.002	-0.002
1.000	-0.248	0.024	-0.013	-0.001	-0.002	0.001	-0.004	0.009	-0.007
-0.248	**1.000**	-0.260	0.029	-0.014	0.001	-0.001	-0.004	0.013	-0.011
0.024	-0.260	**1.000**	-0.276	0.035	-0.016	0.004	-0.009	0.016	-0.014
-0.013	0.029	-0.276	**1.000**	-0.292	0.042	-0.017	-0.002	0.010	-0.010
-0.001	-0.014	0.035	-0.292	**1.000**	-0.302	0.051	-0.026	0.013	-0.014
-0.002	0.001	-0.016	0.042	-0.302	**1.000**	-0.317	0.060	-0.011	0.001
0.001	-0.001	0.004	-0.017	0.051	-0.317	**1.000**	-0.350	0.083	-0.049
-0.004	-0.004	-0.009	-0.002	-0.026	0.060	-0.350	**1.000**	-0.359	0.118
0.009	0.013	0.016	0.010	0.013	-0.011	0.083	-0.359	**1.000**	-0.408
-0.007	-0.011	-0.014	-0.010	-0.014	0.001	-0.049	0.118	-0.408	**1.000**

continued: g_1 correlation matrix in 20 x bins for the neutron (columns 11 - 20).

Bibliography

[A$^+$98] K. Ackerstaff et al., *The HERMES Spectrometer*, Nucl. Instr. and Meth. **A417**, 230–265 (1998), hep-ex/9806008, DESY-98-057.

[A$^+$02] N. Akopov et al., *The HERMES dual-radiator ring imaging Cerenkov detector*, Nucl. Instrum. Meth. **A479**, 511–530 (2002), physics/0104033.

[AB69] S. L. Adler and W. A. Bardeen, *Absence of higher order corrections in the anomalous axial vector divergence equation*, Phys. Rev. **182**, 1517–1536 (1969).

[ABR98] I. Akushevich, H. Boettcher and D. Ryckbosch, (1998), hep-ph/9906408.

[Adl69] S. L. Adler, *Axial vector vertex in spinor electrodynamics*, Phys. Rev. **177**, 2426–2438 (1969).

[AEL95] M. Anselmino, A. Efremov and E. Leader, *The theory and phenomenology of polarized deep inelastic scattering*, Phys. Rept. **261**, 1–124 (1995), hep-ph/9501369.

[AL97] H. Abramowicz and A. Levy, *The ALLM parameterization of $\sigma_{tot}(\gamma^* p)$: an update*, (1997), hep-ph/9712415.

[AP77] G. Altarelli and G. Parisi, *Asymptotic freedom in parton language*, Nucl. Phys. **B126**, 298–318 (1977).

[AR88] G. Altarelli and G. G. Ross, *The anomalous gluon contribution to polarized leptoproduction*, Phys. Lett. **B212**, 391–396 (1988).

[Asc04] E.-C. Aschenauer, private communication, 2004.

[B$^+$93] D. P. Barber et al., *The HERA polarimeter and the first observation of electron spin polarization at HERA*, Nucl. Instrum. Meth. **A329**, 79–111 (1993).

[B+02] M. Beckmann et al., *The longitudinal polarimeter at HERA*, Nucl. Instrum. Meth. **A479**, 334–348 (2002), physics/0009047.

[Bec03] M. Beckmann, Target polarization values and their uncertainties used by the Δq analysis group for the 1996 to 2000 running periods, HERMES Internal Note 03-005, March 2003.

[BFR96] R. D. Ball, S. Forte and G. Ridolfi, *A Next-to-Leading Determination of the Singlet Axial Charge and the Polarized Gluon Content of the Nucleon*, Phys. Lett. **B378**, 255–266 (1996), hep-ph/9510449.

[BG79] W. W. Buck and F. Gross, *A family of relativistic deuteron wave functions*, Phys. Rev. **D20**, 2361–2379 (1979).

[BHHL78] R. Brun, R. Hagelberg, M. Hansroul and J. Lassalle, (1978), CERN-DD-78-2-REV.

[Bjo70] J. D. Bjorken, *Inelastic scattering of polarized leptons from polarized nucleons*, Phys. Rev. **D1**, 1376–1379 (1970).

[Boe05] H. Boettcher, private communication, 2005.

[BP69] J. D. Bjorken and E. A. Paschos, *Inelastic electron-proton and γ-proton scattering and the structure of the nucleon*, Phys. Rev. **185**, 1975–1982 (1969).

[Bru04] A. Bruell, private communication, 2004.

[CCM88] R. D. Carlitz, J. C. Collins and A. H. Mueller, *The role of the axial anomaly in measuring spin dependent parton distributions*, Phys. Lett. **B214**, 229–236 (1988).

[CdASPS93] C. Ciofi degli Atti, S. Scopetta, E. Pace and G. Salme, *Nuclear effects in deep inelastic scattering of polarized electrons off polarized ^{3}He and the neutron spin structure functions*, Phys. Rev. **C48**, 968–972 (1993), nucl-th/9303016.

[CDNE+04a] M. Contalbrigo, L. De Nardo, M. Ehrenfried, D. Reggiani and C. Riedl, Measurement of the Polarized Structure Functions g_1^p and g_1^d (HERMES release report), September 2004.

[CDNE+04b] M. Contalbrigo, L. De Nardo, M. Ehrenfried, D. Reggiani and C. Riedl, Moments of the structure function g_1 of the proton and the deuteron over the measured x range (HERMES release report), December 2004.

[Che96] H.-Y. Cheng, *Status of the proton spin problem*, Int. J. Mod. Phys. **A11**, 5109–5182 (1996), hep-ph/9607254.

[COMPASS05a] E. S. Ageev et al. (COMPASS Collaboration), *Measurement of the spin structure of the deuteron in the DIS region*, Phys. Lett. **B612**, 154–164 (2005), hep-ex/0501073.

[COMPASS05b] A. Mielech (COMPASS Collaboration), *Determination of the gluon polarisation in COMPASS experiment at CERN*, Nucl. Phys. **A752**, 191–195 (2005).

[DN] L. De Nardo, *Measurement of the structure function g_1^d at HERMES and extraction of polarized parton distributions (PhD thesis)*, UMI-NQ-81178.

[Due] M. Dueren, *The HERMES Experiment: From the Design to the First Results (Habilitation thesis, University of Erlangen-Nuernberg)*, DESY-HERMES 95-02.

[E14296] P. L. Anthony et al. (E142 Collaboration), *Deep inelastic scattering of polarized electrons by polarized ^{3}He and the study of the neutron spin structure*, Phys. Rev. **D54**, 6620–6650 (1996), hep-ex/9610007.

[E14396] K. Abe et al. (E143 Collaboration), *Measurement of the proton and deuteron spin structure function g_2 and asymmetry A_2*, Phys. Rev. Lett. **76**, 587–591 (1996), hep-ex/9511013.

[E14398] K. Abe et al. (E143 Collaboration), *Measurements of the proton and deuteron spin structure functions g_1 and g_2*, Phys. Rev. **D58**, 112003 (1998), hep-ph/9802357.

[E15497a] K. Abe et al. (E154 Collaboration), *Measurement of the neutron spin structure function g_2^n and asymmetry A_2^n*, Phys. Lett. **B404**, 377–382 (1997), hep-ex/9705017.

[E15497b] K. Abe et al. (E154 Collaboration), *Precision determination of the neutron spin structure function g_1^n*, Phys. Rev. Lett. **79**, 26–30 (1997), hep-ex/9705012.

[E155] P. M. King (E155 Collaboration), *Spin structure functions of the proton and deuteron from SLAC experiments E155 and E155X*, Presented at Workshop on Testing QCD through Spin Observables in Nuclear Targets, Charlottesville, Virginia, 18-20 Apr 2002.

[E15599a] P. L. Anthony et al. (E155 Collaboration), *Measurement of the deuteron spin structure function $g_1^d(x)$ for 1 (GeV/c)^2 < Q^2 < 40 (GeV/c)^2*, Phys. Lett. **B463**, 339–345 (1999), hep-ex/9904002.

[E15599b] P. L. Anthony et al. (E155 Collaboration), *Measurement of the proton and deuteron spin structure functions g_2 and asymmetry A_2*, Phys. Lett. **B458**, 529–535 (1999), hep-ex/9901006.

[E15500] P. L. Anthony et al. (E155 Collaboration), *Measurements of the Q^2 dependence of the proton and neutron spin structure functions g_1^p and g_1^n*, Phys. Lett. **B493**, 19–28 (2000), hep-ph/0007248.

[E15503] P. L. Anthony et al. (E155 Collaboration), *Precision measurement of the proton and deuteron spin structure functions g_2 and asymmetries A_2*, Phys. Lett. **B553**, 18–24 (2003), hep-ex/0204028.

[EJ74] J. R. Ellis and R. L. Jaffe, *A sum rule for deep inelastic electroproduction from polarized protons*, Phys. Rev. **D9**, 1444–1446 (1974).

[Fey72] R. P. Feynman, *Photon-Hadron Interactions*, W. A. Benjamin, New York, 1972.

[FGP$^+$90] J. L. Friar, B. F. Gibson, G. L. Payne, A. M. Bernstein and T. E. Chupp, *Neutron polarization in polarized He-3 targets*, Phys. Rev. **C42**, 2310–2314 (1990).

[FJ01] B. W. Filippone and X.-D. Ji, *The spin structure of the nucleon*, Adv. Nucl. Phys. **26**, 1–83 (2001), hep-ph/0101224.

[Gae01] Y. Gaerber, *Measurement of the proton spin structure function g_1 down to smallest possible Bjorken-x with the HERMES experiment. (PhD thesis, in German)*, (2001), DESY-THESIS-2001-042.

[GL72] V. N. Gribov and L. N. Lipatov, *Deep inelastic e p scattering in perturbation theory*, Sov. J. Nucl. Phys. **15**, 438–450 (1972).

[HER05] HERMES, inclusive analysis group, internal communication, 2005.

[HERMES97] K. Ackerstaff et al. (HERMES Collaboration), *Measurement of the neutron spin structure function g_1^n with a polarized ^3He internal target*, Phys. Lett. **B404**, 383–389 (1997), hep-ex/9703005.

[HERMES00] A. Airapetian et al. (HERMES Collaboration), *Measurement of the spin asymmetry in the photoproduction of pairs of high p_T hadrons at HERMES*, Phys. Rev. Lett. **84**, 2584–2588 (2000), hep-ex/9907020.

[HERMES03] A. Airapetian et al. (HERMES Collaboration), *Erratum to: Nuclear effects on $R = \sigma_L/\sigma_T$ in deep inelastic scattering*, Phys. Lett. **B567**, 339–346 (2003).

[HERMES05a] A. Airapetian et al. (HERMES Collaboration), *Precision measurements of the spin-dependent structure functions g_1 of the proton and the deuteron at HERMES (publication in preparation)*, 2005.

[HERMES05b] A. Airapetian et al. (HERMES Collaboration), *Quark helicity distributions in the nucleon for up, down, and strange quarks from semi-inclusive deep-inelastic scattering*, Phys. Rev D **71**, 012003 (2005), hep-ex/0407032, DESY 04-107.

[HERMES05c] A. Airapetian et al. (HERMES Collaboration), *Single-spin asymmetries in semi-inclusive deep-inelastic scattering on a transversely polarized hydrogen target*, Phys. Rev. Lett. **94**, 012002 (2005), hep-ex/0408013.

[Jaf90] R. L. Jaffe, *g_2: The nucleon's other spin dependent structure function*, Comments Nucl. Part. Phys. **19**, 239–251 (1990).

[JM90] R. L. Jaffe and A. Manohar, *The g_1 problem: fact and fantasy on the spin of the proton*, Nucl. Phys. **B337**, 509–546 (1990).

[L+80] M. Lacombe et al., *Parametrization of the Paris N–N potential*, Phys. Rev. **C21**, 861–873 (1980).

[L+81] M. Lacombe et al., *Parametrization of the deuteron wave function of the Paris n-n potential*, Phys. Lett. **B101**, 139–140 (1981).

[Lip75] L. N. Lipatov, *The parton model and perturbation theory*, Sov. J. Nucl. Phys. **20**, 94–102 (1975).

[LR00] B. Lampe and E. Reya, *Spin physics and polarized structure functions*, Phys. Rept. **332**, 1–163 (2000), hep-ph/9810270.

[LSS98] E. Leader, A. V. Sidorov and D. B. Stamenov, *NLO QCD analysis of polarized deep inelastic scattering*, Int. J. Mod. Phys. **A13**, 5573–5592 (1998), hep-ph/9708335.

[LV91] S. A. Larin and J. A. M. Vermaseren, *The α_s^3 corrections to the Bjorken sum rule for polarized electroproduction and to the Gross-Llewellyn Smith sum rule*, Phys. Lett. **B259**, 345–352 (1991).

[MHE87] R. Machleidt, K. Holinde and C. Elster, *The Bonn Meson Exchange Model for the Nucleon Nucleon Interaction*, Phys. Rept. **149**, 1–89 (1987).

[Mil02] A. Miller, Applying radiative corrections to polarisation asymmetries for deeply inelastic scattering (unpublished), 2002.

[Mil04] A. Miller, private communication, 2004.

[Muon88] J. Ashman et al. (European Muon Collaboration), *A measurement of the spin asymmetry and determination of the structure function g_1 in deep inelastic muon proton scattering*, Phys. Lett. **B206**, 364–370 (1988).

[Muon89] J. Ashman et al. (European Muon Collaboration), *An investigation of the spin structure of the proton in deep inelastic scattering of polarized muons on polarized protons*, Nucl. Phys. **B328**, 1–35 (1989).

[Muon92] P. Amaudruz et al. (New Muon Collaboration), *The ratio F_2^n/F_2^p in deep inelastic muon scattering*, Nucl. Phys. **B371**, 3–31 (1992).

[Muon94] D. Adams et al. (Spin Muon Collaboration), *Spin asymmetry in muon proton deep inelastic scattering on a transversely-polarized target*, Phys. Lett. **B336**, 125–130 (1994), hep-ex/9408001.

[Muon96] B. Adeva et al. (Spin Muon Collaboration), *Polarisation of valence and non-strange sea quarks in the nucleon from semi-inclusive spin asymmetries*, Phys. Lett. **B369**, 93–100 (1996).

[Muon98] B. Adeva et al. (Spin Muon Collaboration), *Spin asymmetries A_1 and structure functions g_1 of the proton and the deuteron from polarized high energy muon scattering*, Phys. Rev. **D58**, 112001 (1998).

[Muon99] B. Adeva et al. (Spin Muon Collaboration), *Spin asymmetries A_1 of the proton and the deuteron in the low x and low Q^2 region from polarized high energy muon scattering*, Phys. Rev. **D60**, 072004 (1999).

[Muon00] B. Adeva et al. (Spin Muon Collaboration), *Erratum: Spin asymmetries A_1 of the proton and the deuteron in the low x and low Q^2 region from polarized high energy muon scattering*, Phys. Rev. **D62**, 079902 (2000).

[PHENIX98] N. Saito et al. (PHENIX Collaboration), *Spin physics with the PHENIX detector system*, Nucl. Phys. **A638**, 575–578 (1998), hep-ex/9805003.

[Rie05] C. Riedl, *The first measurement of the tensor structure function b_1^d of the deuteron with the HERMES experiment (PhD thesis, University of Erlangen-Nuernberg)*, 2005.

[Rit02] K. Rith, *Spin asymmetries in deep-inelastic electron nucleon scattering: Selected HERMES results*, Prog. Part. Nucl. Phys. **49**, 245–324 (2002).

[ST64] A. A. Sokolov and I. M. Ternov, *On Polarization and spin effects in the theory of synchrotron radiation*, Phys. Dokl. **8**, 1203–1205 (1964).

[SW98] K. Suzuki and W. Weise, *Chiral constituent quarks and their role in quark distribution functions of nucleon and pion*, Nucl. Phys. **A634**, 141–165 (1998), hep-ph/9711368.

[Wan] W. Wander, *Reconstruction of high-energy scattering events in the HERMES experiment. (PhD thesis, University of Erlangen-Nuernberg, in German)*, DESY-HERMES-96-23.

[Wei] C. Weisskopf, *Messung der spinabhaengigen Strukturfunktion g_1^d des Deuterons mit dem HERMES-Experiment (PhD thesis, University of Erlangen-Nuernberg, in German)*, DESY-THESIS-2002-039.

[Wen] J. Wendland, *Polarized parton distributions measured at the HERMES experiment (PhD thesis)*, DESY-THESIS-2003-032.

[Wen01] J. Wendland, Particle Identification for HERMES Run I (HERMES Internal Note 01-067), November 2001.

[WRB+90] L. W. Whitlow, S. Rock, A. Bodek, E. M. Riordan and S. Dasu, *A precise extraction of $R = \sigma_L/\sigma_T$ from a global analysis of the SLAC deep inelastic ep and ed scattering cross-sections*, Phys. Lett. **B250**, 193–198 (1990).

[ZT80] M. J. Zuilhof and J. A. Tjon, *Electromagnetic Properties of the Deuteron and the* BETHE-SALPETER *equation with One Boson Exchange*, Phys. Rev. **C22**, 2369–2382 (1980).

Acknowledgments

First of all I would like to thank my doctoral advisor, Prof. Klaus Rith, for his support and the excellent combination of freedom and guidance which he gave me during my work on this thesis during the last years.

With Caroline Riedl I shared not only C code, monsterous kumacs and the work on the inclusive analysis but also cookies, weird opinions and fortunately a quite similar sense of humor which was a lot of fun – although at times certainly a trial for our environment... ;-)

Basically all I know about how to analyse the HERMES data I learned from Elke-Caroline Aschenauer. She used to be my supervisor during the time when I worked on my diploma thesis and afterwards remained the person I could ask anything at any time (really....) and get helpful answers. Thank you Elke for all your help and support!

I would like to thank...

... all (former and present) members of the inclusive analysis group, especially Christoph Weiskopf, Lara De Nardo, Marco Contalbrigo, Davide Reggiani, Caro Riedl, Wolf-Dieter Nowak, Uta Stösslein, Helmut Böttcher and Norik Akopov.

... Andy Miller, who first suggested and worked out the unfolding formalism used in this thesis for many enlightening discussions.

... Caro Riedl, Markus Diefenthaler and Alexander von Behaim-Schwartzbach for proof-reading my thesis and for their comments and valuable suggestions.

... all members of the Erlanger Gruppe, especially Prof. Steffens, Christian Vogel (who more than once rescued me when in deep trouble with software problems!), Martin Raithel (who always was the first one I asked when I needed help in Erlangen – thank you Martin!!), Nils Pickert, Achim Hillenbrand, Phil Tait, Dietmar Zeiler, Friedrich Stinzing and Bernhard Krauss.

... the HERMES computer gurus Alexander Kisselev (also for the extremley efficient way in which we have been sharing an office for four years!), Larry Felawka, Maurice Bouwhuis and Eduard Avetisyan.

... our secretaries: Eleonore Hassler in Erlangen and Sabine Krohn, Sörne Möller and Evelyn Olabisi in Hamburg for their friendly help with organizing meetings, phone conferences and all sorts of formalities.

Special thanks to Carmen and Wolfgang Haupt-Nagengast for giving me a home in Erlangen and for their friendship!

I cannot thank enough my parents, Marianne and Matthias Ehrenfried, for their love and support. Zu wissen, woher man kommt, hilft einem zu wissen, wer man ist.

```
              .---. .---.
             :     : o   :    me want cookie!
         _..-:   o :     :-.._    /
     .-''  '   `___' `___' "   ``-.
   .'   "   '  "  .    "  . '  "  `.
  :   '.---.,,.,...,.,.,..---.   ' ;
  `. " `.                      .' " .'
   `.  '`.                   .' ' .'
    `.    `-._           _.-' "  .'  .----.
      `. "    '"--...--"'  . ' .' .'   o    `.
      .'`-._'    " .     " _.-'`. :       o  :
    .'      ```--.....--'''    ' `:_ o       :
  .'    "     '         "     "   ; `.;";";";'
 ;         '       "       '     . ; .' ; ; ;
;     '         '       '   "    .'      .-'
'  "     "   '      "           "    _.-'
```